Lire
le début
de la thèse

3.6 Proper orthogonal decomposition of the wake flow

In order to have a better understanding of the flow behavior, a proper orthogonal decomposition (POD) is performed on the measured velocity field for the tests at $\mathrm{Re} = 0.5 \cdot 10^6$ and angle of attack of 10°. The POD has been computed on the entire PIV field. The vorticity of each mode is also computed. The POD allows for detecting the coherent structures featured by the flow field on the basis of their wake number and frequency. The POD is extensively used for the assessment of turbulent flow fields, when dealing with experimental data, or with numerical computations [Ber11].

The velocity field can be expressed as a composition of spatial and temporal modes as follows:

$$U'(x,t) = \sum_{i=1}^{n} \phi_i(x) a_i(t), \tag{3.1}$$

being $\phi_i(x)$ and $a_i(t)$ the i^{th} spatial and temporal modes, respectively. The method proposed in Ref. [Per05] is selected among the several techniques employed for the flow modal decomposition. This approach is particularly suitable for experimental data. As the field is discretized in N_x spatial samples for each N snapshots, PIV issues a matrix of data that can be written as:

$$M = \begin{bmatrix} u_1^1 & u_1^2 & u_1^{N-1} & u_1^N \\ u_2^1 & u_2^2 & u_2^{N-1} & u_2^N \\ u_{N_x}^1 & u_{N_x}^2 & u_{N_x}^{N-1} & u_{N_x}^N \\ v_1^1 & v_1^2 & v_1^{N-1} & v_1^N \\ v_2^1 & v_2^2 & v_2^{N-1} & v_2^N \\ v_{N_x}^1 & v_{N_x}^2 & v_{N_x}^{N-1} & v_{N_x}^N \end{bmatrix} \tag{3.2}$$

The correlation matrix required for the modal decomposition is computed as :

$$R = \frac{1}{N} M^T \cdot M, \tag{3.3}$$

and the corresponding eigenvalue problem writes

$$RA = \lambda A, \tag{3.4}$$

being λ the array of eigenvalues and A the matrix of eigenvectors. The computed eigenvalues are then rearranged in descending order as $\lambda_1 > \lambda_2 > ... > \lambda_N = 0$. The matrix of eigenvectors is employed to compute the spatial modes as follows:

$$\phi_i = \frac{\sum_{j=1}^{N} A_j^i u^j}{||\sum_{j=1}^{N} A_j^i u^j||}, \quad i = 1, 2, ...N \tag{3.5}$$

being ϕ_i the i^{th} spatial mode. The computation of the temporal modes is straightforward:

$$a_i = \phi_i M \tag{3.6}$$

Based on 15000 snapshots, the first 200 modes are retained from the POD. In the following only the first five modes and the higher order modes exhibiting the most significant vortical structures are displayed and discussed in a first time. Subsection 3.6.5 deals with higher POD modes to underline the control strategy. Namely, Von Kármán, Kelvin Helmholtz and two other coherent vortical structures have been detected within the wake. First the static configuration, i.e. with the trailing edge non-actuated, is discussed. Then PODs for the velocity fields obtained by trailing edge actuation at frequency $f_a^* = 3.7$ (55Hz) and amplitude $a^* = 0.03\%$ (500V) and $a^* = 0.06\%$ (1000V) respectively are illustrated. Finally the spatial and temporal modes for excitation at frequency $f_a^* = 0.83$ 12.5Hz and amplitude $a^* = 0.09\%$ (1000V) are described.

The Figures 3.16, 3.18, 3.20, 3.22, 3.23, 3.24a, 3.25, 3.26, 3.27c, 3.27b represent from left to right: i) the stream-wise component of the i^{th} spatial velocity mode; ii) the crossflow component of the i^{th} spatial velocity mode; iii) the vorticity computed for the corresponding i^{th} spatial velocity mode; iv) the power spectral density (PSD) of the temporal mode associated to the velocity magnitude. The velocity spatial modes are normalized by the free stream velocity. The black triangle on the left hand side of the flow fields represents the location of the wing trailing edge.

The PSDs are computed using the Welch's weighted overlapped segment averaging estimator [Wel67]. Periodogram estimations use 4 s Hamming windows with 64% overlap (minimum variance) and zero padding. The shedding frequencies are often provided in non dimensional form, using Strouhal number.

3.6.1 POD of the PIV measurements for the baseline configuration

Figure 3.16 displays the first five modes issued by the POD. The first mode (four plots on the top of the figure) corresponds to the time average of the flow field. The wake region is clearly visible both on the velocity and on the vorticity fields. In particular the two counter-rotating vorticity regions correlated to the flow from the upper and on the lower side of the wing section are clearly visible. The PSD of the temporal mode decays rapidly, as expected for the mean field. The energy content of mode #1 is equal to the 98.4% of the total energy, see Figure 3.15. An estimation of the energy featured by a specific mode is provided by the associated eigenvalue, or equivalently by the area subtended by the PSD of the temporal mode. Modes #2 and #3 exhibit shear layer vortical structures, detectable both on the velocity and on the vorticity fields. The peak at Strouhal St = 11.5 observed in the PSD confirms shedding phenomena typical of Kelvin Helmholtz instabilities. The shear layer instability frequency is consistent with the estimation provided in section 3.4, as well as with the findings of [Szu+15] for numerical simulations in transonic conditions. With this regard it's worth remarking that the flow beside the wake in Ref. [Szu+15] features local Reynolds number comparable to that of the experiments carried out in the present work. In fact the flow is substantially decelerated downstream the shock on the suction side. By considering at the velocity fields of modes #2 and #3, they are in space quadrature, and additionally they feature the same spectrum and the same energy content. Therefore a progressive wave of counter-rotating vortices occurs, alternately shed from the trailing edge, and convected downstream.

Modes #4 and #5 seem chaotic and are discussed in 3.6.5.

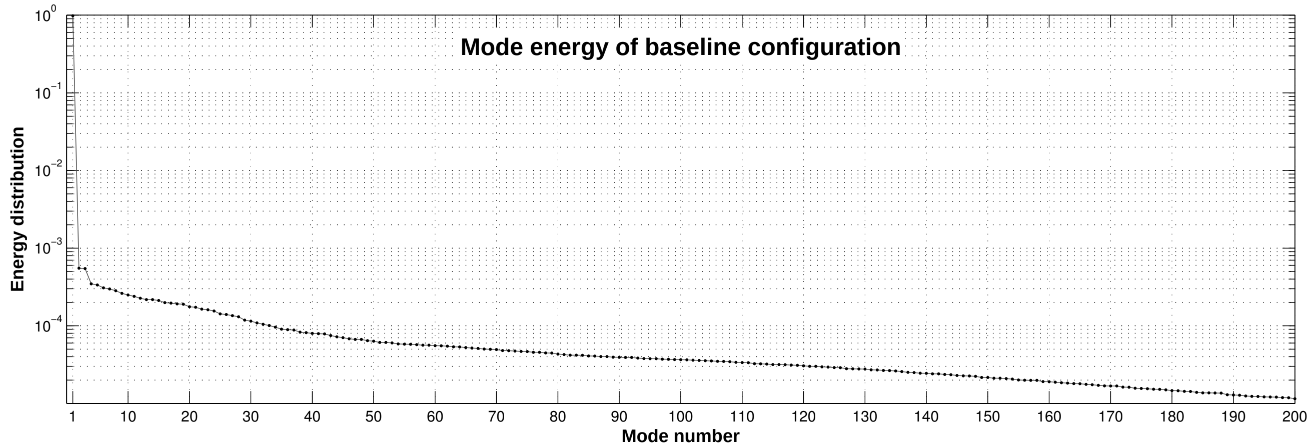

(a)

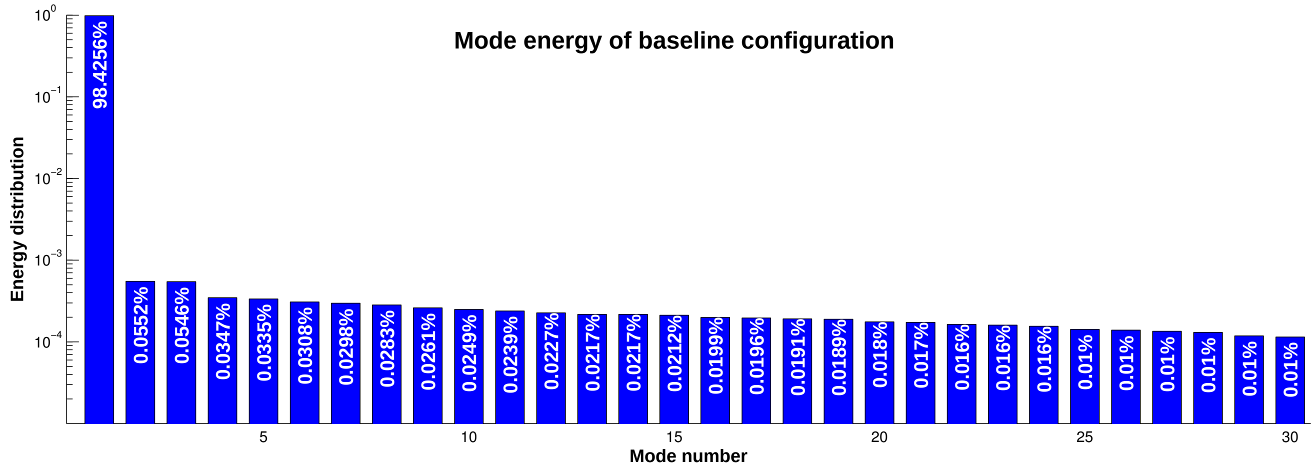

(b)

Figure 3.15: Energy distribution of the first modes issued from the POD for the baseline configuration. The first 200 are presented in (a), (b) focuses on the first 30.

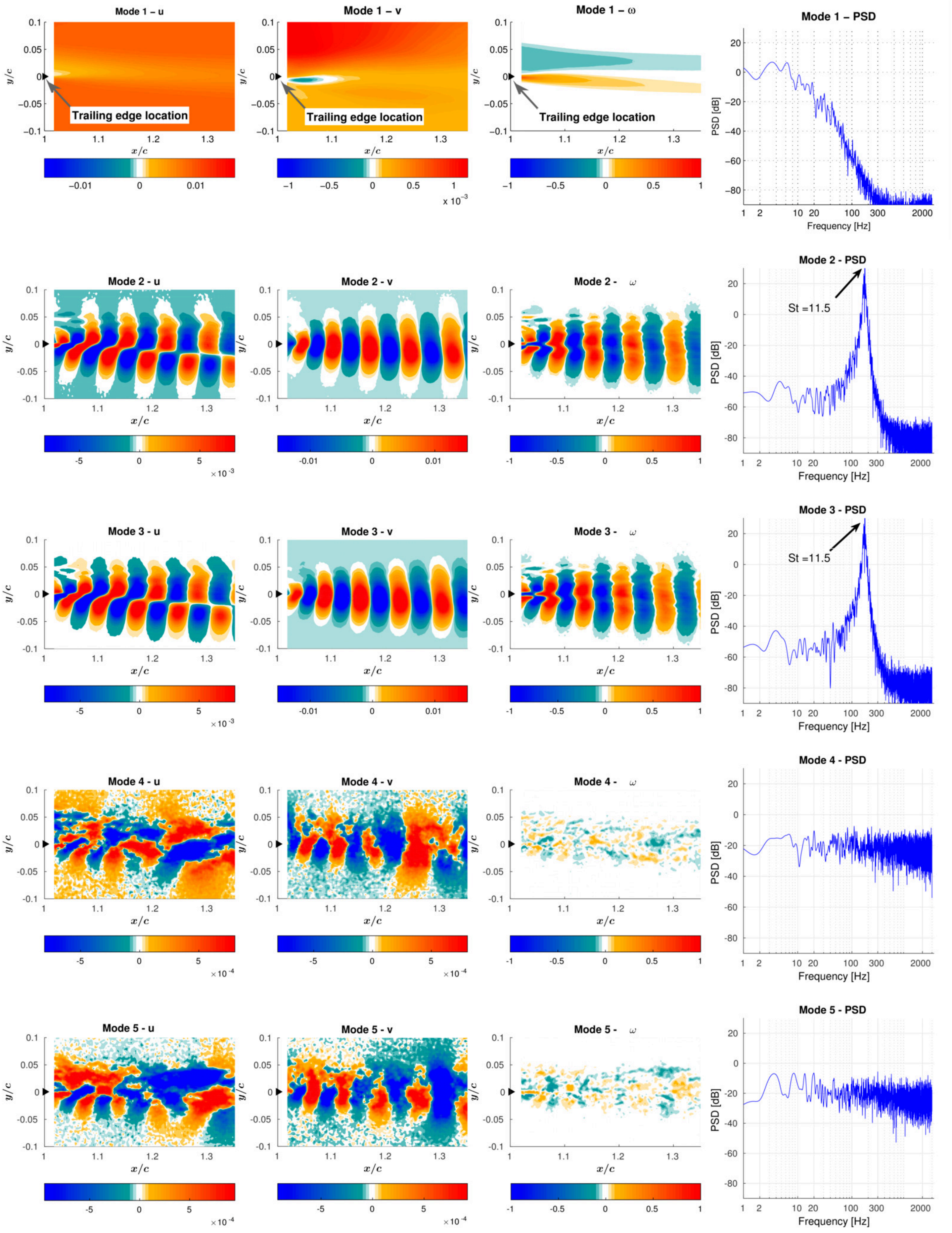

Figure 3.16: POD of the first five modes for the non actuated configuration. From left to right: stream-wise velocity component; crossflow velocity component; vorticity of the corresponding mode; PSD of the temporal coefficients of each POD mode.

3.6.2 POD of the PIV measurements for HFVTE at $f_a^* = 3.7\ a^* = 0.03\%$ (55Hz 500V)

Results of the POD performed for the velocity data measured with actuation at $f_a^* = 3.7\ a^* = 0.03\%$ (55Hz and amplitude 500V) are discussed here. The trailing edge tip cross flow peak to peak velocity imposed by the actuation corresponds to $1\%U_\infty$. The reader can refer to Figure 3.3 (performance of the HFVTE actuator), assuming in this actuation case the vibration amplitudes and velocities are halved, as the voltage is halved compared to the 1kV characterization in the figure (specifically, assuming linear piezoelectricity).

Figure 3.18 shows the first five spatial modes, together with the PSD of the corresponding temporal mode. The first row of figures from the top is the first mode, therefore it describes the mean behavior of the wake. The velocity and vorticity fields, as well as the PSD of the temporal mode, resemble the static counterpart. However in this case the energy associated to the first mode contains the 97.5% of the total energy, therefore it is smaller than the static analogue. As a consequence a larger fraction of energy is contained within the higher order modes, see Figure 3.17.

The second row of plots in Figure 3.18 displays the second mode of the POD. Mode #2 shows non-coherent vortices with almost flat and high amplitude PSD. Modes #3 and #4 exhibit Kelvin Helmholtz vortices. Their frequency shifts from $St = 11.5$ (173Hz) of the non-actuated case, to $St = 11$ (165Hz). The corresponding dimensional frequency of 165 Hz corresponds to three times the actuation frequency. Mechanisms of such change in flow due to morphing are explained in section 3.6.5.

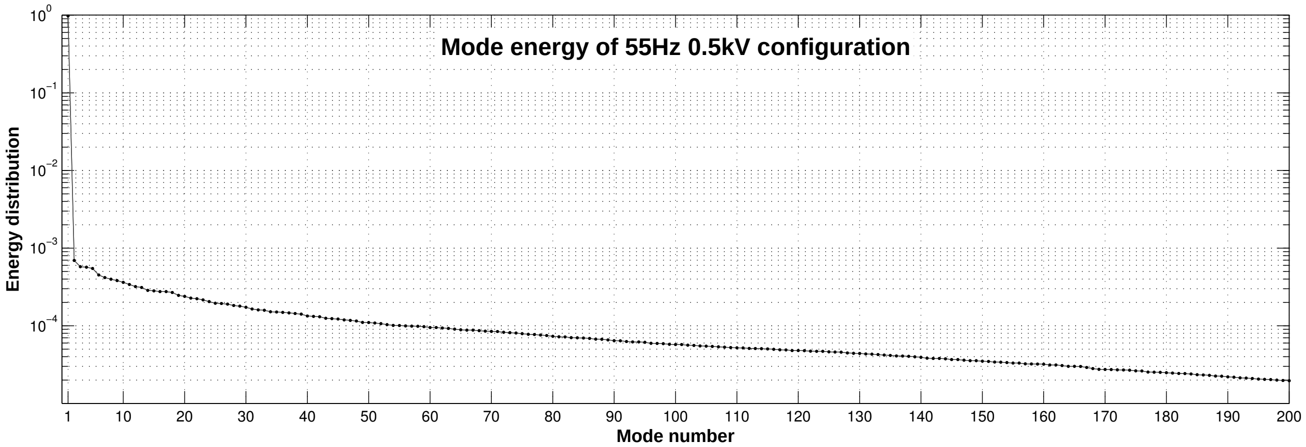

(a)

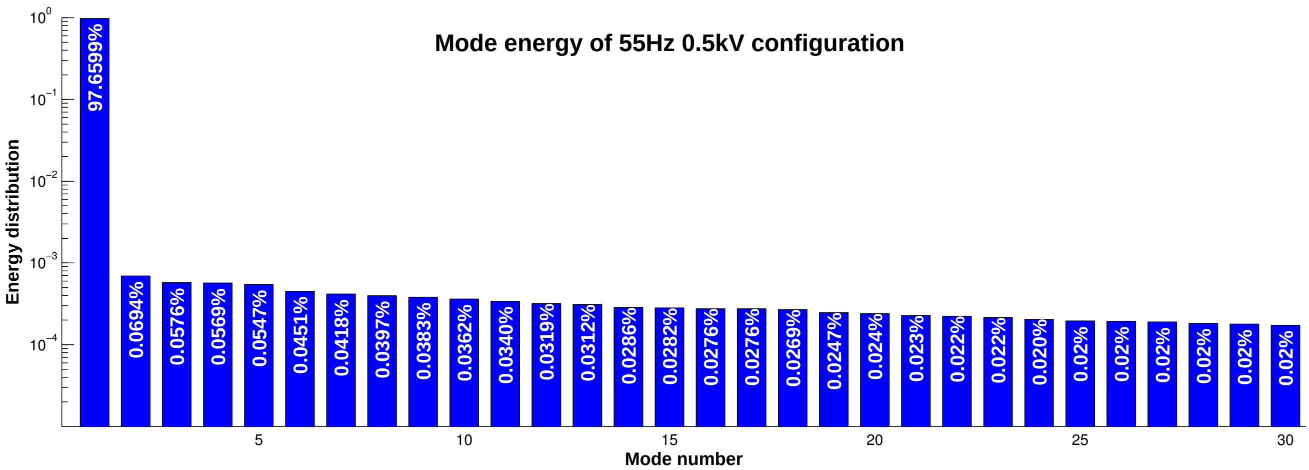

(b)

Figure 3.17: Energy distribution of the first modes issued from the POD with trailing edge harmonic actuation at $f_a^* = 3.7$ $a^* = 0.03\%$ (55Hz 500V). The first 200 are presented in (a), (b) focuses on the first 30.

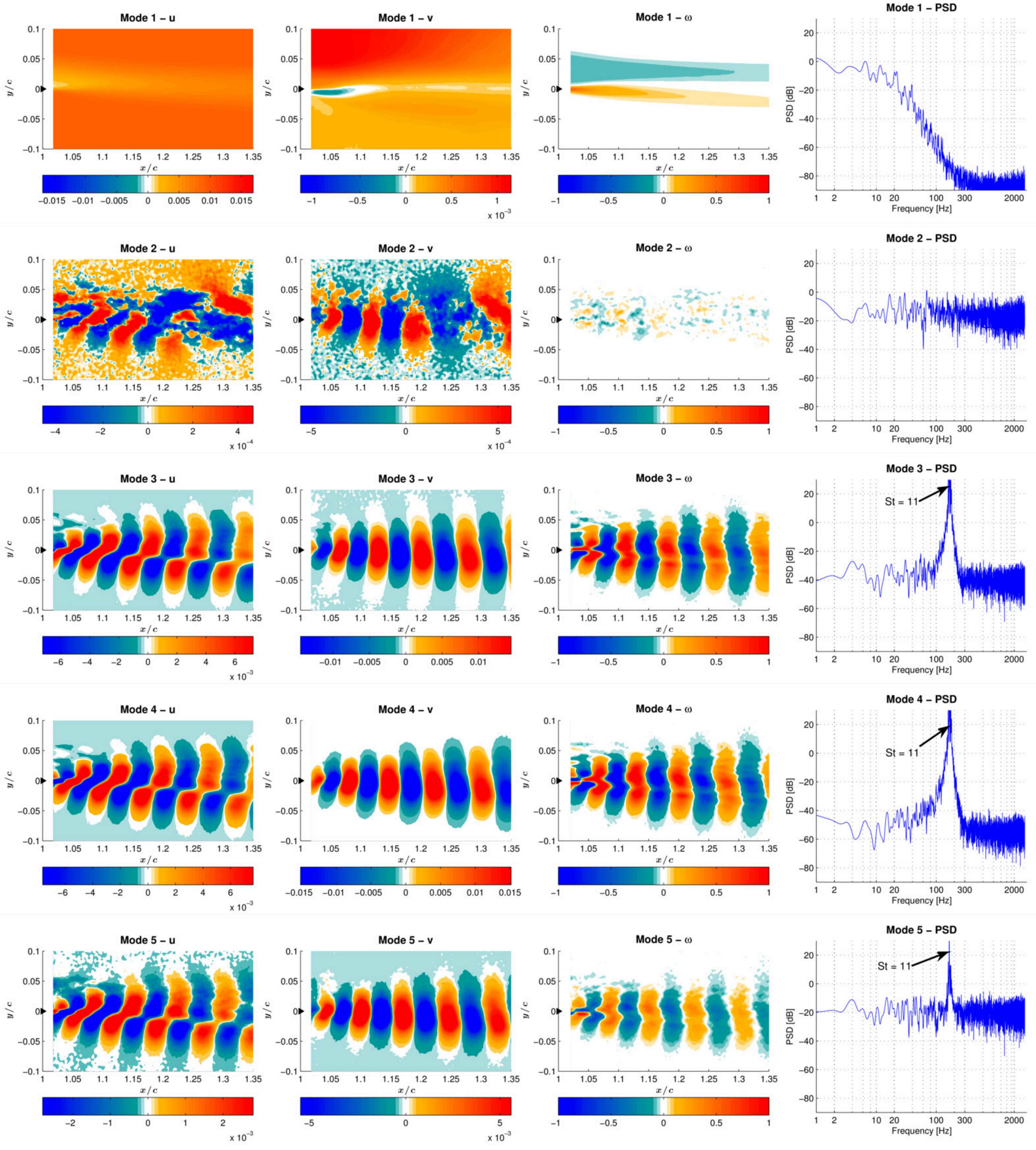

Figure 3.18: POD of the first five modes with trailing edge harmonic actuation at $f_a^* = 3.7$ $a^* = 0.03\%$ (55Hz 500V). From left to right: stream-wise velocity component; crossflow velocity component; vorticity of the corresponding mode; PSD of the temporal coefficients of each POD mode.

3.6.3 POD of the PIV measurements for HFVTE at $f_a^* = 3.7\ a^* = 0.06\%$ (55Hz 1000V)

Figure 3.20 shows the first five POD modes extracted by the measured velocity field. The energy content of the first mode is 97.5% of the total energy, as for the actuation at 500V. Therefore the energy content of the mean flow remains unchanged when doubling the actuation amplitude, as shown in Figure 3.19. Mode #2 exhibits a tight peak in the PSD of the temporal mode at three times the actuation frequency, i.e., St = 11. This mode is associated with coherent vortical structures not observed within the non actuated configuration. The energy content of mode #2 is found to be larger compared to the static counterpart.

With regard to modes #3 and #4 similar effects to those obtained when actuating at 500V are observed. Namely Kelvin Helmholtz structures are shifted to St = 11 (165Hz), corresponding to three times the actuation frequency. The mechanisms of such change in flow due to morphing are explained in section 3.6.5.

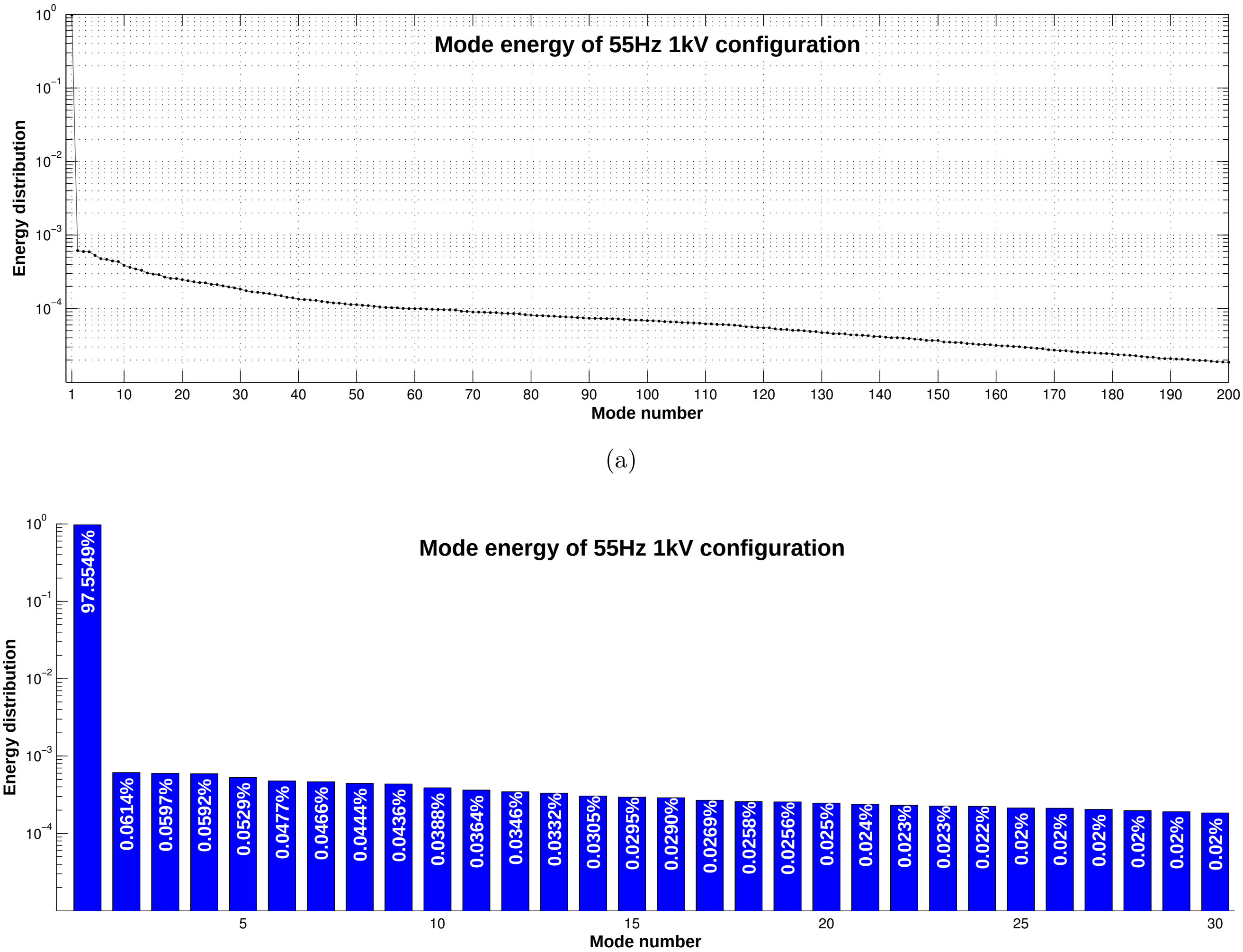

(a)

(b)

Figure 3.19: Energy distribution of the first modes issued from the POD with trailing edge harmonic actuation at $f_a^* = 3.7$ $a^* = 0.06\%$ (55Hz 1000V). The first 200 are presented in (a), (b) focuses on the first 30.

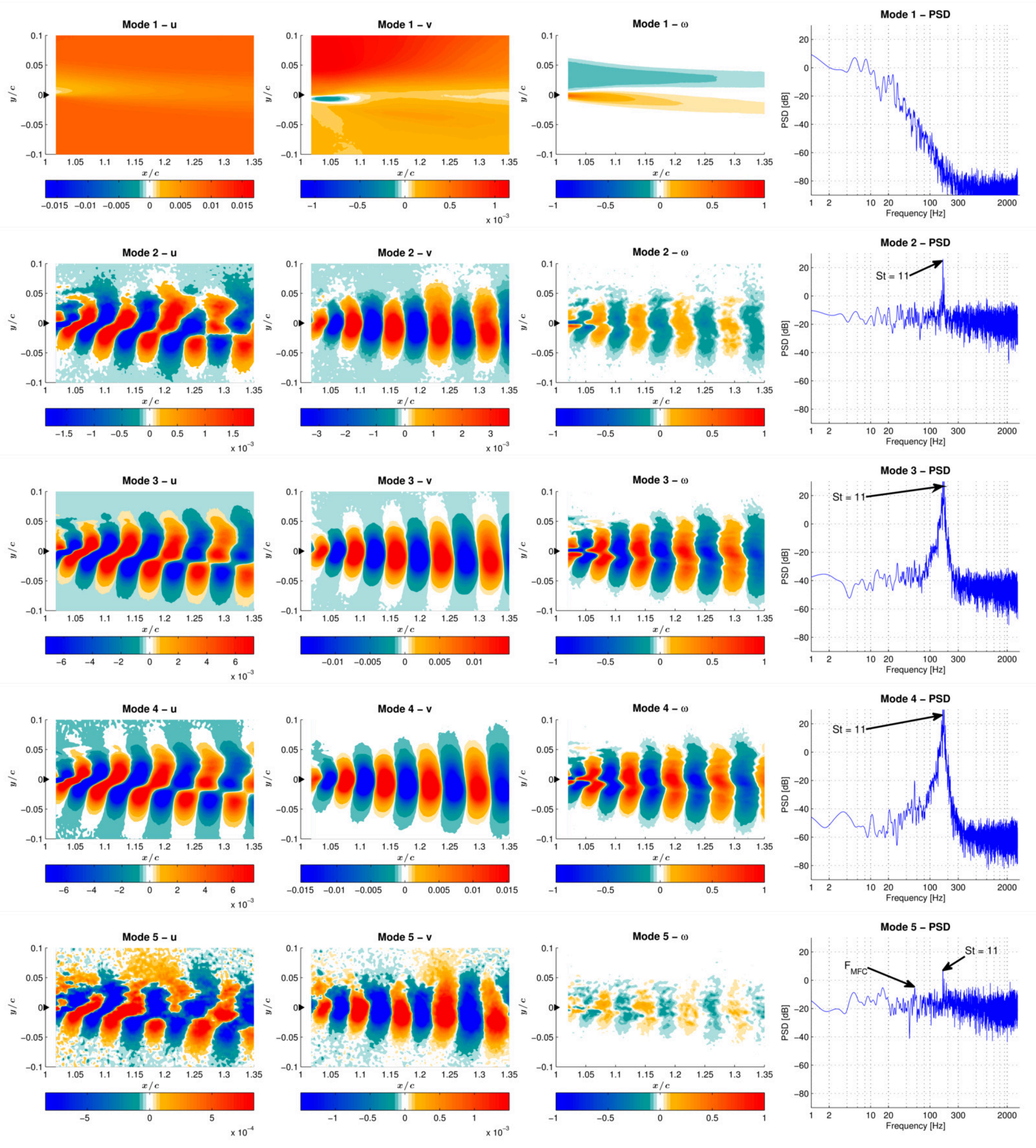

Figure 3.20: POD of the first five modes with trailing edge harmonic actuation at $f_a^* = 3.7$ $a^* = 0.06\%$ (55Hz 1000V). From left to right: stream-wise velocity component; crossflow velocity component; vorticity of the corresponding mode; PSD of the temporal coefficients of each POD mode.

3.6.4 POD of the PIV measurements for HFVTE at $f_a^* = 0.83\, a^* = 0.09\%$ (12.5Hz 1000V)

The response of the flow to harmonic excitations at frequency $f_a^* = 0.83$ (12.5Hz) and amplitude $a^* = 0.09\%$ (1000V) is finally investigated by means of POD. The deflection velocity of the trailing edge tip is $0.45\% U_\infty$.

Figure 3.22 shows the first five modes issued by the POD of the measured velocity field. The first mode, corresponding to the time average of the velocity and of the resulting vorticity, features an energy content of 97.6%, not dissimilar to that of the static counterpart, see Figure 3.21.

The energy content of mode #2 contains the 0.06% of the total energy amount. The corresponding velocity and vorticity fields show non-coherent vortices with almost flat and high amplitude power spectral density. The flow energy of this mode appears to be significantly increased compared to the non-actuated case. A similar phenomenon as $f_a^* = 3.7$ $a^* = 0.06\%$ (55Hz 500V), i.e. a new chaotic second POD mode is found. Discussion is detailed in section 3.6.5.

The PSD of mode #3, #4 and #5 show peaks at 10 times the actuation frequency (St = 8.5), associated to very coherent structures and corresponding to Kelvin Helmholtz vortices. Moreover, a secondary energy peak is visible at St = 11.7 (175Hz), i.e., 14 times the actuation frequency.

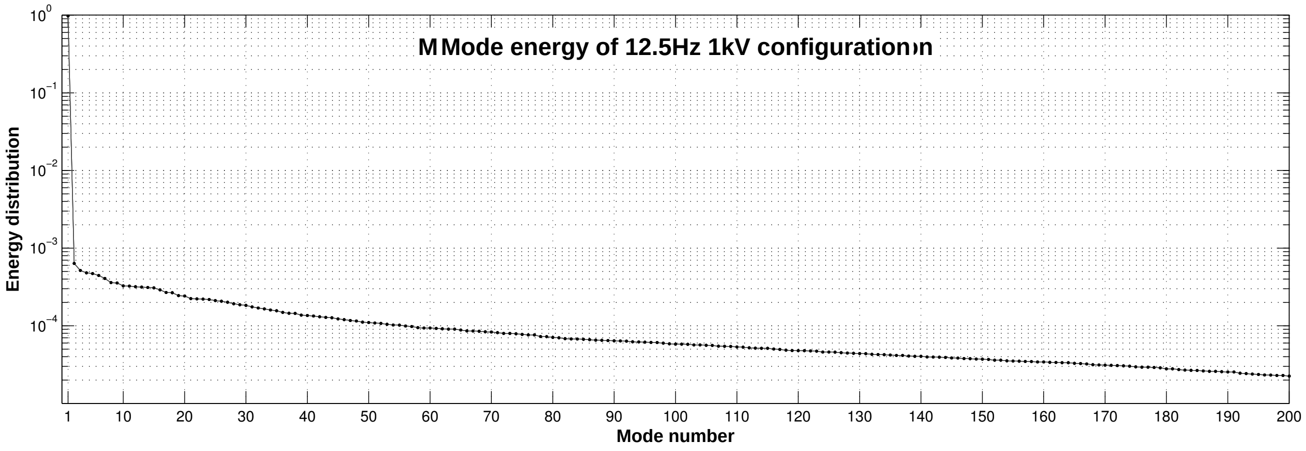

(a)

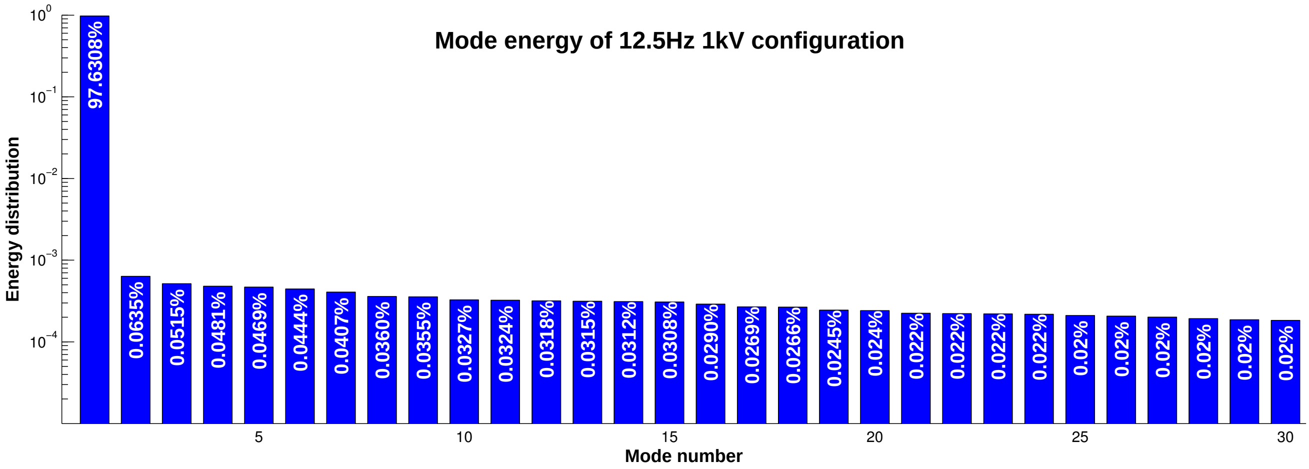

(b)

Figure 3.21: Energy distribution of the first modes issued from the POD with trailing edge harmonic actuation at $f_a^* = 0.83$ $a^* = 0.09\%$ (12.5Hz 1000V). The first 200 are presented in (a), (b) focuses on the first 30.

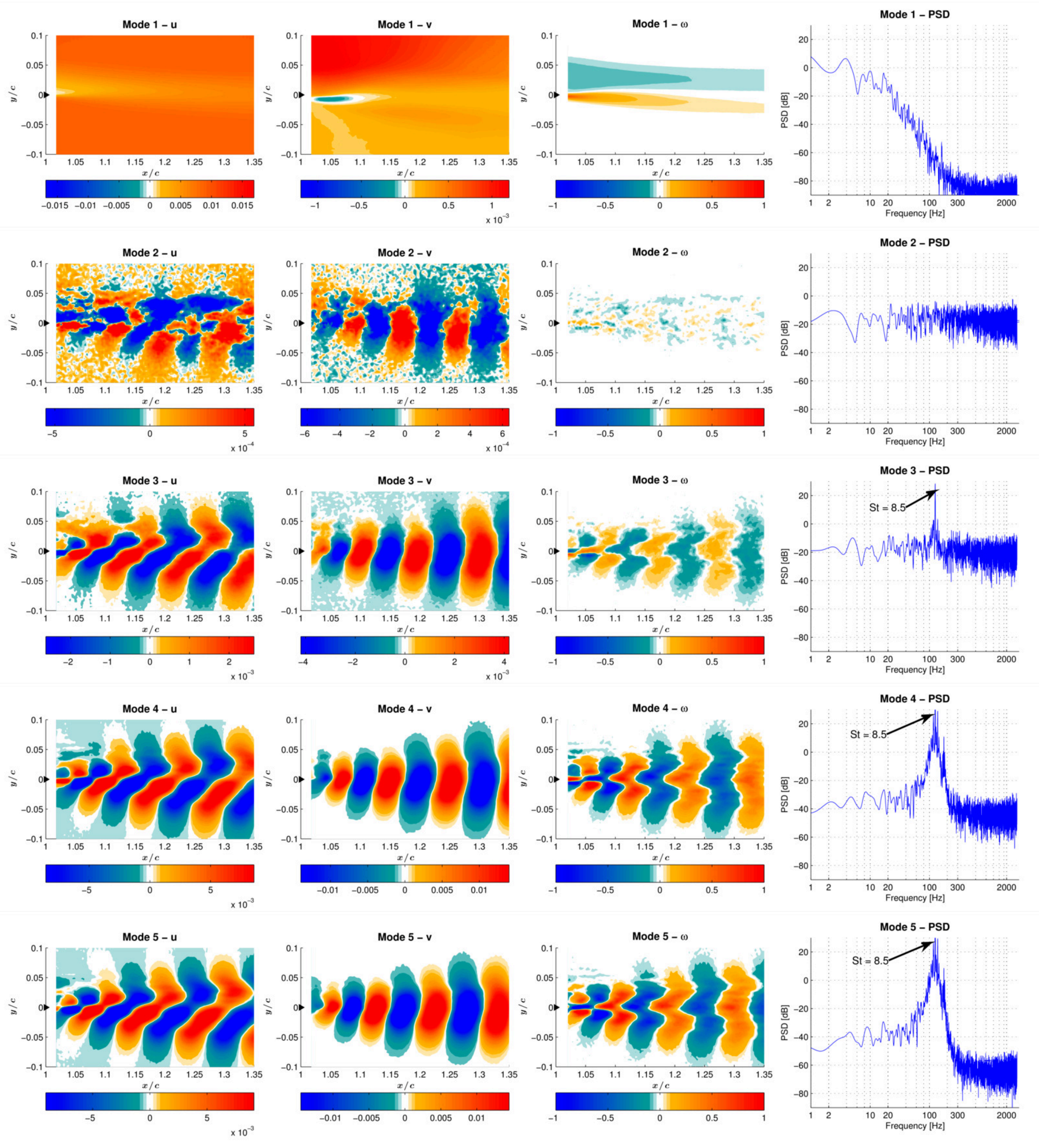

Figure 3.22: POD of the first five modes with trailing edge harmonic actuation at $f_a^* = 0.83$ $a^* = 0.09\%$ (12.5Hz 1000V). From left to right: stream-wise velocity component; crossflow velocity component; vorticity of the corresponding mode; PSD of the temporal coefficients of each POD mode.

3.6.5 Wake mechanisms, higher order modes and control strategies

This section now details some wake mechanisms and focuses on comparison between the different actuations. The control strategy described in section 3.4 is illustrated with experimental results.

1) Von Kármán vortex shedding. Regarding the static baseline, two coherent structures are also observed at $St = 8.5$ (127Hz) and at $St = 3$ (46Hz), or multiples of this latter frequency. Figure 3.23 shows an example of a mode where coherent structures at these frequencies are detected. Specifically modes where peaks at multiples of St = 3 (46Hz) are detected are #8, #9, #16, #17, #18, #19, #20, #24, #27, #34 and #35. Modes with vortex shedding phenomena at St = 8.5 (127Hz) are #12, #13 (Figure 3.25), #14, #15, #16, #17, #18, #19, #21, #22, and #24. As a consequence, there are some modes which exhibit both of these two vortical structures, respectively coupled, see Figure 3.23. It is worth noting that this coupling is found to be strongly affected by the trailing edge actuation discussed in the following. The peak at St = 3 (46Hz) can be associated with the Von Kármán instabilities. The peak at 127Hz (which will be referred to as the letter A in the next section) is a combination of Von Kármán (VK) and shear layer (SL) instabilities according to: $St_{\mathrm{A}} = St_{\mathrm{SL}} - St_{\mathrm{VK}}$.

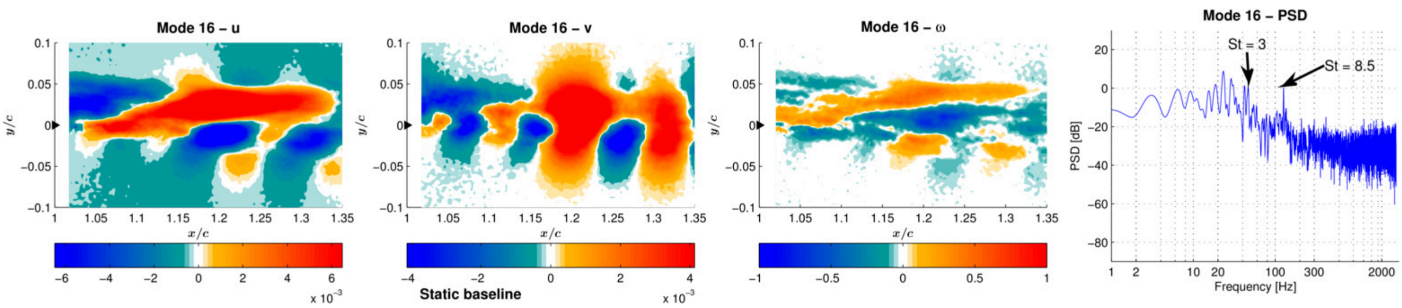

Figure 3.23: POD mode #16 for the non actuated baseline configuration. From left to right: stream-wise velocity component; crossflow velocity component; vorticity of the corresponding mode; PSD of the temporal coefficients of each POD mode.

2) Higher order mode $St = 14$. Figure 3.24a shows the mode #36 issued by the POD of the static case. This mode shows a special coherence and the PSD for the temporal mode corresponds to St = 14.1 (212Hz peaks referred to as B in section 3.5). The corresponding modes in case of morphing at $f_a^* = 3.7$ $a^* = 0.03\%$ (55Hz 500V) are #38 or #39, because the actuation inserts new patterns. For this reason, in the morphing case, mode #39 of the actuated case is compared to mode #36 of the static case (see Figure 3.24b). It can be seen that this mode has lost its spatial coherence, the spectrum does no more display predominant peaks and the vorticity field of this mode indicates a significant of the wake thickness, corresponding to approximatively 15%. This morphing induced effect is analogue to the re-injection of turbulence by means of higher-order POD modes studied numerically by Szubert et al. [Szu+15], enhancing an eddy-blocking effect.

It's also worth remarking that none of the 60 modes retained from the POD for all actuation cases exhibit peaks at St = 14.1 (212Hz). This confirms that these coherent structures are actually dissipated and are not moved towards larger wave numbers. This is an example of vortex breakdown.

3) Shift of modes associated to the shear layer towards higher order-lower energy modes. Both actuations at $f_a^* = 3.7$ $a^* = 0.03\%$ (55Hz, 500V) and $f_a^* = 0.83$ $a^* = 0.09\%$ (12.5Hz, 1000V) exhibit a downshift of the modes #2 and #3 compared to the static baseline. This effect is also present on the $f_a^* = 3.7$ $a^* = 0.06\%$ (55Hz, 1000V) with a higher presence of the actuation frequency in the spectra, due to a larger forcing amplitude. The cause is twofold.

Firstly, the forced flow is found to exhibit vortex shedding phenomena at super-harmonics of the actuation frequency. The two actuations at $f_a^* = 3.7$ (55Hz) have shifted the Kelvin Helmholtz shedding frequency from $St = 11.5$ to 3 times the actuation frequency $St = 11 = 3 \cdot f_a^*$. Actuation at $f_a^* = 0.83$ has shifted this frequency to 10 times the actuation frequency $St = 8.5 = 10 \cdot f_a^*$. Again the forced flow is found to exhibit vortex shedding phenomena at super-harmonics of the actuation frequency. A similar behavior was showed for instance in Refs. [Mot15a; Mot15b] on the flow response to a harmonically oscillating L-shaped Gurney flap.

Secondly, morphing introduces a new chaotic second mode - see modes #2 in Figures 3.18 and 3.22. This energy injection is the signature of the eddy blocking effect described in Section 3.4. The modes #3 and #4 of the morphing case are similar to the modes #2 and #3 of the baseline, so morphing causes the shift of these two modes to higher order. These two modes characterize the main vortex shedding of the wake lost energy. This downshift in energy is associated to vortex breakdown. Specifically, the energy distribution of this morphing case ($f_a^* = 3.7$ $a^* = 0.03\%$) shows that the chaotic mode #2 is 3% more energetic than the coherent mode #3 - see Figure 3.17. This decrease in energy reaches the value of 23% between mode #2 and #3 for the $f_a^* = 0.83$ $a^* = 0.09\%$ morphing case -

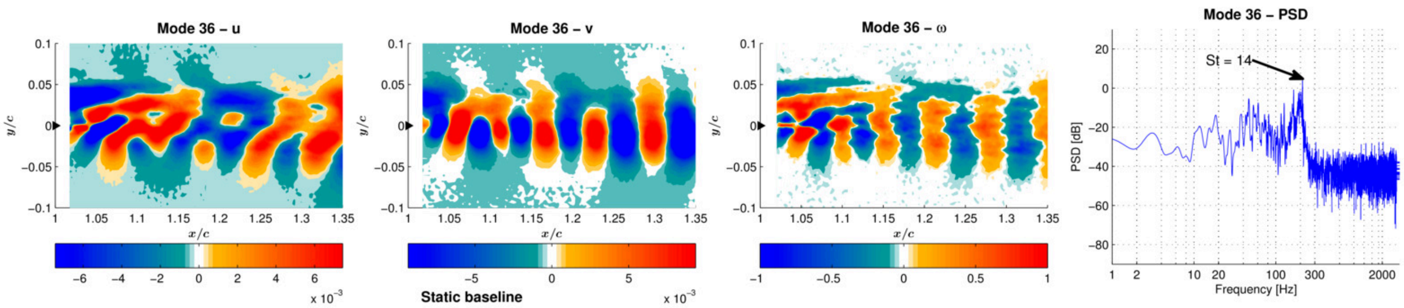

(a) mode #36 for the non-actuated baseline

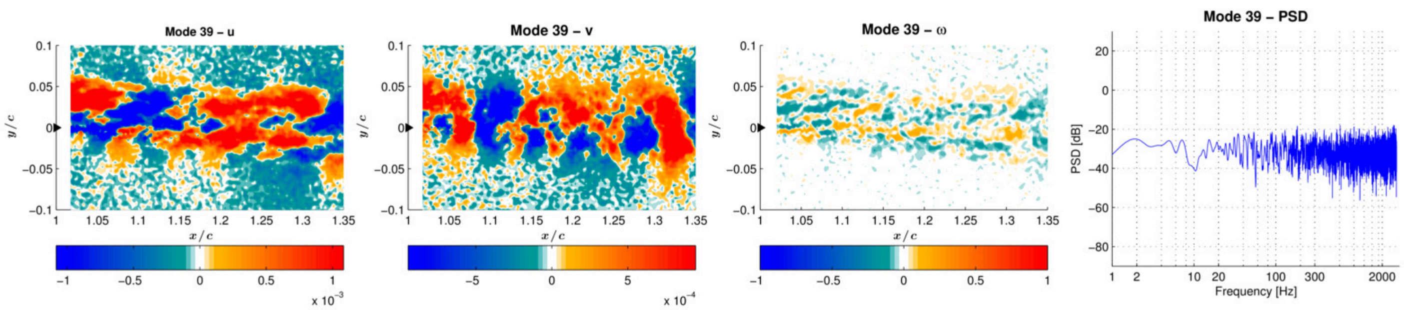

(b) mode #39 for the $f_a^* = 3.7$ $a^* = 0.03\%$ morphing case

Figure 3.24: Comparison of two POD modes. From left to right: stream-wise velocity component; crossflow velocity component; vorticity of the corresponding mode; PSD of the temporal coefficients of each POD mode.

see Figure 3.21. Further shifts in the flow modes with respect to the static case are observed when actuating at $f_a^* = 3.7$ $a^* = 0.03\%$ (55Hz, 500V). Namely coherent structures observed for mode #16 of the static configuration are found on mode #32, not reported here for brevity purposes.

4) Shear layer thinning. Morphing effects on wake thickness are visible on higher POD modes. For instance, the mode #13 of the static baseline (Figure 3.25) indicates wake expansion. The actuated case at frequency $f_a^* = 3.7$ $a^* = 0.06\%$ (55Hz, 1000V) illustrates the eddy blocking effect. The POD mode #22 (Figure 3.26) corresponds to the baseline mode #13, because there are similarities in the spatial mode distribution and their temporal coefficients show the same peak at Strouhal of 8.5; besides, actuation frequency is present in the spectrum of the morphing case (Figure 3.26d). The v component of the mode indicates a thinner wake which decreases in the wake expansion, after $x/c = 1.25$. The wake thickness, indicated by arrows on Figures 3.25c, 3.26c is reduced by approximately 22% at $x/c = 1.35$, thanks to the actuation. One can also remark that – due to the morphing – the magnitude of the characteristic peak at Strouhal of 8.5 has decreased by 10 dB, which means the power density divided by 10.

5) Downshift of the higher energy chaotic modes. Now considering the modes #4 and #5 of the static baseline (Figure 3.16 or Figure 3.27a), similarities can be found with modes #57 of the case $f_a^* = 3.7 - a^* = 0.03\%$ (Figure 3.27b) and the mode #40 of the case $f_a^* = 0.83$ $a^* = 0.09\%$ (Figure 3.27c). These modes have comparable spatial energy distribution. Modes #4 and #5 of the baseline are chaotic but with high energy. The corresponding morphing modes have thinner wakes, due to the eddy blocking effect. Spectra of morphing modes #40 and #57 present peaks that are not present in the static modes; these peaks correspond to harmonic of the actuation frequencies: the Strouhal of 9.2 corresponds to 11 times the actuation frequency ($9.2 \simeq 11 \cdot 0.83$) for the mode #40 whereas the Strouhal of 11 corresponds to 3 times the actuation frequency for the mode #57 ($11 \simeq 3 \cdot 3.7$). It is worth noting that these two morphing cases, both different in amplitude and frequency generate equivalent effects.

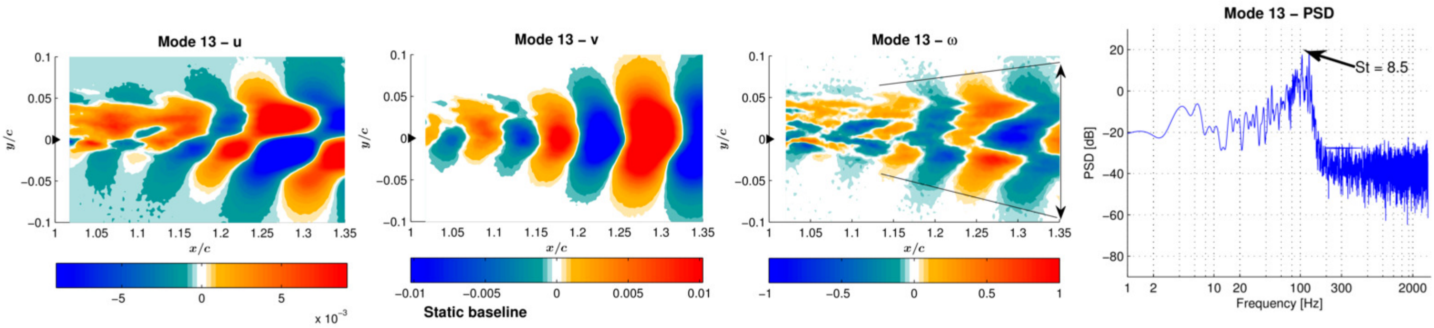

(a) (b) (c) (d)

Figure 3.25: POD mode #13 for the non actuated baseline configuration. From left to right: stream-wise velocity component; crossflow velocity component; vorticity of the corresponding mode; PSD of the temporal coefficients of each POD mode.

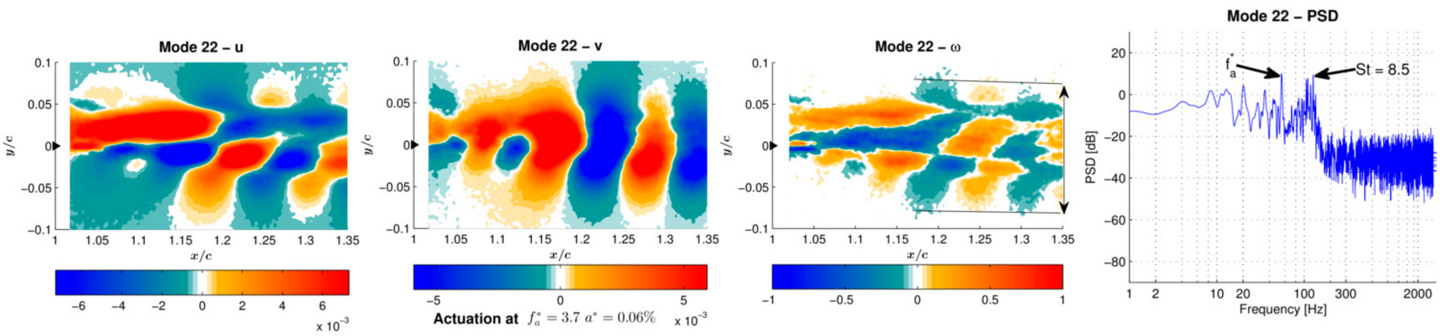

(a) (b) (c) (d)

Figure 3.26: POD of mode #22 with trailing edge harmonic actuation at $f_a^* = 3.7$ $a^* = 0.06\%$ (55Hz 1000V). From left to right: stream-wise velocity component; crossflow velocity component; vorticity of the corresponding mode; PSD of the temporal coefficients of each POD mode.

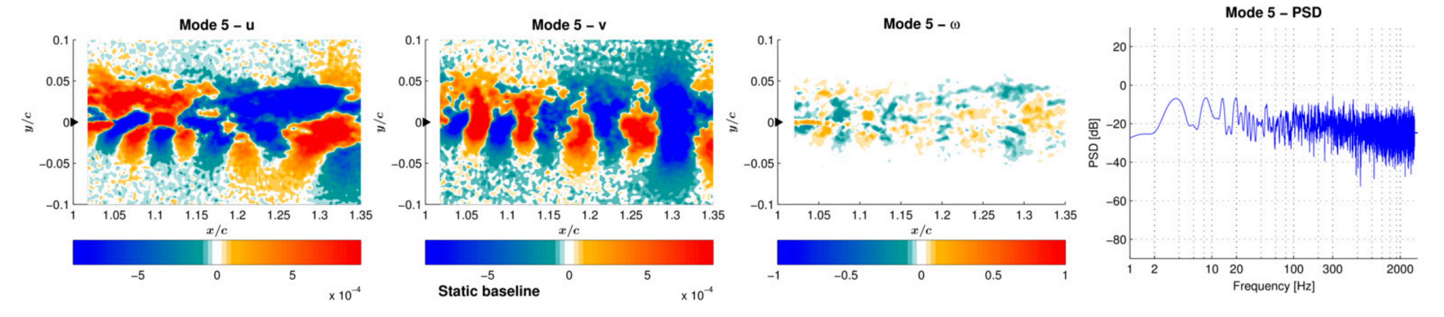

(a) POD mode #5 for the non actuated baseline configuration. From left to right: stream-wise velocity component; crossflow velocity component; vorticity of the corresponding mode; PSD of the temporal coefficients of each POD mode.

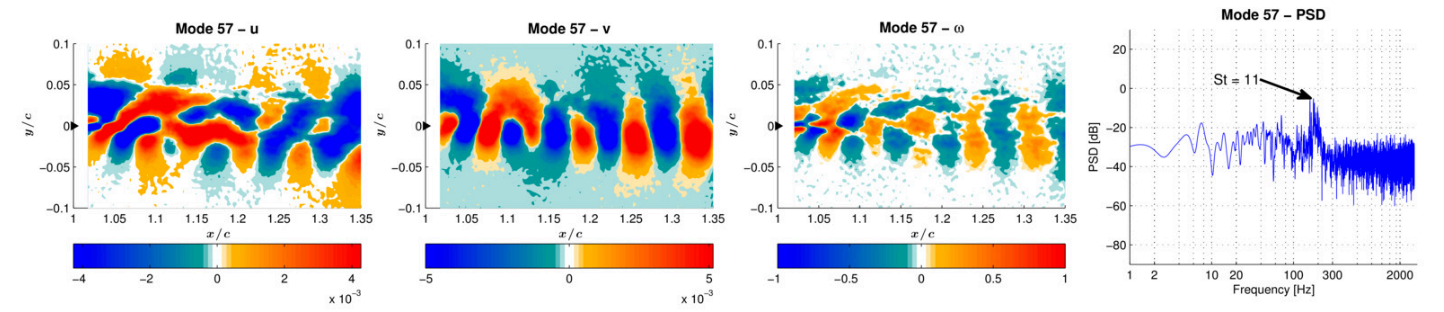

(b) POD mode #57 with trailing edge harmonic actuation at 55 Hz and 500 V. From left to right: stream-wise velocity component; crossflow velocity component; vorticity of the corresponding mode; PSD of the temporal mode for the velocity magnitude.

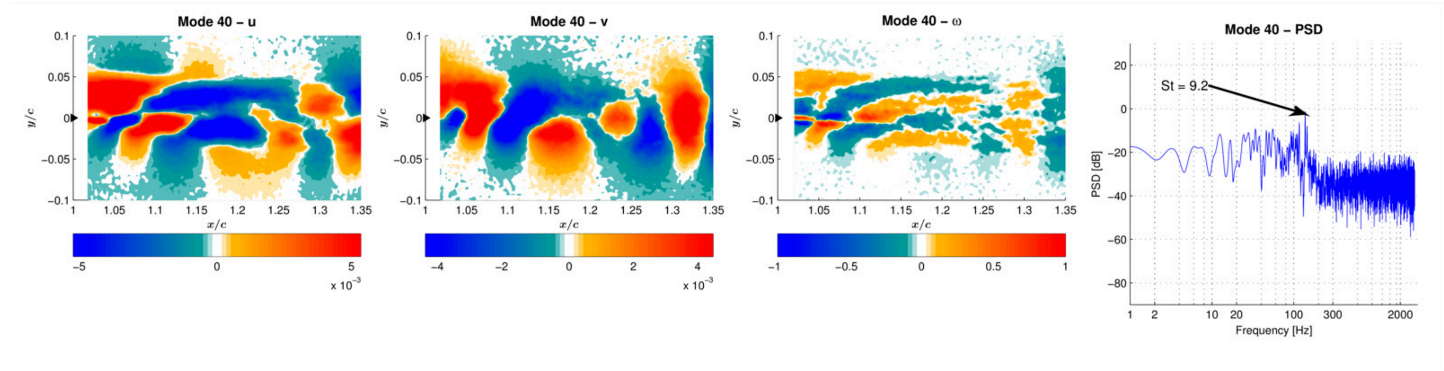

(c) POD mode #40 with trailing edge harmonic actuation at 12.5 Hz and 1000 V. From left to right: stream-wise velocity component; crossflow velocity component; vorticity of the corresponding mode; PSD of the temporal mode for the velocity magnitude.

Figure 3.27: POD modes related to the downshift of higher energy chaotic modes.

3.6.6 General remarks on the POD results

The proper orthogonal decomposition is carried out on the wake velocity field measured by PIV surveys. The first 60 modes issued by POD are investigated in terms of velocity and vorticity fields. The PSD of the temporal mode is also analyzed. It appears that the vortical structures observed at certain frequencies on the unforced flow are shifted to the actuation frequencies or to their higher harmonics. This effect occurs equally for the two actuation amplitudes here considered. With this regard it appears that for the excitation frequency of $f_a^* = 3.7$ (55Hz), actuating at $a^* = 0.03\%$ (500V) is more favorable compared to $a^* = 0.06\%$ (1000V), where a significant increase in the energy of mode #2 relative to the static case is observed. In general comparing the unforced and the forced flow, this latter features a slightly higher level of energy. The fact that the same vortical structures are observed on higher order modes relative to the static case is an indication that a proper vortex breakdown –limited to the larger coherent structures– is occurring. The turbulent fluctuation dynamics shows significant modifications due to the morphing:

- shift of the non-actuated modes 2 and 3 (Figure 3.16) associated to Kelvin-Helmholtz towards the higher order modes 4 and 5 (Figure 3.22) for actuated case;
- disappearance of coherent higher frequency modes: St = 14 for instance, shift of modes associated to the shear layer towards higher-order lower-energy modes;
- shear layer thinning at x/c=1.35 of order 22% (Figures 3.25c and 3.26c); and
- decrease of spectral amplitude of the peak at St=8.5, Figures 3.25d and and 3.26d.

Furthermore, the flow response to wake forcing is similar to that reported in Ref. [Szu+15] for transonic flow conditions. This confirms the potential suitability of high frequency actuation both for subsonic flow conditions here investigated typical of descent flight, and for cruise speeds.

3.7 Spectral analysis of flow velocity

The crossflow velocity component is extracted for 8 points from the TR-PIV measurements. These points are located in the wake close to the trailing edge and downstream, below and above the trailing edge. The center of Figure 3.28 presents the time average stream-wise velocity field of the non-activated baseline flow. The 8 points are numbered on the field. The trailing edge is visible on the left. The different Power Spectral Densities (PSD) of the crossflow velocities are presented in the spectra around the central velocity field. The PSDs are again computed using the Welch's weighted overlapped segment averaging estimator [Wel67]. To maximize the accuracy of the estimator, temporal signals of the three experiment repetitions are concatenated to obtain 33 s signals. Periodogram estimations use 4 s Hamming windows with 64% overlap (minimum variance) and zero padding.

According to the POD results, the flow energy is mainly dominated by the shear layer (SL) coherent instabilities. This corresponds to the SL arrows pointing to the frequency peaks. The shear layer instability is more concentrated in the lower flow, as the SL peaks of points 1 to 4 are over −130dB and the second harmonics are visible (2SL peaks). The points 1, 2, 5 and 6 which are located close to the trailing edge show the frequency signature of the Von Kármán vortices – presented by VK and VK/2 arrows. Coherent structures highlighted by POD analysis at Strouhal of 14.1 appear as B peaks. These peaks are absent from points 6 and 8 corresponding to the flow coming from the suction side. The Von Kármán Strouhal number is evaluated to 3. This is again comparable to CFD simulations of Ref. [Szu+15] with a Strouhal of 2.4 (computed relatively to the chord with the frequency 2630Hz). Peaks A, present on each of the considered points, correspond to the coupling of the Von Kármán and the shear layer structures. Indeed the Strouhal of the peak A is linked to these structures by the relation $St_A = St_{SL} - St_{VK}$. Physically, this can be interpreted as Kelvin Helmholtz amplitude modulation due to the Von Kármán instabilities. This peak identification not only allows for the understanding of the phenomena but also allows identifying spectral signatures in the flow. These signatures can be detected by pressure transducers (see section 3.8). In addition, the flow is significantly affected by the actuation and its effects are clearly visible on the reported spectra.

The crossflow velocity component is extracted for the actuated configurations. Globally the peaks described above are still visible, but some modifications are noticeable. As some spectra are similar, only signals from points 4, 5 and 8 are compared.

Figure 3.29 shows a comparison in PSD of point 4 between the baseline and the $f_a^* = 0.83$ (12.5Hz) actuation. The frequency range is focused on Strouhal from 7.5 to 15. Actuation harmonic frequencies from 9 to 18 are presented on the x-axis.

Peaks of baseline flow named A, SL and B are withdrawn by the actuation. In exchange the actuation gives rise to other peaks. Most of them have lower amplitude and others are harmonics of the actuation frequency. Black arrows indicate peaks corresponding to harmonics of the actuated flow. This phenomenon tends to *spread the peak energies* over actuation harmonics and over other frequencies. This could be interpreted as a vortex breakdown of the largest coherent structures.

Concerning the other points in the wake and the other actuation cases, table 3.1 deals with the Root Mean Square (RMS) values of fluctuating crossflow velocity $\overline{v^2}$ of the 8 extracted points. Variations compared to the non actuated baseline are calculated in percentage. The turbulent energy is decreased by 5 to 7% everywhere for the $f_a^* = 0.83$ (12.5Hz) actuation. The $f_a^* = 6.7$ (55Hz) actuations decrease energy close to the trailing edge by more than 8% but slightly increase it downstream. This effect is more visible for the higher amplitudes for the $a^* = 0.06\%$ (1kV) actuation compared to the $a^* = 0.03\%$ (0.5kV). This result confirms the previous remarks.

Table 3.1: Variations of crossflow velocity RMS at extracted points compared to the baseline configuration.

Point number	1	2	3	4	5	6	7	8
Baseline	0.0%	0.0%	0.0%	0.0%	0.0%	0.0%	0.0%	0.0%
12.5[Hz] 1[kV]	-7.9%	-6.7%	-7.1%	-7.1%	-2.4%	-3.3%	-4.9%	1.0%
55[Hz] 500[V]	-8.7%	-5.8%	-0.1%	4.1%	0.3%	-4.0%	5.4%	6.5%
55[Hz] 1[kV]	-10.0%	-6.7%	0.4%	7.7%	1.5%	-2.1%	8.2%	9.7%

Table 3.2: Variations of crossflow velocity PSD at some noticeable frequencies, at the extracted points 4, 5 and 8. Values are relative to the baseline configuration. Points are ranked by position starting from the trailing edge (point 5) and moving downstream (point 8). Crosses (×) indicate non visible peaks.

	VK ($St = 3$)			A=SL-VK ($St = 8.5$)			B ($St = 14$)		
Fa A*	pt 5	pt 4	pt 8	pt 5	pt 4	pt 8	pt 5	pt 4	pt 8
12.5[Hz] 1[kV]	-3 dB	0 dB	-11 dB	+7 dB	+13 dB	+9 dB	-3 dB	-3 dB	×
55[Hz] 500[V]	-2 dB	×	-14 dB	+1 dB	+8 dB	+4 dB	-5 dB	-5 dB	×
55[Hz] 1[kV]	-2 dB	×	-14 dB	0 dB	+1 dB	0 dB	×	-7 dB	×

	SL ($St = 11.5$)			2SL ($St = 23$)		
	pt 5	pt 4	pt 8	pt 5	pt 4	pt 8
12.5[Hz] 1[kV]	-17 dB	-18 dB	-16 dB	+37 dB	-13 dB	×
55[Hz] 500[V]	-5 dB	-5 dB	-4 dB	×	+4 dB	×
55[Hz] 1[kV]	-5 dB	-4 dB	-4 dB	+1 dB	-3 dB	×

Table 3.2 sums up the effects of morphing on remarkable peaks of the spectra. It is remarkable that a few thousandth of chord fraction vibration amplitude is capable to reduce the large wake vortices power by nearly 99.9% (30 dB). It appears on one hand that both $f_a^* = 6.7$ (55 Hz) and $f_a^* = 0.83$ (12.5 Hz) morphing increase the A peaks, related to the interaction of Von Kármán and shear layer instabilities. On the other the signatures VK linked to the Von Kármán vortical structures are significantly reduced. A noticeable result is that actuation at $f_a^* = 0.83$ (12.5 Hz) deletes the most energetic peaks SL but increases the harmonic peak 2SL in the region close to the trailing edge. In comparison to this actuation, the two morphing cases $f_a^* = 6.7$ (55 Hz) yield smaller reductions and risings of the PSD peaks. Another important result is that the impact of the amplitude at $f_a^* = 6.7$ (55 Hz) is low compared to the impact of the frequency: a larger actuation amplitude increases a bit more the effects on higher frequencies B and 2SL as well as the coupling A between SL and VK. Apart from the effects on the main frequency peaks of the baseline static wing, the actuation generates other frequency peaks. Most of these peaks are actuation harmonics. Harmonic 3 of the $f_a^* = 6.7$ (55 Hz) $a^* = 0.03\%$ (500 V) actuation presents an important PSD level everywhere which increases by 3 dB for the $a^* = 0.06\%$ (1 kV) actuation.

Finally, despite the creation of coherent structures due to the actuation, the HFVTE can be beneficial as it decreases the Von Kármán and Kelvin Helmholtz vortex energies. The actuation amplitude has to be set as a compromise between vortex breakdown effect and energy introduced in the wake.

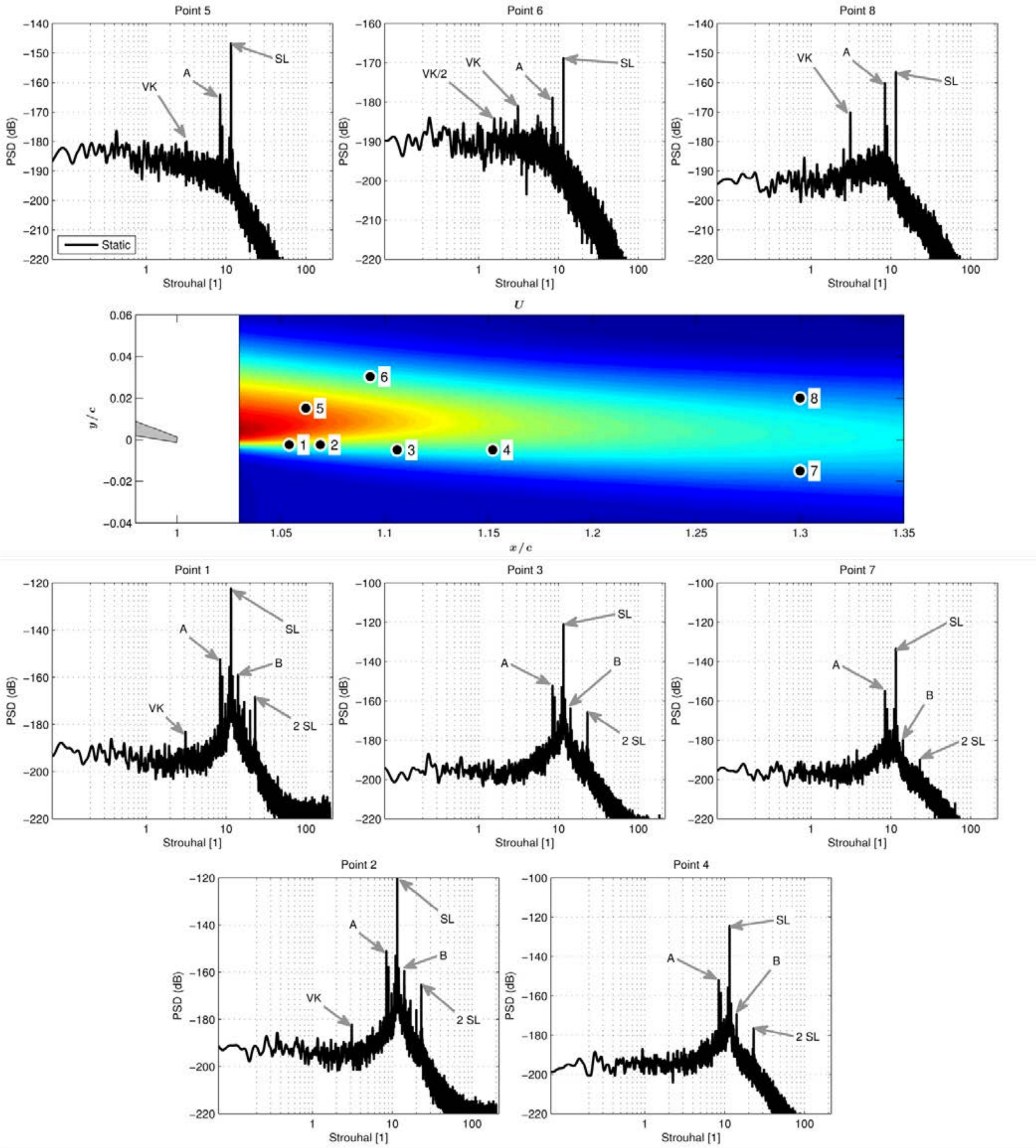

Figure 3.28: PSD of the crossflow velocity on the 8 extracted points, from the baseline configuration. The center figure presents the positions of the extracted points within the time average stream-wise velocity.

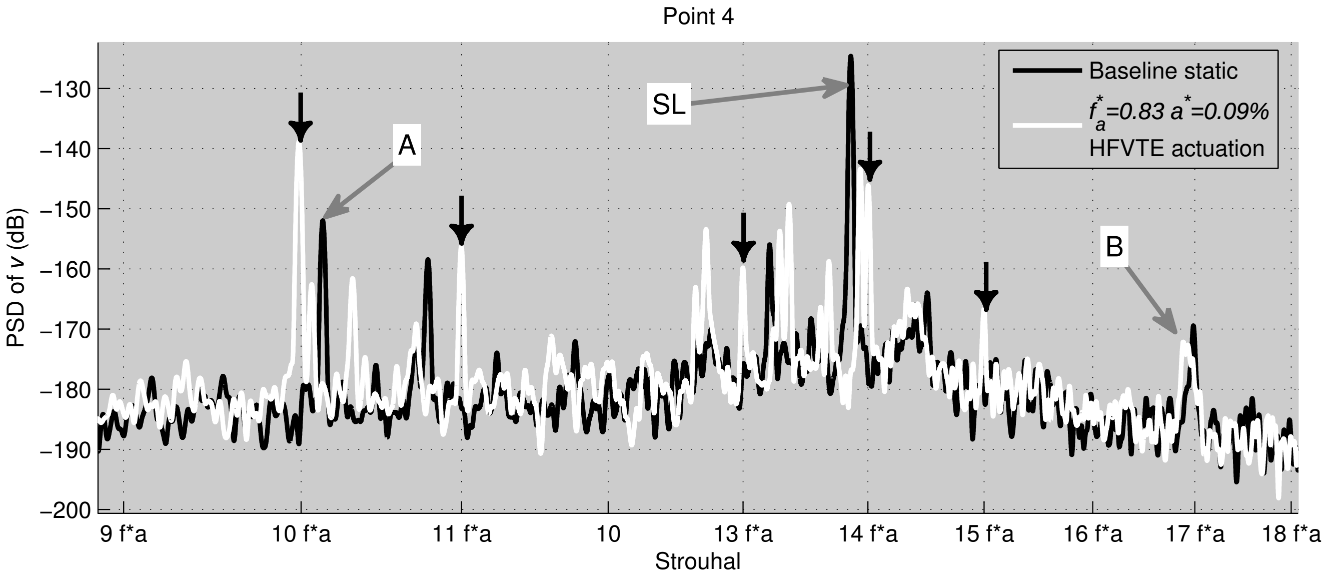

Figure 3.29: PSD magnification of point 4 of the crossflow velocity. Baseline is compared to 12.5Hz actuation. Black arrows indicate peaks at multiples of the actuation frequency f^*a that appear thanks to morphing.

3.8 Effect of high frequency actuation on aerodynamic loads

A second test campaign is carried out in order to investigate the effects of higher frequency actuation on local and resulting airloads over the wing section model. Measurements are performed at Reynolds number $\mathrm{Re} = 10^6$ and angle of attack of $10°$.

Lift and drag are measured with an aerodynamic balance, whereas pressure is acquired by means of a microphone located at the 90% of the chord and in the middle of the model span. To ensure the statistical convergence of measurements an acquisition time of 40 s is employed for each run. For this time lapse all the main statistical indicators have found to converge, both for force and pressure measurements. Flow visualizations are not reported as the limited acquisition time of 6.5 s of the PIV camera memory does not allow reaching the statistical convergence of the measured phenomena for this Reynolds number.

Sinusoidal harmonic inputs are provided to the piezo-actuators, with frequencies in the range $f_a^* \in [3.2, 14.6]$ ($F_a \in [100, 450]$Hz) and amplitude 1000V. The actuation amplitude a^* (or A) is not maintained constant. As mechanical resonance can occur in the range $f_a^* \in [4.9, 7.2]$ ($F_a \in [150, 220]$Hz), the results of the HFVTE actuation in this section depend on both coupled frequency and amplitude. With the aim to check the repeatability of measurements, several acquisitions are performed by alternating actuated with non-actuated runs. For each run, the measure is launched 20 s after the switch of the control input (on/off and vice versa), to allow for the settling of the permanent regime in the flow dynamics, as indicated in A.2. The maximum percentage difference in drag between runs is 0.5%. This confirms the reliability of the measured quantities. With regard to the non actuated configuration, differences between repeated runs are below $10^{-4}\%$ for both lift and drag.

Figure 3.30 displays the percent gain in terms of drag and lift obtained with the trailing edge actuation at a specific frequency referred to as f_a^* and maximum amplitude 1000 V, relative to the non-actuated case. Positive values indicate that the actuation increases the measured quantity, whereas the opposite is meant for negative gains. For each of the actuation frequencies, positive gains in lift and negative gains in drag are obtained. Therefore high frequency trailing edge actuation appears beneficial in improving the overall sectional aerodynamic performance. It can be noticed that the flow at Reynolds number of 1 million undergoes a strong unsteady behavior with modifications of the forces, being this case likely to be close to a bifurcation. The vibration of the trailing edge increases the turbulence intensity in the boundary layer and the transition to turbulence goes more up-

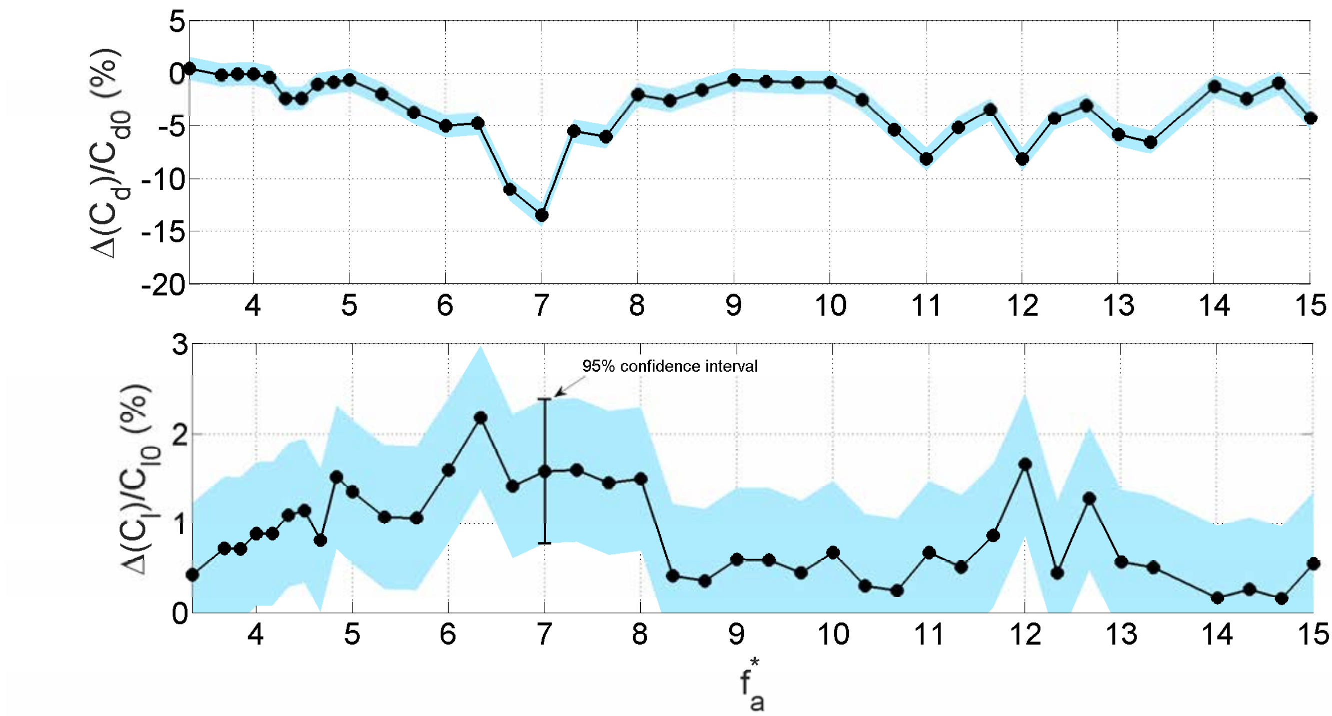

Figure 3.30: Percent gain of mean drag (top) and lift (bottom) coefficients obtained with HFVTE, relative to the non-actuated case. Experiments are done at $Re = 1$ M

stream. Therefore, the flow regime becomes critical. These critical aspects may yield a high sensitivity of the measured drag to the initial conditions and to the perturbations induced by the patch vibrations.

Therefore the eddy blocking effects, observed on in terms of velocity field, appear to yield the expected drag reduction. At $f_a^* = 7$ (210 Hz) the largest drag reduction is obtained. The specific percent gains in drag and lift are:

$$\begin{aligned} \Delta D &= -13,48 +/- 1.8\% \text{ (with incertitude : } 3\sigma) \\ \Delta L &= +1.58 +/- 1.12\% \text{ (with incertitude : } 3\sigma), \end{aligned}$$

being σ the standard deviation of the measures (not the measurement accuracy). At $St = 6.3$ 190Hz the largest lift augmentation is obtained. The corresponding percent gains read:

$$\begin{aligned} \Delta D &= -4.80 +/- 1.08\% \text{ (with incertitude : } 3\sigma) \\ \Delta L &= +2.17 +/- 0.65\% \text{ (with incertitude : } 3\sigma), \end{aligned}$$

Significant effects of piezo-actuation are found both on lift and on drag coefficient. By the way high frequency–low amplitude trailing edge actuation was first conceived specifically to reduce drag within the framework of the present research project. Therefore details on drag behavior are provided by analyzing the results achieved in terms of pressure measurements in the following. Specifically the actuation at $f_a^* = 7$ (210 Hz), where the maximum gain in drag is found, is considered. Pressure measurements – especially if performed on the trailing edge – provide a good indication of the phenomena occurring in the wake, as flow perturbations propagate in each direction, being the Mach number much smaller than the unity everywhere in the domain. In order to check the reliability of pressure measurements the same approach adopted for the balance acquisitions is followed. Namely, for each excitation frequency, several measurements are carried out alternating non-actuated and actuated runs. The maximum difference in terms of measured mean values is 1% among all the runs, for any of the considered excitation frequencies. The statistical stability of measurements without actuation is verified in the same manner. In this case differences between runs are below 10^{-4}%.

Figure 3.31 shows the power spectral density (PSD) of the pressure fluctuations measured with trailing edge actuation at $St = 7$ (210 Hz) (HFVTE activated) and without actuation (MFC OFF), respectively. The plot on the bottom is a blowing up of the top counterpart on the area surrounded by the rectangle. The trailing edge actuation provides a shift of the flow modes, compared to the non-actuated case. Namely, peaks at the actuation frequency, as well as at the corresponding super-harmonics and sub-harmonics are observed. At the same time the peak at $St = 9.5$ (285 Hz), clearly visible on the PSD of the non-actuated case (observed on loads spectra as well), has diminished by 17% compared to the mean spectral level when actuating at $f_a^* = 7$ (210 Hz). In fact actuation adds new peaks in the power spectral density, but the corresponding flow modes result less detrimental for drag, relative to the natural peak at $St = 9.5$ (285 Hz). It's worth remarking that the peak at $St = 9.5$ (285 Hz) highlighting Kelvin Helmholtz instabilities is consistent – in terms of Strouhal number – to the results reported in the previous section for a smaller Reynolds number, as well as to the estimations of Ref. [Szu+15] for transonic flow conditions.

Good indications of the flow instabilities are also provided by the statistical moments of the measured pressure [Nor11]. The variance, the third order (skewness), and the fourth order moments (flatness) are computed on the time histories of pressure measures for excitations at $f_a^* = 7$ (210Hz), and for the static configuration. The percent differences between the actuated and the non-actuated cases are reported in Table 3.3:

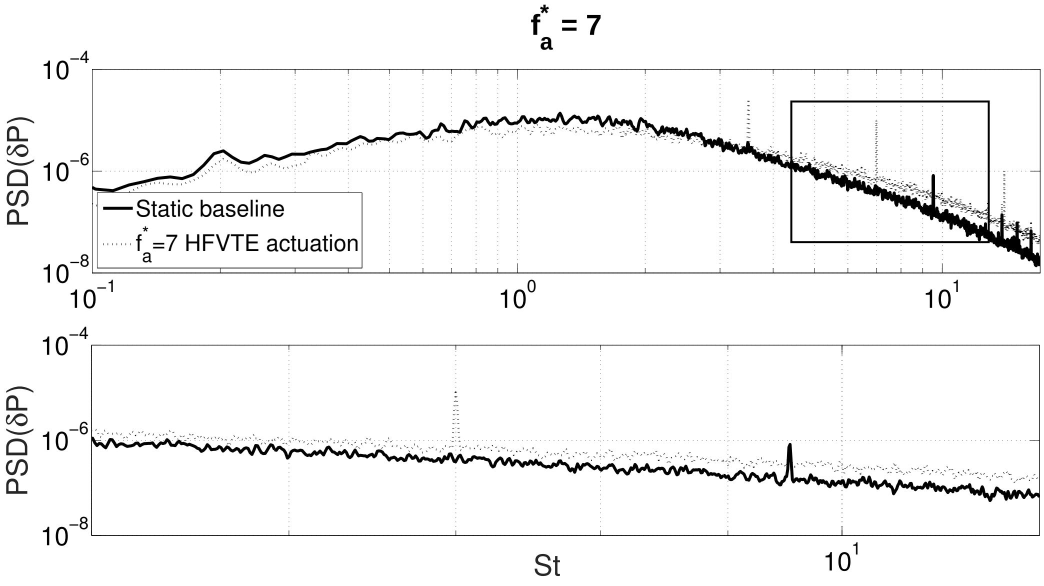

Figure 3.31: PSD of pressure fluctuations measured on the wing section with actuation at $f_a^* = 7$ (210 Hz) and without actuation. On the bottom the same plot is blown up around $f_a^* = 7$ (210 Hz).

Quantity	Percent difference between actuated and non-actuated
Variance (RMS)	-7.66%
Skewness	-36.25%
Flatness	13.03%

Table 3.3: Percent difference in statistical moments between the measures at $f_a^* = 7$ (210Hz) and those of the static configuration.

The actuation at $f_a^* = 7$ (210 Hz) leads to a smaller variance with respect to the baseline configuration. This is consistent with the results obtained in terms of drag. Indeed a reduction in the flow instabilities related to large vortical structures, i.e., in the pressure variance, yields a decrease in pressure drag. The skewness is related to instabilities in flow statistics. For a more stable wake, with less intense shedding phenomena, a smaller skewness (to be meant with sign) is expected. Actuating at $f_a^* = 7$ (210 Hz) provides a reduction in skewness with respect to the static configuration, accordingly to the measured drag downturn. The increase in flatness encountered for the actuated case is also in agreement with the observed drag reduction. Indeed flatness is larger for more regular flows, where weaker shedding phenomena are encountered. This actuation provides a vortex breakdown for the largest coherent structures and yields an upscale in the turbulent cascade from smaller scales towards larger ones.

Similar results on forces can be found at lower velocities. Figure 3.32 presents lift measurements from an accurate balance at Reynolds number $Re = 500$ k. Depending on the actuation frequency, lift improvement above 2% is measured. Each of the measured points in Figure 3.32 comes from two different runs. The sequences of the tested actuation frequencies have been randomly generated to avoid any dependence from a measure to another. Lift measurement accuracy has been evaluated to $+/-$ 0.3% for this experiment.

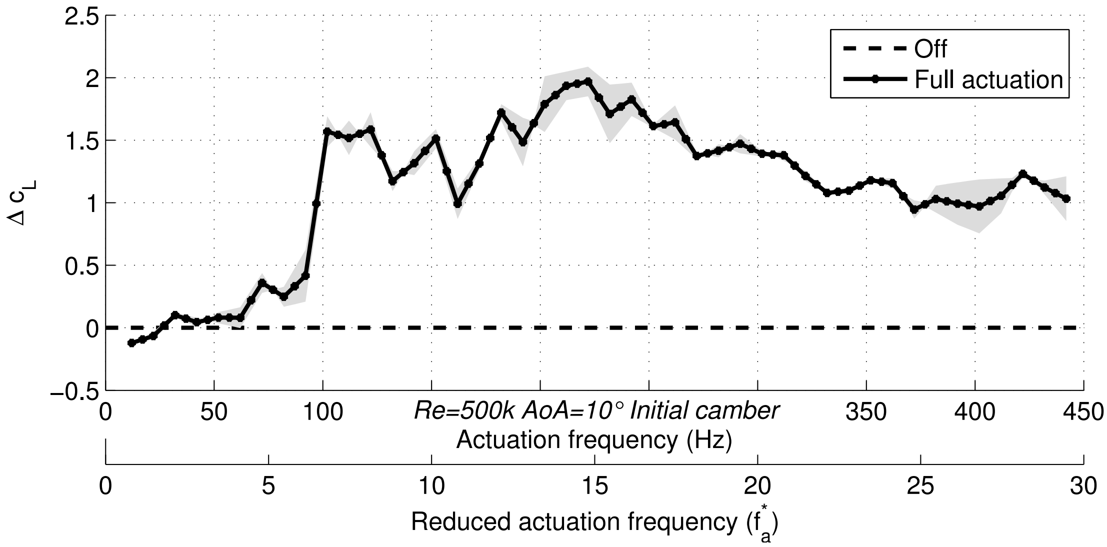

Figure 3.32: Percent gain of mean lift coefficients obtained with maximal HFVTE amplitude actuation, relative to the non-actuated case. Experiments are done at $Re = 500$ k

3.9 Conclusion

This chapter presents an experimental study of the electroactive morphing effects on the aerodynamics and time-dependent flow structures in the wake of an Airbus A320 aerofoil with piezo-actuated vibrating trailing edge. Camber control has been achieved using Shape Memory Alloys. Therefore, high frequency-low amplitude trailing edge actuation has been performed by wind tunnel tests. The angle of attack was set to 10°. Velocity measurements have been carried out at $\mathrm{Re} = 0.5 \cdot 10^6$ in the near-wake region by TR-PIV. A detailed investigation of the mechanisms modifying the eddy structure due to morphing has been done by means of the averaged velocity fields, Proper Orthogonal Decomposition and by spectral analysis. The aerodynamic forces and wall pressures on selected points have been measured by means of an aerodynamic balance and pressure transducers, respectively. A specific range of cambers and trailing edge vibrations have been depicted yielding a significant increase of lift in the order of 27%, where 4% are achieved thanks to the small amplitude vibrations. Concerning the neutral configuration (clean wing), the piezo-actuated Higher Frequency Vibrating Trailing Edge significantly affects the flow response. Namely:

- a vortex breakdown is observed for the largest coherent structures;
- an upscale energy transfer from smaller scales towards larger coherent eddies occurs. A significant reduction of large scale instabilities is obtained – approximately 20 dB power reduction (99.9%) of the predominant frequency peak is obtained.
- a reduction in pressure drag and an increase in lift are observed. Approximately 5% of drag reduction and a 2% lift enhancement is measured in optimal conditions. *Beyond this study, such macroscopic changes are linked significant changes in wake dynamics. Important reduction in wake's width together with effects upstream the actuation are visible on PIV measures of Figure 3.14.*

A wise choice in amplitude and actuation frequency has to be made to ensure the benefits without creating unwanted actuation-induced vortices. The present chapter substantiates the potential feasibility of hybrid morphing actuation as a novel means of improving aerodynamic performance by manipulating the near wake turbulence.

In a next step, the coupling between the camber control and the vibrating trailing edge is to be investigated in more detailed. Finally a closed loop control based on the best actuation frequency is currently studied.

Acknowledgements

The authors are grateful to Airbus and RTRA-STAE Foundation as well as the Direction Generale de l'Armement - DGA that provided funding for this research. The authors are also grateful to Dominique HARRIBEY, Karl Joseph RIZZO, Robert LARROCHE, Sébastien CAZIN, Moïse MARSHALL, Christophe KORBULY, Gilles HARRAN and Philippe MOUYON for their useful advice and help.

CHAPTER 4

Design through optimization: true scale cambered control flap

"Everything should be made as simple as possible, but not simpler."
Albert Einstein

This chapter is written like an article and will be soon submitted.

Figure 4.1: Word cloud of this chapter content (`www.wordclouds.com`).

Abstract Morphing requires a structure flexible enough to be easily deformed whilst being stiff enough to withstand the aerodynamic loads. This paradox leads to current issues in skin and actuator design. This cahpter presents a multi-criteria optimization process that considers the wing as a system doing different functions. Each function is addressed through different technological solutions. Different solutions for articulations, agonist-antagonistic shape memory alloy actuators, skin or feathers are described in the chapter. Taking into account industrial constraints, the optimization results in a feasible, low weight, low power consumption morphing wing design. Finally the optimal wing is designed based on the feasible optimized result.

4.1 Introduction

This work takes place within the design of the Large Scale Prototype of the ongoing European project SMS[1]*, as detailed in the outlooks of this manuscript 4.7.*

Limiting energy consumption has become a central concern for reducing the aircraft operational costs. Improving aerodynamic performance is a way to reduce the fuel consumption during flight.

Current airfoil shapes are generally optimized for one working point, corresponding to nominal cruise conditions. During flight, the altitude, the weight and the speed are continuously changing. Hence this design is suboptimal for the whole aircraft mission. Traditional solutions to control and adapt the wing shape (like slats and flaps) exhibit limited performance ranges [Bar+11]. Changing the shape of the wing during a mission can save several percents of fuel for a regional passenger aircraft [LM15]. The concept of real time shape adaptation enabling multipoint optimization is called morphing.

Within the framework of aircraft aerodynamic performance, morphing has been known for decades [Bar+11]. It was demonstrated that camber control of the trailing edge of a wing is very efficient to improve airliners performance by Lyu et al. [LM15]. It is also shown that morphing applied to a limited part of the airfoil chord may feature effectiveness comparable to that of entirely morphed airfoils. Additionally, the required deformations result in a change of camber by about 2% of the wing chord length, which corresponds to 7% of the flap chord length.

Despite the fact morphing wings have been used for military fighting aircrafts, research concerning industrial passenger aircrafts has not led to commercial appli-

[1] `http://smartwing.org/SMS`

cations. One can explain this as technology is not mature enough, the potential gains are known but reliability, maintenance, mass and power consumption of the added devices deteriorate the assessment. The skin or the interface between the structure and the outside airflow is the current technological bottle neck. Some studies simply do not deal with this issue (experiments at low velocity do not exhibit issue with elastomeric skins), others propose a degraded skin (i.e. corrugated skin for example that cause turbulent transition). As the skin is a part of the morphing system, it has to be taken into account. Thill et al. [Thi+08] draw review of morphing skin and its challenges. With this regard relatively high Technology Readiness Level (TRL) projects, targeting current industrial airliners at true scale, were undertaken. The European research program SARISTU[2] focuses on operating cost reductions as well as on improving the aerodynamic performance. One work package of SARISTU deals with a morphing wing trailing edge [Dim+16]. The device is based on servomotors driving an articulated structure. The European research program CleanSky[3] works in this direction as well. It focuses on a flap with twofold actuation, provided by servomotors and redactors respectively [PAM16]. The dual actuation allows for camber control during the different flight phases/assets. Another trailing edge morphing concept, called Adaptive Compliant Trailing Edge, was developed by NASA in cooperation with FlexSys Inc.[4]. This concept features an adjustable structure which can be actively deformed. Endurance flight tests for this concept were performed and described in Ref. [KFC16]. This solution was proved to yield aerodynamic benefits and its effectiveness and airworthiness are being ultimately assessed.

However these new adaptive structures are actuated through conventional actuators like electromechanical or hydraulic servomotors. Recent advances in the field of smart materials show the potential to overcome difficulties to make a wing both stiff enough to withstand the loads, and flexible enough to be easily deformed [Bar+14]. The related research focuses mainly on low TRL, mainly applied to low scale Micro Air Vehicles. Among electroactive materials, Shape Memory Alloys (SMAs) are the most frequently used. SMAs are characterized by thermomechanical behaviors, and most applications use an electrical resistor or the resistance of the SMAs themselves to activate the transformation. Different morphing concepts were developed, an overview of which is presented by Barbarino et al. in [Bar+11]. A counter example of the low TRL research is a recent industrial application of the SMAs within the Boeing CLEEN research program. A topic of the program consists in a flap actuated by a SMA twist tube, [CM16]. Safety issues have been solved using a redundant hydraulic actuator. It also provides brake

[2]http://www.saristu.eu
[3]http://www.cleansky.eu/
[4]http://www.flxsys.com/

and damping functions to maintain a deflected flap without requiring actuation energy. A flight test campaign has been successfully done, reaching TRL 7.

In the works previously mentioned the desired operation is generally accomplished using one specific smart material. But a combination of different smart material leading to a synergy is possible. As the SMAs can achieve large deformation at low speed, and as piezoelectric material can achieve small deformation at higher speeds, a combination of both material can enhance the global performance of the actuation. This is the proposed approach of the *synergistic smart morphing aileron* [PFI15]: the combination of a SMA actuated hinge followed by a flexible piezoelectric driven trailing edge. Another approach is an airflow point of view. Lift and large flow instabilities can be controlled through camber control whereas smaller instabilities responsible for drag and noise can be modified through active turbulence control of the trailing edge wake's shear layers. For ten years of collaborative effort from two laboratories (LAPLACE and IMFT) this approach has been leaded to the *electro-active hybrid morphing* concept: a low frequency (< 1 Hz) camber control ($\sim$10% of the chord) thanks to SMAs and a higher frequency vibrating trailing edge (fractions of millimeters up to 400 Hz). It was demonstrated that the flow dynamics are significantly affected by the trailing edge actuation. The wing's wake energy was reduced, leading to an improvement in aerodynamic performance, according to Sheller et al. in [Sch+15].

Based on an Airbus commercial aircraft, this chapter deals with a morphing flap design. After firstly describing the morphing flap concept with design requirements; different used technologies for actuator, skin and hinges are modeled. Thirdly, the optimization problem is described before presenting important results. Finally the chosen design is followed by a conclusion.

4.2 Morphing wing concept and modeling

The proposed morphing concept is applied to a flap but the assumptions are valid for a whole morphing wing. The function assessed by the proposed morphing is to adapt the wing shape configuration. This allow to change the shape that correspond to lower drag for every flight step. The high lift function is not addressed so that safety is not critical for this function. The morphing flap is based on an articulated ribs where Shape Memory Alloy actuators control the rotations of the elements around the hinges. This concept is firstly described. Then input geometry and loading are defined before the modeling of the whole camber controlled flap.

4.2.1 Articulated concept

The proposed concept, presented in Figure 4.2, is decomposed fourfold:

- *articulated ribs* define the geometry and carry the other components. They have to withstand the internal and external (i.e. aerodynamic) forces, whilst being low weight.

- *hinges* allow the rotation of the articulated ribs. Parts of forces are transmitted through these components without generating much parasite force (or torque) when rotated.

- *actuators* are devices that transmit mechanical energy to the structure. The actuators are responsible for the shape control and have to counteract aerodynamic forces as well as some internal forces coming from the other components.

- *skins* or covering devices guarantee the airtightness of the wing, transmit the aerodynamic forces to the structure and ensure a smooth shape during morphing. The skin must endure deformation without unexpected displacements like bumps or wrinkles.

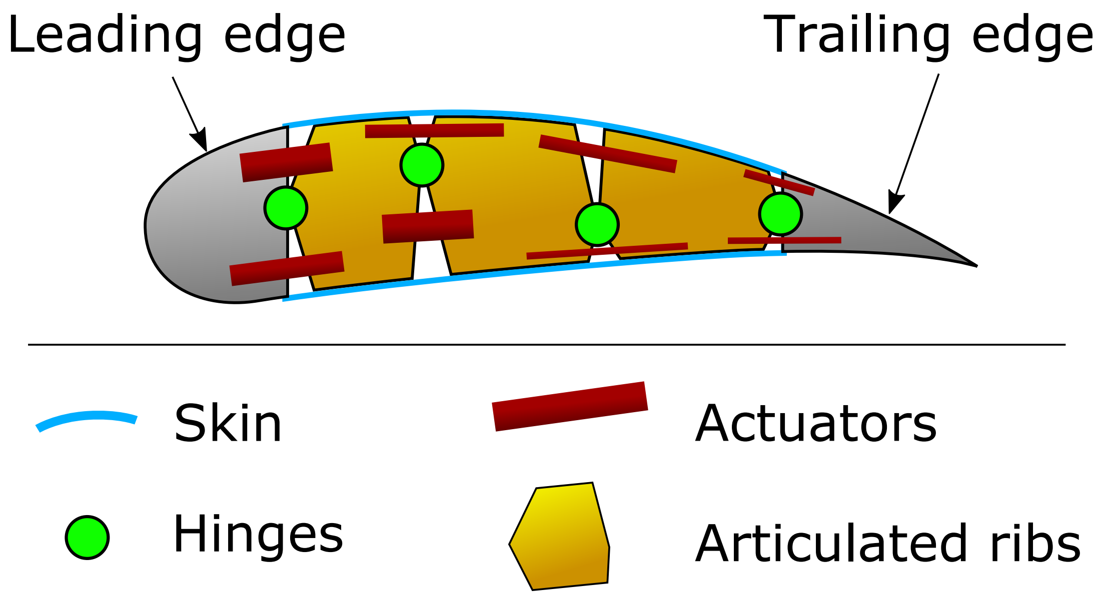

Figure 4.2: 2D illustrative sketch of the proposed concept. Articulated ribs are placed between fix leading edge and trailing edge. Actuators and specific skins are located within the morphing flap.

Additionally, mechanical stops are provided to limit the rotations of the articulations, thus preventing overloads in actuators. The internal structures represented by the articulated ribs actually consist in an engineered mechanical structure composed of ribs and spars. The fine design of this structure is outside the scope of this study, it is accepted that the lower the force in the structure, the lighter the structure. The proposed actuators consist in cylinder like actuators. Composed of shape memory alloy wires, they are able to pull on the articulated ribs, thus imposing the rotations. More detailed are presented in 4.3. One can notice the presented concept is not breakthrough, but the original purpose of this study is the comparison of the different technologies that can be applied.

4.2.2 Requirement and objectives

The previous concept performance assessment is based on a representative flap of an industrial passenger aircraft. To simplify the design, the flap's aspect ratio is assumed rectangular, with 1 m chord by 2 m span. The airfoil profile is presented in Figure 4.3. The morphing region targeted in the present chapter extends from 15% to 75% of the chord length. The trailing edge is committed to the integration of a Higher Frequency Vibrating Trailing Edge, corresponding to an actuation concept that manipulate the turbulence to enhance aerodynamic performance, developed in other studies of the authors, [Sch+15] and [Sch15]. The specified load is also presented in Figure 4.3. This vertical surface force distribution is assumed vertical and constant along the wing span. Globally, the resulting aerodynamic force on the 2 m span flap is about 1 ton force. One can notice that the higher force density are located at the trailing edge, thus the rear part of the wing carries lighter forces; this is beneficial for actuation requirements. This force specification is representative of nominal working points of the flap during all flight conditions where actuation is needed.

Regarding the objective, a flap design must perform the camber control function. Two objectives shapes are defined. Starting from the neutral initial shape, the flap can reach a low cambered shape (corresponding to upward displacement of the trailing edge tip) or also a high cambered shape (corresponding to a downward displacement of the trailing edge). The two objective shapes are presented in Figure 4.4, on the top two red airfoil profiles. According to the optimized shapes from [LM15] as well as Airbus specification, a vertical trailing edge tip displacement by about 7% of the flap chord is enough to optimally increase the cruise performance – 10% is selected for the design of a proof of concept. The profiles' deformations have been interpolated by polynomial; then the polynomials are applied to current flap profile to obtain the high and specified low cambered shapes. Finally, the optimized designed flap has to respect the morphing shape while being as lightweight and low-energy consumer as possible – the objective formulations are detailed in the following.

4.2.3 Model

As the morphing concept and its objective and specifications are defined, the optimization model is now defined.

4.2.3.1 Shape calculation

Starting from the positions and the rotation angles at every hinge, the profile is cut in sections corresponding to the different ribs sections. Then, using rotation matrices, every section is rotated. After the calculations of the new positions of the hinge centers, the rotated sections are assembled together. It results a deformed flap which is lightly faceted. To evaluate the relevance of the obtained shape, vertical position differences between the obtained shape and the objective shape are calculated for the upper and lower side of the airfoil profile. For each of the two ob-

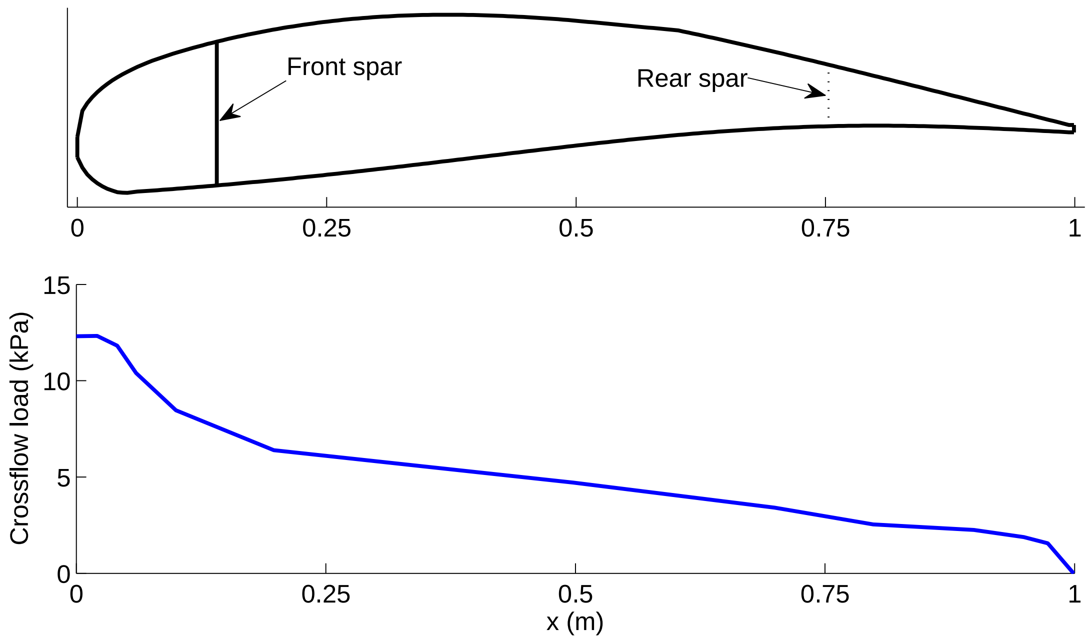

Figure 4.3: Top: Airfoil profile. Camber controlled part is located between the front spar and the rear spar. Bottom: distribution of the resultant surface vertical force loading.

jective shapes, articulation angles are found by minimizing the difference between the current articulated flap profile and the targeted profile. The function's cost is defined as the sum of the mean absolute error plus the maximum absolute error. This minimization is done thanks to a multi-variable gradient based constraint algorithm[5]. Figure 4.4 presents an optimized articulated flap with superimposed objective.

4.2.3.2 Force balance

Figure 4.5 schematically represents an articulated flap with four hinges. The leading edge is recessed in the spar. Actuators are present at every articulation, in parallel with the hinge. As the morphing displacement is slow, quasi-static assumption is done, thus the Newton's second law can be applied on a selected wing section Ω comprising a rib section and all the following ones until the trailing edge.

[5]Mathwork MATLAB *fmincon* function.

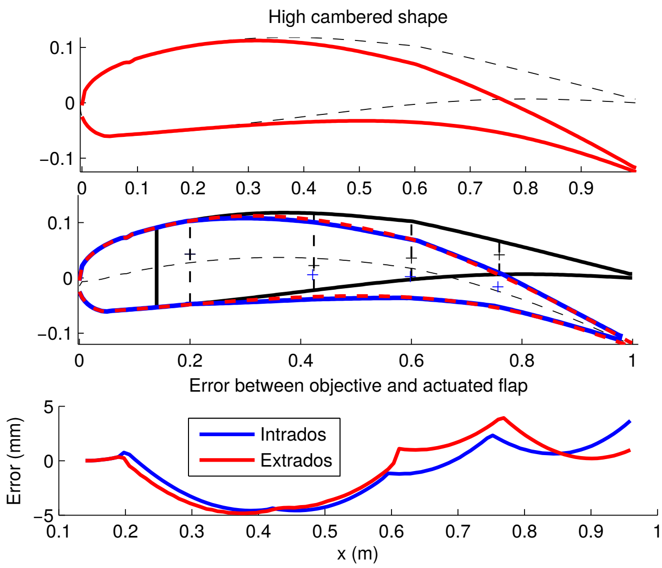

(a)

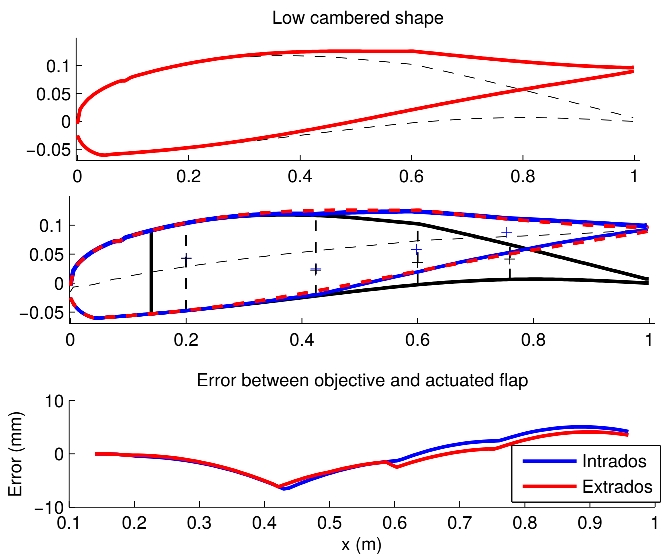

(b)

Figure 4.4: From top to bottom: The two objective shapes superimposed with the original non-deformed profile; deformed shape of the articulated morphing flap fitting the objective; error between the articulated flap and the objective. (b) presents the low cambered shape with upward trailing displacement, whereas the high cambered shape characterized by downward trailing edge displacement is presented in (a).

An example of the selection is blue highlighted in Figure 4.5. The resulting forces and moments expressed at the hinge location are:

- *Actuators*' participations: Force $F_{act} = \Sigma F_{act_i}$ and $M_{act} = \Sigma F_{act_i} \cdot l_i$, where l_i are the lever arms. The actuators inside the selected wing section Ω.

- *Hinge*'s participations: Parasite moment due to elasticity or friction in the hinge M_{hinge} and F_{hinge} the resulting force transmitted to the previous rib through the articulation.

- *Aerodynamic forces*: Resulting force $F_{aero} = \int_\Omega P(x) \cdot dx$ and resulting moment $M_{aero} = \int_\Omega P(x) \cdot x \cdot dx$

The force balance is presented in equation 4.1.

$$\begin{aligned} F_{hinge} &= -(F_{act} + F_{aero}) \\ M_{act} &= -(M_{hinge} + M_{aero}) \end{aligned} \tag{4.1}$$

Two important results sum up this balance: 1- the force transmitted to the previous ribs F_{hinge} allow the sizing of the hinge; 2- the resulting moment allow for the sizing of the actuator moment M_{act}, where the actuators' forces and lever arms are design variables.

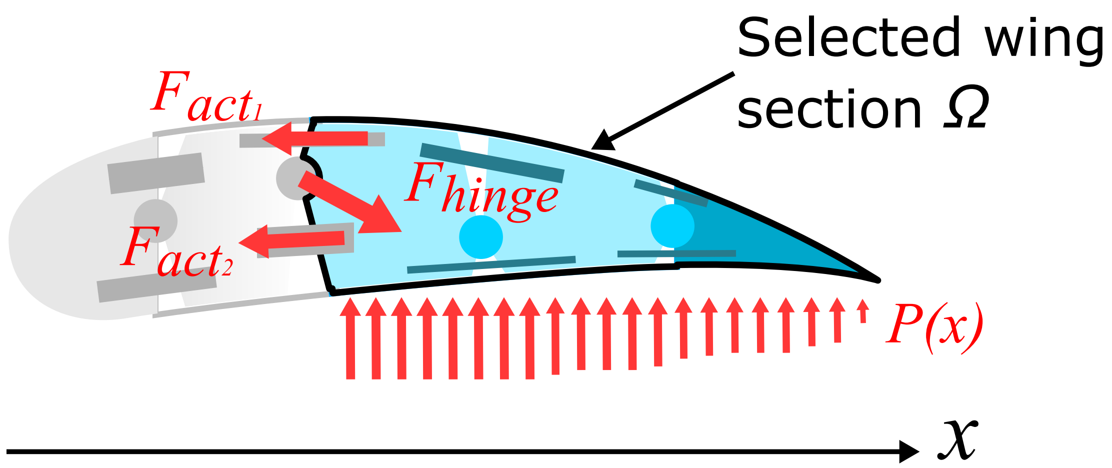

Figure 4.5: Sketch of the flap's force balance model. Among the 4 articulations of this design, the force balance is presented for the 2^{nd} one. The parasite hinge moment is not represented for greater clarity.

4.2.3.3 Hinge technologies

Various technologies realize mechanical articulations between two parts at low rotation angles. The specifications of the articulations are to transmit the forces with minimal movement in every direction and rotation. Excepted for the rotation axes where the parasite torque has to be minimum. The articulations have to be as light as possible and fit with the available room. Then two technological families exist. The first one is based on deformable parts, i.e. metallic bending beams or elastomer links. The behavior of such hinges can be modeled as elastic links, thus the parasite moment is linked to the rotation angle and the stiffness of the hinge. This stiffness is determined by the sizing that depends on the transmitted forces. The second family is based on gliding bearings. As the rotation angle and velocity ranges are small, ball bearings are not suitable. The parasite torque is due to friction, which is linked to the transmitted forces.

These different hinge technologies have been compared regarding the morphing flap sizing. For brevity purpose, the models are not detailed. For gliding bearings and elastomer links, routines have been coded to automatically select a hinge within a subcontractor catalog that fits the requirements. For the metallic bending beams, the beams must be as flexible as possible whilst withstanding the load with no buckling. To avoid large translations, the beams have to be as shorter as possible, but thin enough to stay slim. A routine has been coded to size the elastic beams while respecting the constraints. All these routines are parts of the sizing code described in this chapter.

4.3 Actuator modeling

The proposed morphing concept relies on actuators using Shape Memory Alloy (SMA). This section first shows that SMAs are suitable for the actuators. Then actuators are modeled and actuation topologies are described. It is important to notice that non linearity like material hysteresis, slake SMA wires or dependencies between actuators are not discussed in this chapter. Those specific issues are assumed to be addressed by suitable controllers.

4.3.1 Shape Memory Alloy behavior

Amongst smart materials, SMA are metallic alloys that exhibit an impressive thermo-mechanical coupling, due to crystallographic phase changes at microscopic scale. They have been studied for decades, Lexcellent draws a complete handbook about SMAs, [Lex13]. The most common are based on Nickel-Titanium alloys

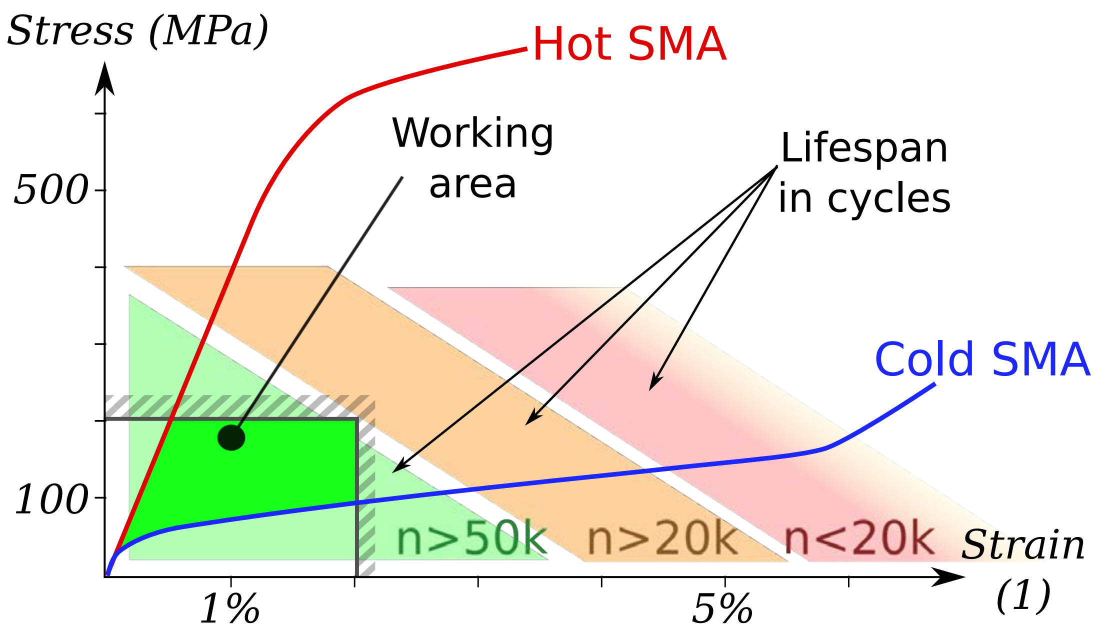

Figure 4.6: Tensile test of SMA wires at two temperature. Areas $n < 20$k, $n > 20$k and $n > 50$k respectively indicate that for actuators working in these areas, less than $20,000$, more than $20,000$ and more than $50,000$ cycles can be expected. Below the 200 MPa and 2% limits lies the specified working area.

with small amount of chemical additives to tailor thermo-mechanical properties. Basically, cold SMA is martensitic which exhibits low stiffness and pseudo-plastic behavior. Hot SMA is austenitic, characterized by a higher stiffness and super-elastic behavior. This two-material in one withstands strain levels up to 7% and stress level up to 600 MPa, as presented by hot and cold stress-strain characteristics in Figure 4.6. Its high specific actuation energy (about 1 kJ/kg), stainless property and growing maturity make this material of interest for aeronautic applications. SMA actuators are not designed in respect with the maximum stress and strain, but in respect with fatigue. A cycle life up to one million actuation cycles have been shown on small diameter SMA wires at limited stress and strain, [Jan+14]. Generally, the lower the diameter and strain-stress loading, the longer the cycle life. Areas drawn on Figure 4.6 indicate the expected maximum number of cycles. Therefore, a reliable design relies on a specification area where the working points are included. To ensure about 100,000 cycles with 1.5 mm diameter for the first demonstrator, limits are set at $\sigma_{SMA\ max} = 150$ MPa stress and $\epsilon_{SMA\ max} = 2\%$ strain. This choice allow a wire section large enough that limit the number of wires to be integrated; this eases the prototype assembly.

4.3.2 Actuator model

The previously described SMA are integrated in actuators. Based on back and forth wires to increase the force, the proposed actuator concept is like a cylinder that pull only – as the wires can only work in tension. This actuator is clamped on two following ribs that are articulated. The active length (i.e. relaxed SMA length) L as well as the lever arm h have to be within feasible limits ($L \leq L_{max}$, $h_{min} \leq h \leq h_{max}$) that depends on geometry and manufacturing possibilities. Figure 4.7a illustrates a hinge with one actuator at neutral position; geometric parameters are indicated. The actuator's forces applied on the anchors are presented as F_{act} and the moment at hinge axis due to the actuator applied from rib 2 to 1 is named $M_{act\ 2/1} = F_{act} \cdot h$. Figures 4.7b and 4.7c present the two extreme rotated shapes. The small angles assumption is made. If $h/L \ll 1$, it can be reasonably assumed that: lever arm h is independent from the hinge rotation, and actuator's stroke s is defined by $s = h \cdot \theta$.

The sizing of an actuator starts with the specification of:

- the actuator torque $M_{act\ 2/1}$ – detailed in global sizing algorithm, section 4.5.3,
- the angle range $\theta = \theta_u + \theta_d$ – from section 4.2.3.1,
- the geometric limits L_{max}, L_{min}, h_{max}, h_{min}.

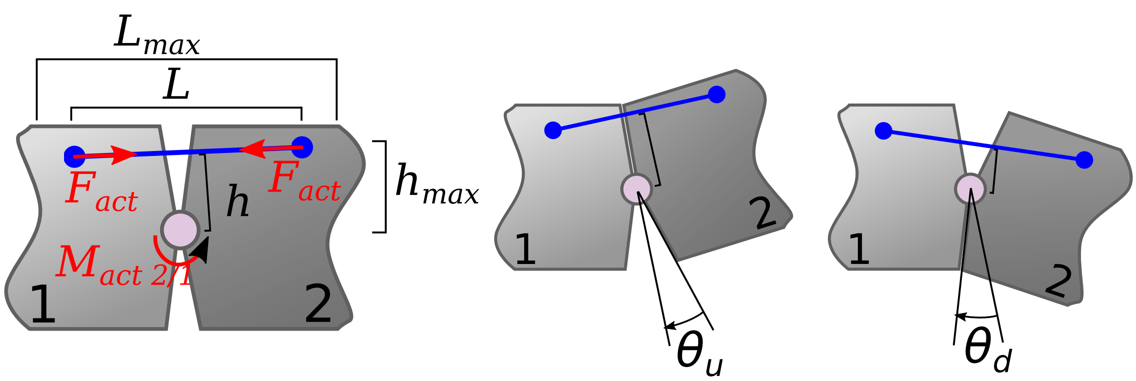

(a) (b) (c)

Figure 4.7: (a) Parametrized sketch of an actuated articulation. (b) Rotation when actuated, the maximum rotation angle is θ_u. (c) Rotation when non-actuated, the mainimum rotation angle is θ_d.

The sizing Algorithm 1 describes the calculation of the lever arm h, the force F_{act} and other properties like the mass of the design actuator. A flag giving information about the successful design is output. It is used to penalize a flap with non feasible actuators, without crashing the computation. The total mass of the actuator is evaluated, as well as the power consumption. This is done with results from a thermal analysis of the actuator, non presented here for brevity purpose. Assuming a cylinder like actuator, with a passive cooling and a cooling time of 60 s in nominal conditions, the insulation cover thickness and the power consumption are evaluated. It can be shown that independently of the exact shape or topology, a good approximation of power consumption per kilogram of SMA during heating is 960 W/kg whilst 295 W/kg seems enough to maintain the maximum temperature at minimum ambient temperature.

Algorithm 1 Actuator sizing algorithm

```
procedure ACTUATOR SIZING(M_act 2/1, θ, Geometric limits, SMA limits)
    L = L_max                              ▷ First, try with maximum available length
    h = ε_SMA max · L_max/θ                ▷ corresponding lever arm
    Flag = ok                              ▷ A priori there is no design issue.
    if h < h_min then                      ▷ Design within limits?
        h = h_min
        Flag = Aging issue                 ▷ We do not respect SMA limits
    else if h > h_max then                 ▷ There is too much length available
        h = h_max                          ▷ Limits the lever arm, then calculate the new length
        L = h · θ/ε_SMA max
        if L > L_max then                  ▷ New design over limits?
            L = L_max
            Flag = Aging issue             ▷ We do not respect SMA limits
    F_act = M_act 2/1/h                    ▷ Evaluate force
    ε_act = h · θ/L                        ▷ Effective strain
    S_SMA = F_act/σ_SMA max                ▷ actuator's SMA section
    Evaluate mass and power consumption with amount of SMA, anchors' masses
depend on force, case's mass depends on dimensions.
    return L, h, masses, Flag
```

4.3.3 Antagonistic actuation concept

This subsection deals with the actuation topology. As the SMA actuators can only pull, a device has to be implemented to recover the initial shape. Additionally the aerodynamic forces are not always present so they cannot be the only way to be used to recover the non-actuated shape. Two solutions are compared: a passive counter-spring and an antagonist SMA actuator. To chose between the two technologies, the representative comparison cases are presented in Figure 4.8.

A first approach is a simple analytical modeling. For the counter spring concept, respectively the antagonist concept; it is assumed the forces applied on articulated ribs are the actuator (force F_{act}) and the counter spring (force F_{sp}) or respectively the antagonist actuator (force F_{ant}). Force moments are calculated at hinge's center. The lever arms are noted h_1 and h_2. The usable output torque is M_u. SMA actuator minimum force is $F_{act\ cold}$ and maximum force is $F_{act\ hot}$. The counter spring is assumed as a linear spring, with its stiffness K_{sp} and its relaxed length L_{sp0}.

Considering the counter spring solution, the spring moment at hinge center is expressed in equation 4.2, where δL is the spring pre-strain.

$$\begin{aligned} M_{sp} &= h_2 \cdot K_{sp} \cdot (h_2 \cdot \theta) + M_{sp\ 0} \\ M_{sp\ 0} &= h_2 \cdot K_{sp} \cdot \delta L \end{aligned} \tag{4.2}$$

The counter spring aims to counter act the cold SMA force from the actuator to recover the initial shape. The counter spring pre-strain must apply a minimum moment equal to the opposite of the cold SMA moment. In order to limit the exceed in this force, the stiffness K_{sp} have to be minimize, this is possible by selecting a low stiffness spring with a high pre-strain. For integration reason, the pre-strain is reasonably limited to 70% of the actuator length L_{SMA} ($\delta L = 70\% L_{SMA}$). The torque balance gives the expression of the output moment in equation 4.3. This equation also contain the resulting force F_X in the hinge.

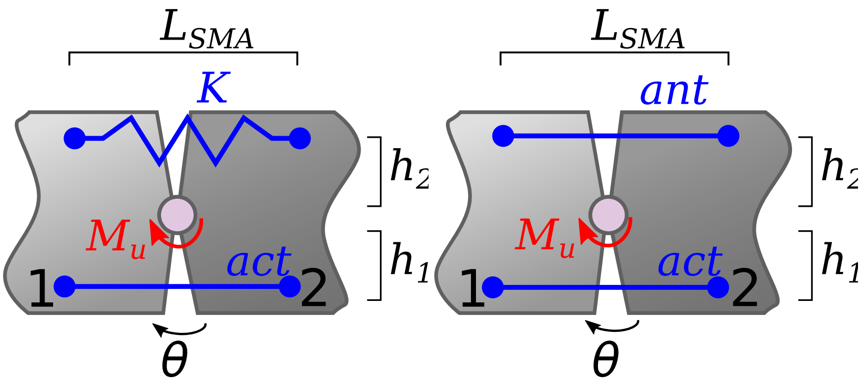

(a) Counter spring concept. (b) Agonist-antagonist concept.

Figure 4.8: Sketch of the two compared solutions.

$$
\begin{aligned}
\text{Maximum actuation: } M_u &= F_{act\ hot} \cdot h_1 - F_{act\ cold} \cdot h_1 \cdot (1 + \frac{h1 \cdot \theta}{\delta L}) \\
\text{Minimum actuation: } M_u &= -F_{act\ cold} \cdot h_1 \cdot \frac{h1 \cdot \theta}{\delta L} \\
F_X &= F_{act} + F_{act\ cold} \frac{h_1}{h_2}(1 + \frac{h_1 \cdot \theta}{\delta L})
\end{aligned}
\tag{4.3}
$$

Regarding the agonist-antagonist concept, the representation on Figure 4.8b distinguishes the actuator F_{act} and the antagonist actuator F_{ant} which is design to be actuated to counter act the cold actuator. The torque balance as well as the resulting hinge force are presented in equation 4.4.

$$
\begin{aligned}
\text{Maximum actuation: } M_u &= F_{act\ hot} \cdot h_1 - F_{ant\ cold} \cdot h_2 \\
\text{Minimum actuation: } M_u &= F_{act\ cold} \cdot h_1 - F_{ant\ hot} \cdot h_2 \\
F_X &= F_{act} + F_{ant}
\end{aligned}
\tag{4.4}
$$

We can see that the output torque of the spring solution depends on the rotation angle. With a more accurate model, the antagonist actuator also depends on the rotation angle but in a smaller way. To compare the two concepts, standard values are taken: $h_1 = h_2 = 50$ mm, $L_{SMA} = 150$ mm, for a SMA strain of 1.5% the maximum angle is $\theta_{max} = 2.6°$. Actuator forces are $F_{act\ hot} = 8,700$N and $F_{act\ cold} = 2,000$N. Results are summed up in table 4.1.

This simple example shows that internal forces are lower for the antagonist concept and the output torque is 43% higher than the counter spring concept, with the same SMA actuator. The fact that antagonists actuators can be “switched off” compared to counter spring that always applies the restoring torque explains the large efficiency difference.

The previous models do not take articulation parasite torque into account. The sizing algorithm has been applied to an articulated hinge for a range of output torques. The performance of the technologies are presented in Figure 4.9. The

Table 4.1: Force comparison of counter spring VS antagonist solutions.

Technology	actuated $M_u(\theta_{max})$	actuated $M_u(\theta = 0)$	$\max(F_X)$	Spring/antago force
Counter spring	557 N.m	565 N.m	$28,830$ N	$F_{sp}(\theta_{max}) = 8,830$ N
Antagonist actuator	811 N.m	811 N.m	$16,220$ N	$F_{ant\ hot} = F_{ant\ cold}$, $F_{ant\ cold} = 3,780$ N

total estimated mass of the actuators and hinges, the hinge force and the amount of SMA are drawn depending on the output torque. Computations of non-functional system without antagonist actuator nor spring is represented as "No return system" for comparison. Some jumps due to a change in hinge references are visible. The conclusion is significant: counter spring solution add forces that need larger total SMA amount and larger hinges.

Finally, despite the need of a more sophisticated control system, the agonist-antagonist actuator concept is more efficient than a counter spring. The solution is lighter, requires lower SMA amount with lower forces in the structure. According to integration point of view, the counter spring can be materialized by an elastic skin, as presented in the next Section 4.4. An analogy with biologic articulations can be made, a simplified vision is that elbows are actuated by two antagonist muscles (biceps and triceps). This natural solution is preferred than one large muscle with a counter spring materialized by tendons. Thus the agonist-antagonist actuator topology is selected for the morphing wing design.

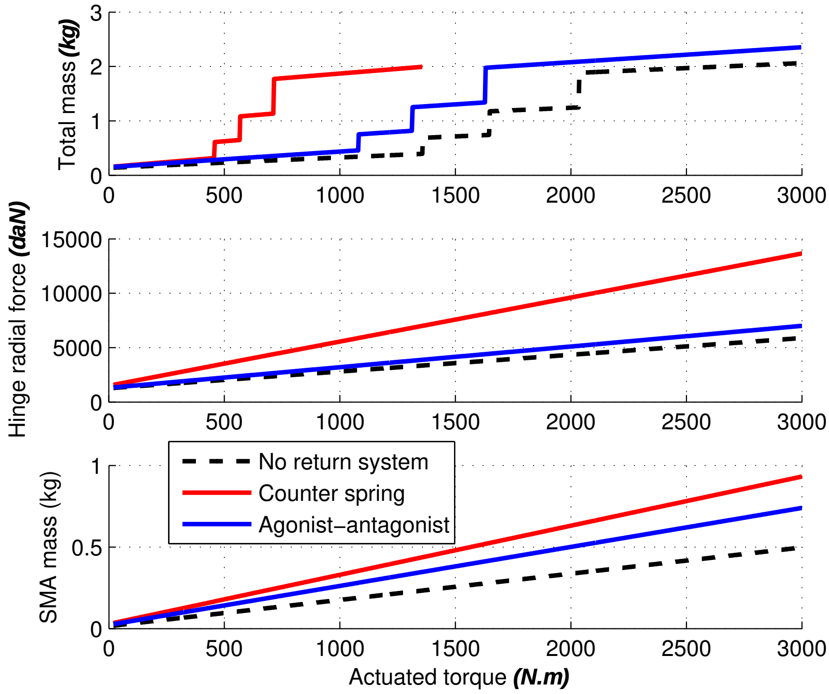

Figure 4.9: Performance of the counter spring and the antagonist solutions compared to the no return system.

4.4 Skin technologies and modeling

The skin is the device that covers the whole wing and defines the interface with the airflow. The skin for morphing wing is considered as the most demanding function. Thill et al. [Thi+08] draw a review of morphing skins within complete morphing systems. It is concluded that the combination of stiffness and flexibility is a major bottleneck. Indeed, the skin has to keep the airfoil profile fitting the required shape regardless to the deformations nor aerodynamic loading. Whilst carrying the pressure, the skin must be airtight, lightweight and consumes low energy. Some industrial specifications like temperature and environment compatibility, abrasion resistance or electric conduction are required.
Two different technologies are optimized and compared for the articulated flap: an elastic skin that covers the flap with some hung or free parts 4.4.1, and a promising innovative bio-inspired skin based on feathers 4.4.2. For both technologies, the specifications are to withstand the aerodynamic pressure with less than 1 mm deformation.

4.4.1 Elastic skin

The elastic skin concept consists in a taut membrane that is hung on the articulated ribs. The skin is free between the ribs at articulations levels, as presented in Figure 4.10. The free skin elements can be elongated when the articulations moves while the dynamic pressure tends to deform it.

To model the skin, one free element is focused on the detailed view in Figure 4.10. The free length is note L, T is the skin tension force (considering a span length $Span$) and H is the normal deformation due the pressure P (supposed constant on the free length). The skin is modeled as a membrane; but reduced to

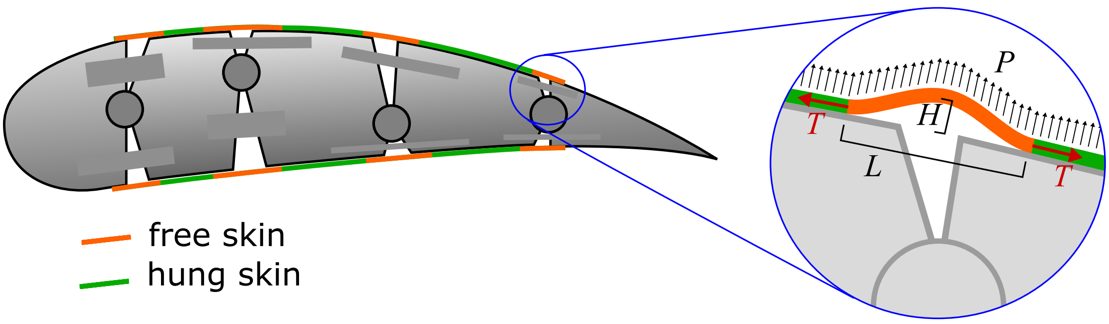

Figure 4.10: Morphing flap with elastic skin. Skin is hung when represented in green, whereas it is free and taut when represented in orange. The right part presents a detailed view of a parametrized taut skin element.

two dimensions, the skin is assumed to be modeled like a taut cable. The relation between the normal deformation and the other parameters is depict in equation 4.5. In a case corresponding to constant length L, a choice of the couple length, tension (L, T) is made to ensure a small normal deformation $H < H_{max} = 1$ mm. But due to the movements of the articulations, the skin length changes. Additionally the elasticity of the skin cause changes in the tension.

$$H = \frac{P \cdot Span \cdot L^2}{8 \cdot T} \tag{4.5}$$

Therefore, equation 4.6 models the skin as a pre-stressed elastic material; where t is the skin thickness, $\mathbb{E}$ its Young modulus and δL the skin extension due to articulation movements.

$$T = T_{pre} + \mathbb{E} \cdot t \cdot \frac{\delta L}{L} \tag{4.6}$$

The skin pre-stress T_{pre} corresponds to the minimum tension in skin when morphing movement impose minimum skin length. This tension is calculated from equation 4.5 to ensure a small normal skin deformation. When stretch, elastic force increase the skin tension thus ensuring small normal deformation. The dependence of T_{pre} as a function of the free skin length L is drawn in Figure 4.11. During morphing deformations, the skin's maximum extension δL add an important tension in the skin, inversely proportional to the free skin length L. The dependence of the elastic force is also drawn in Figure 4.11.

Therefore, the total maximum tension – drawn in Figure 4.11 – exhibits an optimum free length L that minimize the maximum tension. It is reminded that the lower the forces, the lighter the structure and the actuators. The formula of this optimal length L_{opt} with the corresponding maximal tension are written in equation 4.7.

$$\begin{aligned} L_{opt} &= \sqrt[3]{\frac{4\mathbb{E} \cdot t \cdot \delta L \cdot H_{max}}{P}} \\ T_{max} &= \frac{P \cdot Span}{8H_{max}} L_{opt}^2 + \mathbb{E} \cdot t \cdot Span \frac{\delta L}{L_{opt}} \end{aligned} \tag{4.7}$$

Finally, these equations are integrated in the design algorithm. This routine takes the skin displacement and the available room as inputs. It computes the free skin lengths and pre-stresses that fit the available room – optimum length are selected if possible. Outputs are the tensions that are transmitted by the hinges, and the maximum torques that actuators have to counter act, due to skin elastic forces when stretched during morphing.

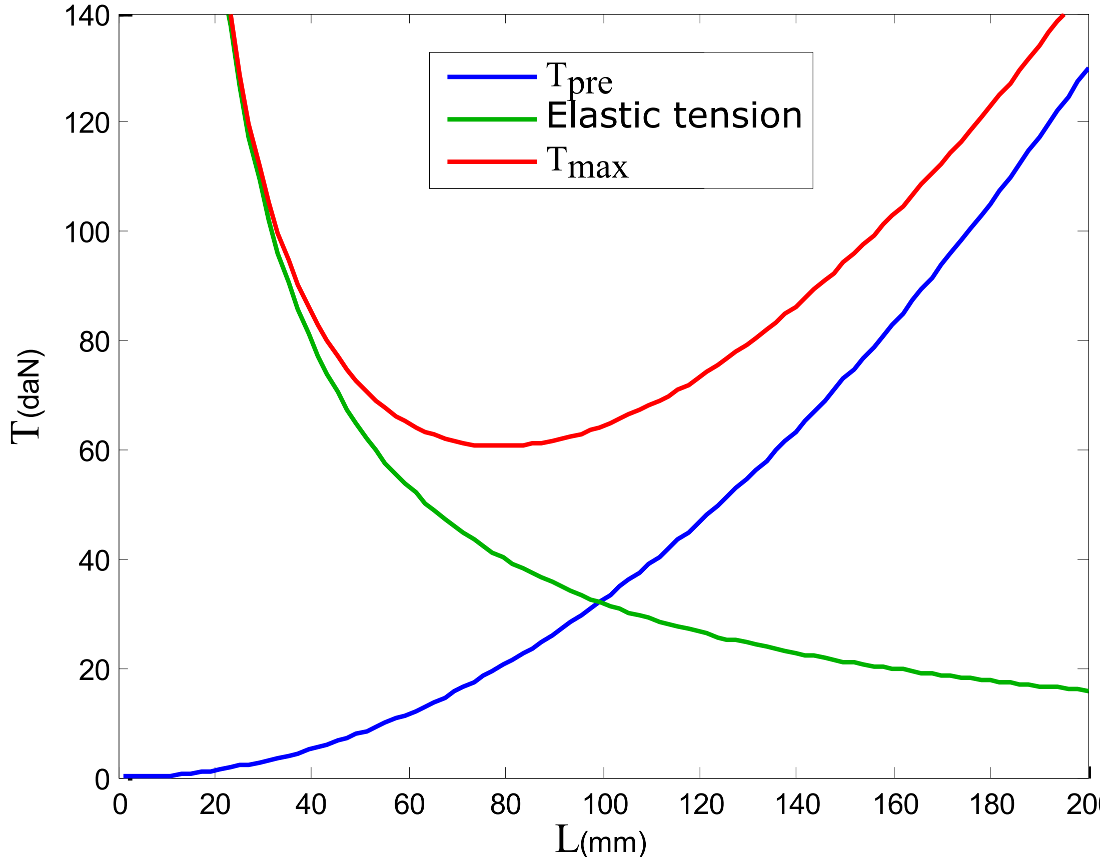

Figure 4.11: Illustration of skin tensions. The considered skin is an elastomeric coated fabric from Pennel & Flipo. The considered stretch is $\delta L = 8.5$ mm, for a 5 cm span.

An early result – detailed in section 4.6 – is that elastic skins require high tensions (about 3 tons for a 2 m span flap) that are transmitted through the structures and the hinge. These forces are much larger than aerodynamic forces, thus very heavy design is mandatory to carry these loads. Additionally, the skin stiffness consumes 60% of the actuator output energy so actuators have to be oversized to fulfill their functions. This early result confirms that the skin technology is a bottleneck for morphing purpose.

Figure 4.12 illustrates possible skin materials. The skin is a fabric based flexible composite that contains different layers dedicated to different requirements like stiffness and environment resistance.

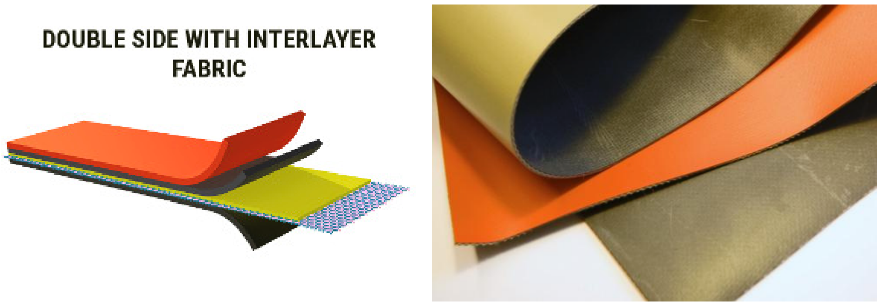

Figure 4.12: Illustration of ORCA products made by Pennel & Flipo.

4.4.2 Innovative feather and skin concept

The proposed innovative concept is bio-inspired from birds. Birds' bodies are covered by heterogeneous feathers. When a bird moves its wings, the wing profiles stay smooth, as the feathers glide on each others. If the feathers ensure the aerodynamic profile, birds have skin under the feathers to protect their bodies from the external environment. Inspired from this function decoupling, the proposed concept consists in an internal airtight skin and external gliding devices. The internal skin has no shape specification, but must be airtight to prevent internal airflow going outside and must carry the average aerodynamic loads. The external gliding devices, like artificial feathers, slide on the external profile and are thin enough to respect the 1 mm shape accuracy. Figure 4.13 presents the concept applied on one articulation.

The sizing of the internal skin do not require it to be extended so the forces due to the internal skin are neglected. Particular attention is paid to ensure there is enough room between the feathers and the actuators. The sizing of the feathers is decomposed threefold: geometric constraints, friction induced parasite torque , pressure induced deformation.

Geometric constraints concern the feather thickness t that must be under 1 mm, ($t < 1$ mm). The feather length L must be larger than the gliding length ($L > h \cdot (\theta_d + \theta_{op}$, where h is the articulation lever arm, θ_d and θ_{op} the extremal rotation angles). This second condition ensures the airfoil profile is always closed.

The friction induced torque comes from the calculation of the force exerted between the feather and the rib. Due to the rotation, the feather tip displacement y is evaluated. Assuming the feather is a cantilever beam in aluminum, the length have to be higher than a minimum value depending on the elasticity modulus $\mathbb{E}$ and elasticity limit σ_{max}. The maximum displacement y allows for calculating the contact force F_y with the rib (I stands for the second moment area of the feather cross section). Then, in the worth case corresponding to maximum deformation and force, the parasite friction torque M_{frot} is evaluated, depending on the friction

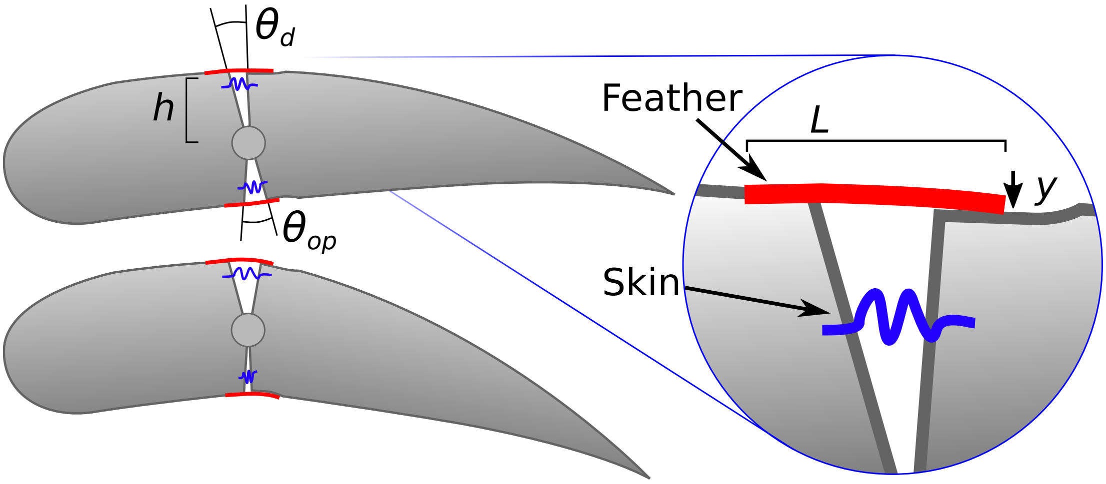

Figure 4.13: Skin and feather concept applied on one articulation. The flap is drawn for two rotation angles. A parametrized detailed view is also presented on right.

coefficient ν. Equations are detailed in equation 4.8.

$$\begin{aligned} y_p &= h \cdot tan^2(\theta_p) \\ L &> \sqrt{\frac{3y \cdot t \cdot \mathbb{E}}{2\sigma_{max}}} \\ F_y &= \frac{3y \cdot \mathbb{E} \cdot I}{L^3} \\ M_{frot} &= h \cdot \nu \cdot F_y \end{aligned} \tag{4.8}$$

The pressure induced deformations are static and dynamic. The feather tip deformation is calculated assuming the aerodynamic pressure is applied on only one side of the feather. This assumption is conservative because as the feathers are not airtight, the mean pressure between the feather and the skin is close to the outside mean pressure. The tip calculated displacement is very low (about 50 μm, for L = 15 mm, t = 0.5 mm), even within the conservative assumption. The dynamics aspects are important, feather flutter must not happen. Therefore, the first resonance frequency f_1 of the feathers are evaluated, thanks to equation 4.9 (cantilever beam, S is the cross section, ρ is the density). This frequency has to be high enough to avoid fluid-mechanic resonance; this condition is respected for every feather.

$$f_1 \approx \frac{1.875^2}{2\pi \cdot L^2}\sqrt{\frac{\mathbb{E} \cdot I}{\rho \cdot S}} \tag{4.9}$$

Despite of the different constraints, the skin and feather solution seems effective. Early results present feather of 0.5 mm thick, the longest ones are about 20 mm while the average length is approximately 6 mm. The parasite torques due to friction are always under 0.5 N.m, which represent less than 1% of the aerodynamic loads. First resonance frequencies of the feathers are above 2 kHz that is found to be acceptable. Finally, the algorithm's routine that size skins and feather only computes the needed length, as force or resonance constraints are always observed.

4.5 Optimization problem

Now that components are modeled, this section deals with a global flap sizing algorithm. The study aims designing a feasible and realistic flap, not the development of new optimization algorithm. Thus the computations are based on the genetic optimization algorithm from Mathworks' Matlab software.

4.5.1 Design variable

Previous sections 4.3.2 and 4.4 present methods that optimally size the actuators and the skin according to a given articulated geometry and forces. Then, actuators' lever arms, strokes and length, as well as skins' pre-tensions and free length or feathers' sizes are not design variables to be globally optimized. Nevertheless, hinges' locations as well as ribs where actuators are hold have to be selected. But to guaranty the controllability of each articulation angle, one actuator and one antagonist actuator are set between each consecutive articulated rib.

Thus the hinge locations remain to be optimized. The horizontal position (normed by the chord length) of the i-th hinge is named h_{Xi} while h_{Yi} is its relative vertical position (in % normed to the profile thickness). Hinge positions are limited within feasible making constraints, as summed up in equation 4.10, where N is the number of articulations.

$$\begin{aligned} \forall i \in [1:N], \text{Front spar} < h_{Xi} < \text{Rear spar} \\ \forall i \in [1:N], 30\% < h_{Yi} < 70\% \\ \forall i \in [1:N-1], h_{Xi} < h_{Xi} + 3 \text{ cm} \end{aligned} \tag{4.10}$$

Concerning the number of articulation N, shape optimizations with 2 to 7 hinges have been performed. Approximation errors – calculated in section 4.2.3.1 – due to the faceted profiles severely decrease up to 4 hinges. The gap between a 4 hinge flap profile and a 5 hinge flap profile has been found insignificant compared to the added implementation complexity.

As the internal structure is not precisely modeled in the sizing algorithm, the number of actuators spread along the span direction of the wing is not an important matter. A realistic compromise between force distribution and complexity is 4 actuators in the span. The optimization is then based on 50 cm span wingboxes, forming the 2 m span flap.

4.5.2 Cost and objective formulations

The sizing algorithm computes weights, power consumptions, shape approximation error, lifespan and penalization:

- The total weight W_{total} is the sum weight from the agonist actuators, the antagonist actuators, the hinges and an assumed simplified rib structure.
- The power consumption comes from the SMA activation, as explained in section 4.3.2. The maximum power is computed when heating all the actuators and antagonist actuators. The maintaining power P_{SMA} corresponds to the average power needed to maintain all the agonist and antagonist actuators at maximum temperature.
- The shape approximation errors are assessed like in section 4.2.3.1. S_{AV} is the average absolute error whereas S_{max} is the maximum absolute error.
- The lifespan concerns the actuators. The system expected lifespan is limited by the actuator with the lowest lifespan, noted L_{min}.
- Penalizations can be added, when sizing difficulties are encountered. Penalties are calculated when dimensions of dedicated actuator place are lower than the minimum lever arm, when there are not enough places for hinges and when the design is not converged. Additionally the number of different penalties is taken into account for the total penalty cost P_{enalty}.

To allow the optimization towards one optimal design, a unique cost must be defined from the different costs. A normalization is necessary. Costs like weight and power consumption are normalized to a representative value. The normalized shape cost is evaluated from the square of the averaged and maximum absolute approximation error. Cost related to the cycle life is proportional to the inverse of the expect number of cycles. Both shape and cycle life costs have a upper bound to prevent the optimization being piloted by these two costs only. The formulas corresponding to the cost normalization are summarized in equation 4.11, where

$.^n$ exponents are related to normalized costs.

$$\begin{aligned} W^n_{total} &= \frac{W_{total}}{5 \text{ kg})} \\ P^n_{SMA} &= \frac{P_{SMA}}{1.3 \text{ kW}} \\ S^n = (S_{AV}/2.3 \text{ mm})^2 + 100 \cdot (1 - e^{(-S_{max}/100 \text{ mm})}) \\ L^n_{min} &= 100 \cdot (1 - e^{(-10^6/L_{min})}) \end{aligned} \tag{4.11}$$

Finally, the definition of unique cost uses mixing ratios. The choice of the mixing ratios does not come from sound scientific criteria but from empiric criteria leading to a balance flap between the effective weight, shape approximations, power consumption and lifespan.

4.5.3 Cost function: sizing algorithm

The sizing algorithm that uses the previously modeled components is described in Algorithm 2. This algorithm corresponds to the cost function of the optimization problem.

Starting from a hinge distribution and sizing rules (i.e. SMA limits and geometrical parameters), the algorithm firstly computes the optimized rotation angles that best fit the specified shapes for both up and down morphing. The design is placed in the worth case regarding the position, so only the maximum rotation angle θ_i – defined in the present algorithm – are used. Then aerodynamic forces and skins are evaluated. Therefore the sizing of the different actuators and hinges starts. The specified actuator torques $M_{act\ i}$ correspond here to the actuator torques $M_{act\ 2/1}$ of the model presented in Section 4.3.2. The first sizing iteration considers unknown forces as zero, so the first design of the actuator does not take into account the cold antagonist actuators nor the hinge parasitic torque. Then the antagonist actuators are computed based on the cold actuator forces; and finally the hinges are computed knowing the forces of all the actuators and antagonist actuators. This first loop is followed by other sizing loops. Taking the previous antagonist actuators and hinge to size the actuators, several iterations are done until the modifications in the hinge parasitic torque or the force from the cold antagonist actuators do not change by more than 5%. It results a sized system where the actuators, the antagonist actuators and the hinges can work together. If the design does not converge within 13 iterations, the sizing algorithm stop with a penalty cost. The final step of the algorithm is the computation of all the costs, defined in the previous section.

Algorithm 2 Actuator sizing algorithm

procedure GLOBAL FLAP SIZING(h_{Xi}, h_{Yi})

    Compute rotation angles θ_{Ui} from *optimized shape*, *Up morphing*
    Compute rotation angles θ_{Di} from *optimized shape*, *Down morphing*
    $\theta_i = \max(\theta_{Ui}, \theta_{Di}, \theta_{Ui} - \theta_{Di})$ ▷ Angle ranges
    Compute aerodynamic forces on hinges $F_{aero\ i}, M_{aero\ i}$
    Compute forces and parasite torque of skin $F_{skin\ i}, M_{skin\ i}$
    $M_{act\ OLD\ i} = 0$, $M_{ant\ OLD\ i} = 0$, $M_{hinge\ OLD\ i} = 0$ ▷ Initialization
    ▷ Actuator sizing
    $M_{act\ i} = M_{aero\ i} + M_{skin\ i} + M_{hinge\ OLD\ i} + M_{ant\ OLD\ i}$
    Compute $F_{act\ i}$ from *actuator sizing*($M_{act\ i}, \theta_i$, Sizing rules)
    ▷ Antagonist actuator sizing
    $M_{ant\ i} = M_{act\ i} + M_{skin\ i} + M_{hinge\ OLD\ i}$
    Compute $F_{ant\ i}$ form *actuator sizing*($M_{ant\ i}, \theta_i$, Sizing rules)
    ▷ Hinge sizing
    $F_{hinge\ i} = F_{act\ i} + F_{aero\ i} + F_{skin\ i} + F_{ant\ i}$
    Get $M_{hinge\ i}$ from *hinge selection*($F_{hinge\ i}, \theta_i$, Sizing rules)
    do ▷ Iterative design loop
        $M_{act\ OLD\ i} = M_{act\ i}$
        $M_{ant\ OLD\ i} = M_{ant\ i}$
        $M_{hinge\ OLD\ i} = M_{hinge\ i}$ ▷ Aging specifications
        ▷ Actuator sizing
        $M_{act\ i} = M_{aero\ i} + M_{skin\ i} + M_{hinge\ OLD\ i} + M_{ant\ OLD\ i}$
        Compute $F_{act\ i}$ from *actuator sizing*($M_{act\ i}, \theta_i$, Sizing rules)
        ▷ Antagonist actuator sizing
        $M_{ant\ i} = M_{act\ i} + M_{skin\ i} + M_{hinge\ OLD\ i}$
        Compute $F_{ant\ i}$ form *actuator sizing*($M_{ant\ i}, \theta_i$, Sizing rules)
        ▷ Hinge sizing
        $F_{hinge\ i} = F_{act\ i} + F_{aero\ i} + F_{skin\ i} + F_{ant\ i}$
        Get $M_{hinge\ i}$ from *hinge selection*($F_{hinge\ i}, \theta_i$, Sizing rules)
    while $(|\frac{M_{hinge\ i} - M_{hinge\ OLD\ i}}{\frac{1}{2}\cdot(M_{hinge\ i} + M_{hinge\ OLD\ i})}| > 5\%$ and $|\frac{F_{ant\ i} - F_{ant\ OLD\ i}}{\frac{1}{2}\cdot(F_{ant\ i} + F_{ant\ OLD\ i})}| > 5\%)$ or number of iterations below maximum
    ▷ Sizing design end
    Compute costs and penalties
    return costs

4.6 Optimization results

Based on the modeled concept, actuators, skin and optimization problem, several tests have been performed. Different cost parameterizations and different hinge and skin technologies have been assessed. The cost function evaluation – i.e. computation of a completely sized flap with specified shape, actuators, antagonist actuators and skin – takes about 0.6 s on a laptop with 8 core CPU at 2.3 GHz. Different genetic algorithm parameters are tried. Finally, a population of $N = 150$ individuals (initially randomly generated) with a cross over fraction of 0.9, computed in parallel using migration has been selected. Each optimization lasts about 10 min and is processed many times with small variations in cost weightings to ensure the suitability of the results.

The optimization is used first to determine the best technologies. Then the locus of the hinge locations is determined for a multi-objective optimization using Pareto fronts.

4.6.1 Technological impacts on objectives

This section compares the results from two technological choices: elastic skins with elastic beam hinges and feathered skins with gliding hinges.

4.6.1.1 Flap with elastic skin with elastic beam hinges

The considered flap uses the elastic skins modeled in Section 4.4.1, with beams between the articulated ribs. These beams are bend when the ribs rotate. An algorithm calculates the dimensions of these flexible beams made of titanium, but is not detailed for brevity purpose.

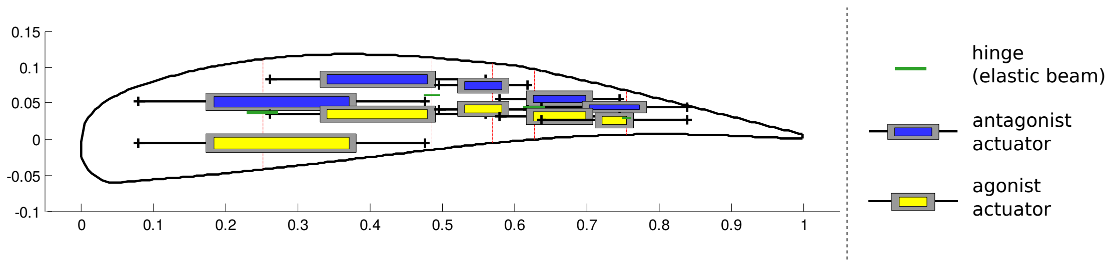

Figure 4.14: Sketch of the flap profile with the actuators and the flexible articulations. The sizes of the actuators represent the amount of SMA, assuming a square section. Actuators are drawn horizontal with maximum length between anchors, but this can be adapted in a final design step.

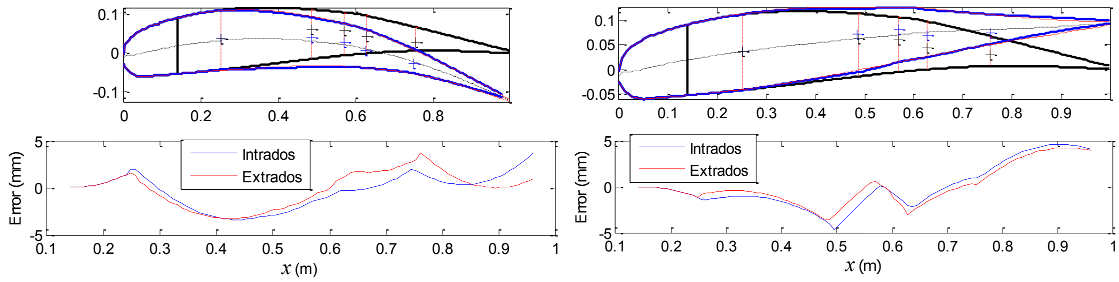

Figure 4.15: Optimized shape for both down and up morphing, with the corresponding approximation errors, as explained in 4.2.3.1.

Figure 4.14 schematically presents the flap with the actuators and the flexible beam articulations. The shape approximation performance is presented in Figure 4.15. The result of the optimization is detailed in Appendix B.1. For the 0.5 m span flap section, the total mass is estimated to 4.9 kg and a maximum heating power of 8 kW. The internal forces are quite large, for example, the first agonist actuator is designed to apply a force equivalent to 4.3 tons. This high force in the actuator is not only due to the aerodynamic forces, as visible in table 4.2. More than half the actuator specified torque is dedicated to counter act the skin elasticity. The part required by the hinge elasticity is below 5 %. This indicates that the actuators can be downsized by a factor 2 if the skin is removed.

Another important result regarding the technological choice is design of the flexible beams. The forces and available spaces (mostly in span direction) restrict the design of the flexible hinges to bad aspect ratios. The beams are not slim, which may conduct to unexpected behaviors. This is detected in the sizing algorithm that generates penalties. This result finally indicates that despite their relatively low parasite torque due to elasticity, the flexible beams are not suitable for the proposed morphing flap.

Table 4.2: Design moments for the actuators at hinge locations (without the torques from agonist and antagonist actuators)

	Design moment	Aero part	Skin elastic part	Hinge parasite part
Hinge #1	845.3 Nm	48.4%	49.2%	2.4%
Hinge #2	317.4 Nm	50.4%	47.4%	2.2%
Hinge #3	178.2 Nm	59.0%	40.7%	0.3%
Hinge #4	206.3 Nm	34.1%	61.2%	4.4%
Hinge #5	91.9 Nm	29.1%	78.6%	2.3%

4.6.1.2 Flap with feathered skin and gliding hinges

The considered flap uses the skin and feather concept modeled in Section 4.4.2. Instead of flexible beams, the articulations are realized using gliding bearings. These two selected technologies introduce friction but are not elasticity.

Figure 4.16 schematically presents the flap with the actuators and the gliding hinges. The shape approximation performance is presented in Figure 4.17. The result of the optimization is detailed in Appendix B.2. For the 0.5 m span flap section, the total mass is estimated to 2.6 kg and a maximum heating power of 2 kW. The internal forces are lower than the solution with elastic skins. For example, the first agonist actuator is designed to apply a force equivalent to 2.0 tons. This force in the actuator is mainly due to the aerodynamic forces, as visible in table 4.3. The part required by the friction from hinges and feathers is below 1.3 %.

The proposed solution with gliding bearings and feathers is efficient because parasitic forces are very low. Then the actuators are designed to only actuated against the aerodynamic forces and the antagonist actuators. The gliding bearings are selected as the best articulation technology, as their little dimensions, their very low parasite torques and their integration easiness are better than the other technologies. The feathers demonstrate here their suitability regarding a low power consumption morphing flap; thus this technology is selected.

4.6.2 Multi-objective optimum

Previous optimization results provides interesting results but are highly depends on cost weightings. These weightings are empirically tailored and the impacts from the skin accuracy or the actuator integration are not distinguished. To discriminate

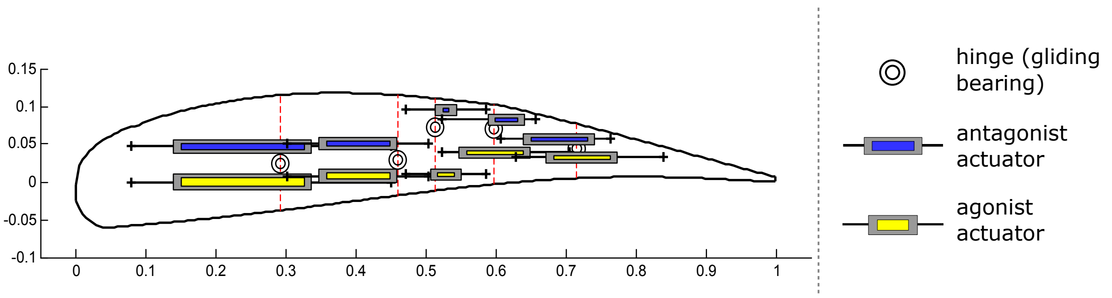

Figure 4.16: Sketch of the flap profile with the actuators and the gliding bearings. The sizes of the actuators represent the amount of SMA, assuming a square section. Actuators are drawn horizontal with maximum length between anchors, but this can be adapted in a final design step.

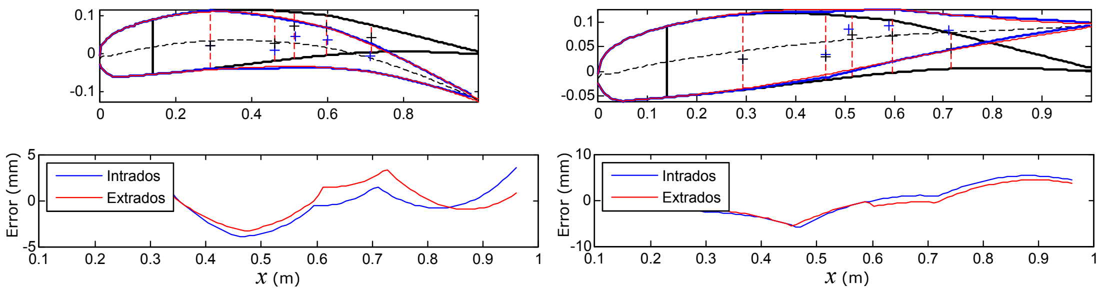

Figure 4.17: Optimized shape for both down and up morphing, with the corresponding approximation errors, as explained in 4.2.3.1.

Table 4.3: Design moments for the actuators at hinge locations (without the torques from agonist and antagonist actuators)

	Design moment	Aero part	Feather friction part	Hinge parasite part
Hinge #1	368.1Nm	98.7%	0.0% (0.07Nm)	1.3% (4.7Nm)
Hinge #2	184.5Nm	99.7%	0.0% (0.02Nm)	0.3% (0.6Nm)
Hinge #3	142.3Nm	100.0%	0.0% (0.01Nm)	0.0% (0.0Nm)
Hinge #4	90.2Nm	99.8%	0.0% (0.02Nm)	0.2% (0.2Nm)
Hinge #5	39.6Nm	98.6%	0.4% (0.16Nm)	1.0% (0.4Nm)

the impact of the different costs, a multi-objective approach based on Pareto front is used in the following.

Considering a population of N flaps, named $X_i, i \in [\![1, N]\!]$.The costs $C_{sha}(X_i)$ (respectively $C_{int}(X_i)$) is related to the shape (respectively is related to the integration of actuators). The flap X_j is Pareto optimal if there is no flap with one better cost, i.e. $\forall i \in [\![1, N]\!], C_{sha}(X_i) > C_{sha}(X_j)$ OR $C_{int}(X_i) > C_{int}(X_j)$.

The cost definitions for this multi-objective optimization are written in Equation4.12. It is remembered that: $S_{maxUP}/S_{maxDOWN}$ are the maximum skin error between the reference and the effective deformed shape for UP and DOWN deformation; k is the hinge/actuator/antagonist actuator number of the considered flap, $M_{aero\ k}$ is the aerodynamic torque on the k^{th} hinge; $\theta_{max\ k}$ is the angle range of the k^{th} hinge, $h_{max\ k}$ and $L_{max\ k}$ are the maximum available lever arm and length of the considered agonist/antagonist actuator.

$$
\begin{aligned}
C_{sha}(X_i) &= S_{maxUP}(X_i) + S_{maxDOWN}(X_i) \\
C_{int}(X_i) &= \sum_k M_{aero\ k} \frac{\theta_{max\ k} \cdot h_{max\ k}}{L_{max\ k}}
\end{aligned}
\tag{4.12}
$$

To justify the integration cost, consider the k^{th} actuator is designed with the lowest force. To apply the required torque at lowest force, the lever arm must be maximum (h_{max_k}). Then the stroke of an actuator is $\theta_{max\ k} \cdot h_{max\ k}$. The actuator length is assumed maximum, the relation between the stroke, the length is $L_{max\ k} = \theta_{max\ k} \cdot h_{max\ k}/\epsilon_{SMA}$. Depending on the geometric parameters, the SMA strain ϵ_{SMA} can be expressed by $\epsilon_{SMA} = \frac{\theta_{max\ k} \cdot h_{max\ k}}{L_{max\ k}}$. The actuator is feasible if the SMA strain is low enough to ensure the expected fatigue life. So the minimization of cost $C_{int}(X_i)$ tends to minimize the forces in the structure, whilst maximizing the space for actuator integration.

Considering these two costs, a genetic algorithm has spread the population of the flap on the Pareto front presented in Figure 4.18. Two main areas of the Pareto front are identified: an area where the shape approximation costs are low ($<$ 8 mm) for a wide range of integration costs, and an area where the integration costs decreases with the increase of the shape costs. At the extremity of these two areas are the best shape approximation flap and the best actuator integration capability flap. These two designs are respectively drawn on the figure with red highlighted drawbacks. For the first one the integration is not performed for one actuator; respectively for the other one, the shape approximation is very bad in the highlighted area. This observation indicates that a optimized flap which has both the best shape approximation and the best actuator integration capability does not exist. A compromise must be done.

Corresponding to the Pareto front flaps, the locus of the hinge positions is represented on Figure 4.19. The locus of hinges #5 does not move, locus for hinges #1, #3 and #4 are quite continuous whereas the positions of hinges #2 are spread on two spots. The Figures 4.19b and 4.19c indicates that the best hinge positions corresponding to the best shape approximation or the best actuator integrability are not identical. A compromise must be done.

This compromise is selected where the previously described two main areas cross each other. This crossing area corresponds also as a compromise between the different hinge positions. The Pareto front of Figure 4.20 presents the two compromise flap designs. The costs here are normalized, so that the costs are between 0 and 1. Both designs present a good shape approximation and a good actuator integration ability. Considering the worst shape approximation flap – also the one with the best integrability – (bottom right part of the figure), an improvement of 55% of the shape approximation costs only 8% of the integrability costs. On the other corner, the best shape approximation flap – also the one with the worst integration capability – (top left part of the figure), an improvement of 70% of the integration costs a 30% decrease in shape approximation. Additionally the compromise flap with the best actuator integration capability presents actuators larger by 5%, thereby corresponding to a heavier design consuming more energy.

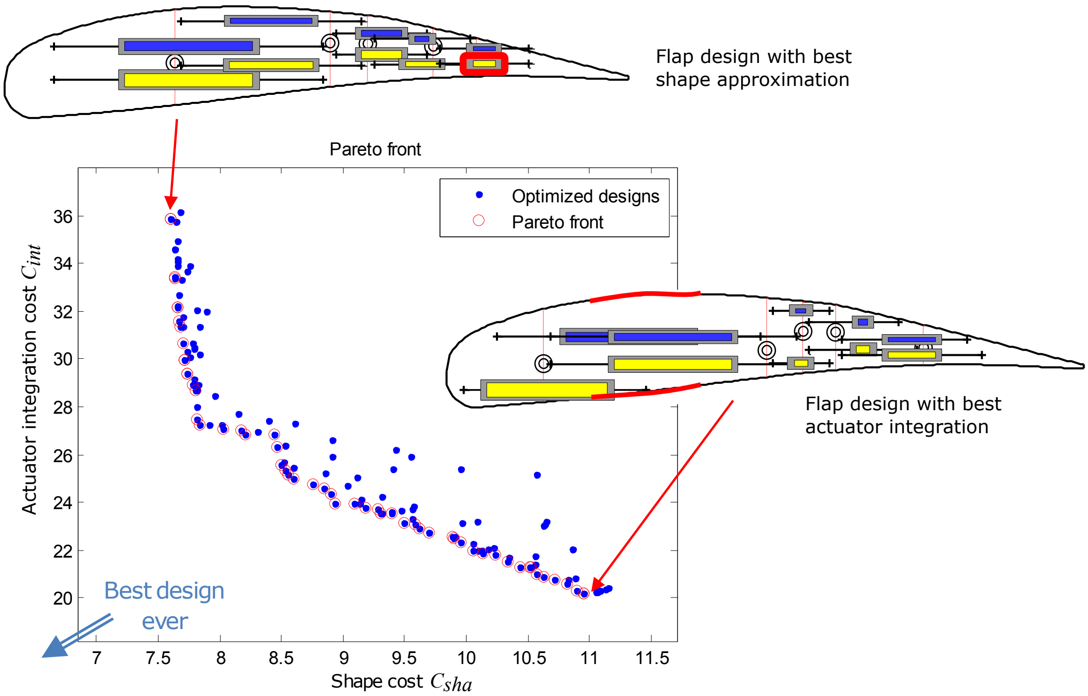

Figure 4.18: Pareto front Shape cost VS Integration cost. The population is represented by blue points and the Pareto optimal individuals are presented by red circles. The two extreme flaps are represented with red highlighted drawbacks: large integration issue for the last actuator or large error in shape approximation.

Finally, the choice of the ultimate flap design is the flap with the best shape approximation, to ensure a feasible flap. The articulation positions corresponding to the final choice are indicated on Figure 4.19.

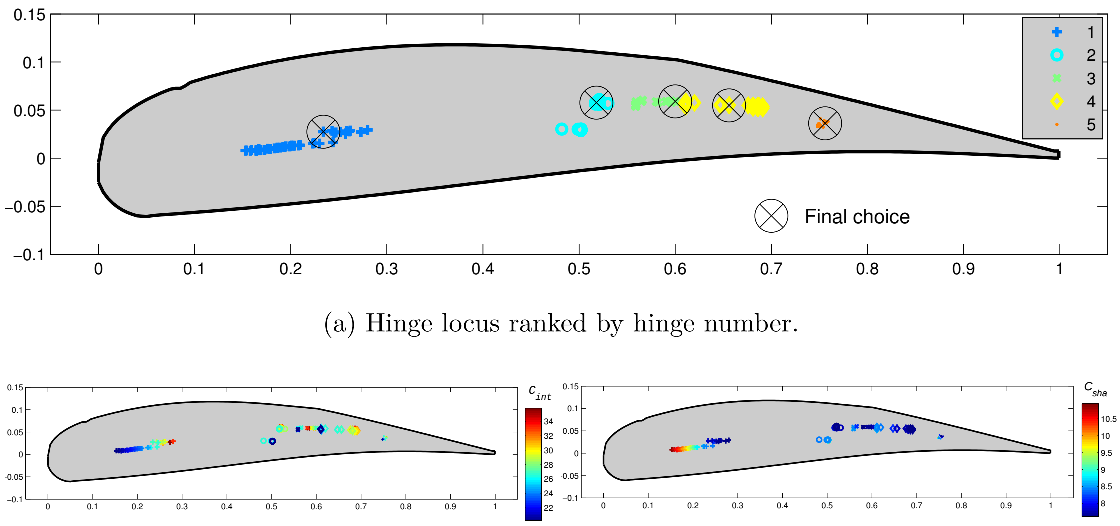

(a) Hinge locus ranked by hinge number.

(b) Hinge locus ranked by C_{int} cost.

(c) Hinge locus ranked by C_{sha} cost.

Figure 4.19: Hinge locus. The positions of the hinges of the Pareto front's flaps are plotted threefold: 4.19a color shades represent the hinge number, 4.19b color shades represent the actuator integration cost and 4.19c color shades represent the shape approximation cost.

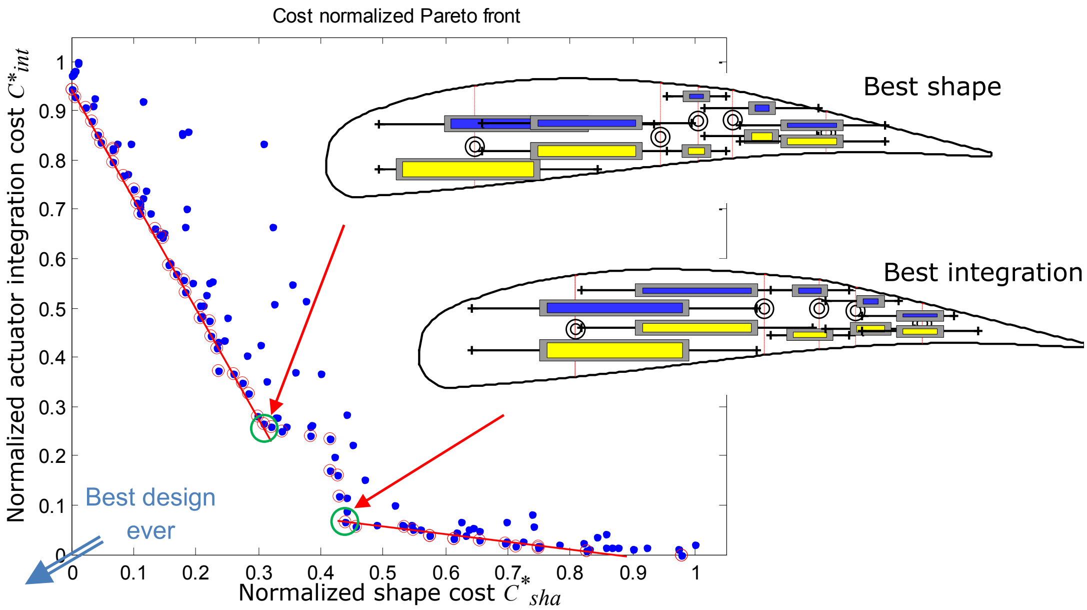

Figure 4.20: Normalized Pareto front Shape cost VS Integration cost. Here the costs have been affine transformed to be between 0 and 1. The population is represented by blue points and the Pareto optimal individuals are presented by red circles. The two possible compromise flaps are represented on the right.

4.6.3 Design choice

The justification of the selected design is presented in the previous Section 4.6.2. The hinge positions are presented in Figure 4.19. The design estimates a 9 kg flap section with an average consumption of 0.515 kW, as it is developed in B.3. One can notice that the expected fatigue life is limited to 40,000 cycles, which is very low. This estimation comes from the lever arm limitation in the thin rear part of the wing. This issue is alleviated during detailed design by inclining the actuators – a new calculation of the active lengths and lever arms is performed for such inclined actuators.

Additionally, all the actuators have been inclined to increase the lever arm and then to decrease the forces in the structure. Taking into account the available space in the span direction, the different actuators are spread in the span. It results a macro-actuator composed of the different actuators, the articulated ribs and the hinges. The flap is then made by the assembly of four macro-actuators plus spars, stiffeners, skin and feathers. The detailed design of the such optimized flap prototype is not detailed anymore in this chapter. Figure 4.21 presents a view of the manufacturing CAD model of the macro actuator.

4.7 Conclusion and outlooks

The present chapter deals with morphing wing design through optimization. The target is a true scale flap of a regional industrial aircraft. A camber control concept based on articulated ribs is proposed. This concept can be used with different hinge technologies and different skin technologies. The actuators, based on innovative smart materials like shape memory alloys, are also investigated. Comparing different actuation topologies, it has been shown that in terms of weight and internal forces, the agonist/antagonist topology is better than a solution with one actuator and a counter spring. Based on industrial specifications and constraints, genetic optimizations have been performed comparing the different technological choices. As a result, the elastic skin causes large issues according to the internal forces in the structures and is responsible for over-sizing by more than 50% the actuator forces. Then an innovative bio-inspired skin and feather concept has been selected, taking advantage of the specifications and constraints. As the optimization objectives are related to the weight, the shape approximation, the energy consumption and the fatigue life of actuators, a multi-objective optimization based on Pareto front is used to choose the ultimate flap design.

Finally, the resulting design is feasible and a detailed design has been done. Future works will focus on the design, integration, and control of the macro-actuators

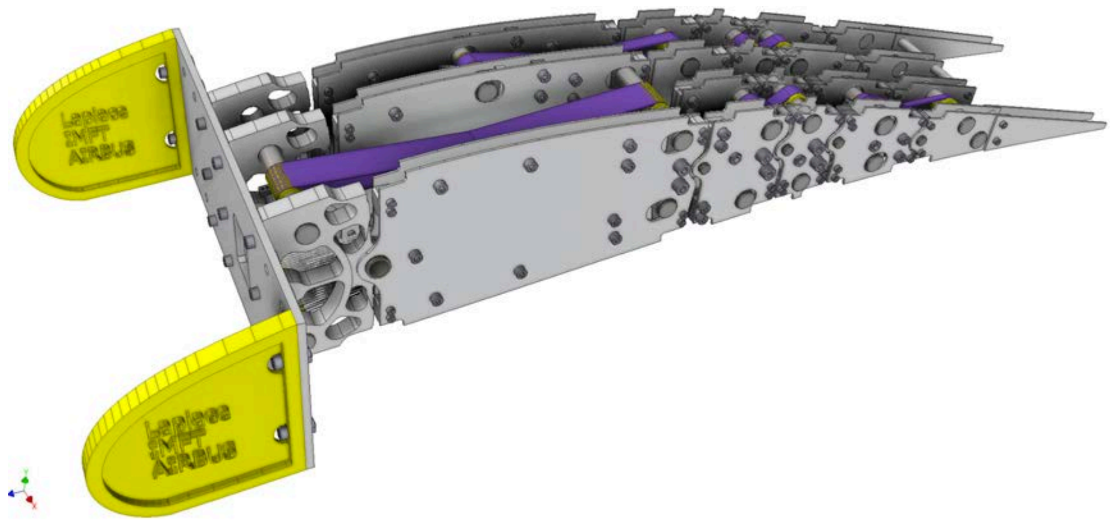

(a) 3D CAD view of the detailed design of the macro-actuator of the flap.

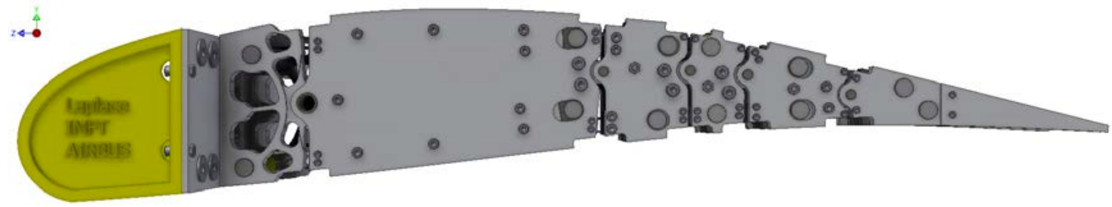

(b) Side view of the detailed design of the macro-actuator of the flap.

Figure 4.21: Detailed design views of the macro-actuator of the flap.

in a true scale flap prototype. Then electromechanical and aerodynamic characterizations will be performed on dedicated static test bench and in wind-tunnel.

Acknowledgements

The authors are grateful to Airbus and RTRA-STAE Foundation that provided funding for this research. The authors would also like to thank Dominique HARRIBEY, Oussama FILALI and Maxime RUFFEL for their useful advice and help within this work.

Conclusion

This thesis has investigated electroactive hybrid morphing, with a calling towards real scale application for Airbus A320.

Morphing wings have potential to increase aerodynamic performance but actuators, structures and aerodynamics have to be studied together. Within the framework of the LAPLACE and IMFT laboratories, the originality of the proposed approach is to combine different smart material actuators to both adapt the wing shape by large deformation and manipulate the airflow turbulence.

In this multidisciplinary study in cooperation with Airbus, a reduce model of an electroactive hybrid morphing wing has been made. Wind tunnel experiments have been performed. The morphing impacts on lift and drag is measured and wake dynamics with morphing mechanisms are described. To apply the developed concept on a true scale wing, a first step consisting in sizing and designing a A320 morphing flap is dealt with.

- In more details, the first part of the work consisted in making a 700 mm chord hybrid morphing wing. Models have been developed for design purpose and for control purpose. Validations were performed on previous mock-up (Scheller's NACA4412 model) or specifically made test bench (actuated plate). Models are in agreement with experiments but analytical models exhibit limits for complex structures. Plus, finite element analysis highlighted the sensibility to pre-strain applied to actuators, this informing the care to be given during making. Electrodynamic characterization has been performed: a notable result is the choice of controller settings can reduce the power consumption by 20%.

- The second contribution regards the experimental aerodynamic characterization. The wing prototype has been instrumented with pressure transducers and a home made balance. The sensors' accuracies and reliabilities have been characterized and the experiments have been programmed to be automatically processed in order to maximize the reliability and the independence of the different morphing configuration. For the first time, the force changes due to camber control, trailing edge vibration and their combination have been acquired in a large database. Lift enhancement by 27% (23% due to camber + 4% due to small trailing edge vibrations) has been measured. The measured decrease of 13% in drag at Reynolds number of 10^6 has been seen only once. The measurement set up has been update to perform accurate measures at lower velocities at initial cambers, where the reproducibility is observed with gains of 2% at optimal frequency. High speed time resolved particle image velocimetry (HS TR-PIV) measurements have been performed in the trailing edge wake region. The flow dynamics has been studied by means of time average fields, spectra and Proper Orthogonal Decomposition. Vortices have been identified and a theory based on models from Hunt is used to explain eddy blocking effect and vortex breakdown. A morphing induced reduction of 99.9% of coherent vortices power density has been observed.

- The optimal design of a true scale morphing flap is the third contribution of the manuscript. From Airbus data and specifications, the transition towards true scale actuators for camber control is investigated. The technology gap implies that the developed solutions for a reduced scale are not applicable. Based on a simple parametrized articulated structure, analytic models for shape evaluation, force balance, actuators, skin technologies and hinges are developed. These models are parts of the sizing algorithm, codded to optimize the flap design according to shape approximation error, weight, power consumption and life span. It is showed that agonist-antagonist actuator is better than a single one way actuator with a counter spring. Also skin has to be pre-stressed to carry the aerodynamic loads with limited airfoil profile deformation. This leads to very high internal forces that over size the structure and the actuators. Consequently, an innovative solution bio-inspired with feathers and internal skin appears to be a good alternative. A multi-objective optimization based on Pareto front helped to choose the final choice: a 10 kg and 1 m length macro actuator carry 250 kg of aerodynamic force while deforming the trailing edge by 20 cm with a maximum average power consumption of 0.5 kW. The result is now the basis for designing a true scale demonstrator but the analytic model with static assumption is limited; the dynamic fluid-structure behavior has to be addressed.

The works presented in this manuscript is part of the basis of the European project *Smart Morphing and Sensing*[6]. This project is coordinated by Marianna BRAZA. It started in May 2017 and will end in April 2020. It will include part of activities developed in the reduced scale prototype (Chapter 2) with further testing of close-loop control as well as innovative electromagnetic actuators. The large scale prototype of this project will result from the continuation of the designed morphing flap presented in Chapter 4.

[6]smartwing.org/SMS

Outlooks

This work answered some questions and some elements have to be continued or enhanced. Two main points are discussed here:

- The understanding of the physics phenomena due to hybrid morphing are not well understood yet. Better force measurements are needed and a new update of the sensors can be proposed. This is already difficult because the measurement specifications are very demanding. Eventually, a new wing prototype, lighter with upgraded actuators could be designed for this purpose. Regarding the PIV measurements, the actuations selected in the manuscript correspond to points with small effects. New measures – of the wake and of the flow over the trailing edge – at vibrations leading to significant changes in lift have already been investigated and are know being post-processed; an example is provided in Figure 3.14. The SMS project could answer the questions raised by the present thesis. Notably, a closed loop controller of the turbulence is investigated. Innovative optical pressure sensors are used to sense the turbulence in order to control the morphing actuators.

- The wing demonstrator at true scale is not done yet. The technologies are selected, the camber control actuator is sized. The design is in progress and a validation test of the macro-actuator is planed soon. Also, a further investigation of the design by optimization can be addressed. Convergence criteria or cost definition can be improved; deterministic optimization algorithms may be used instead of genetic algorithm. It will take place in the already made fixed leading edge visible on Figure 4.22 Dynamics study of the fluid-structure-actuator interaction is currently being assessed. Then, the mechanical structure has to be designed before the final making.

- All of the work related in the Chapter 4 is dedicated to camber control only; the vibrating trailing edge has to be designed too. Due to the increased velocities, forces and amplitudes for the subsonic and transonic flights, the technology transfer can not be a homothety of the small scale vibrating actuator. Magnetic actuators – with conventional electro-mechanical devices or innovative magnetic shape memory alloys for instance – will be investigated in the framework of the SMS project.

- Bio-inspiration can go further. The manta ray uses traveling waves on its fins to efficiently propel itself. This is done with a smart interaction with generated vortices. This idea can be transposed to the trailing vibrations, to generate spanwise traveling waves. These transverse mechanical waves interact with the 3D secondary vortices, with potential drag and noise reductions.

The following section presents a list of my contributions: publications, co-supervising, scientific popularization.

Related publications and contributions

Within the current framework of PIV measurements, experiments discussed in Chapter 3 were used to evaluate and buy new cameras and lasers by Sébastien Cazin and Moïse Marchal from the technical support of IMFT. These experiments were processed on the MPI cluster EOS of Calmip team, using the software CPIV developed by Pierre Elyakim. Also, the presented work has been participating to the Smart Wing platform[7]. The electroactive hybrid morphing wing prototype realized for the purpose of this thesis will be used for further investigations in the context of the SMS European project.

Scientific popularization:

- "Aéronautique : des chercheurs toulousains travaillent sur la mise au point des ailes du futur", a video report in 4 episodes on regional TV (France 3), 2014 [8]
- "Royal Society Summer Science Exhibition", "Smart Wing Design through turbulence control: Science imitating nature", London, United Kingdom, July 2014. [9]
- "Fête de la science", visit of the LAPLACE laboratory, Toulouse, France, October 2015.
- "The Wings of the Future" , video report by CNRS, 2015 [10]
- `"Ma Thèse en 180 secondes (MT180)", French national competition, selected for regional final, 2016 [11]

[7] http://smartwing.org/

[8] http://france3-regions.francetvinfo.fr/occitanie/haute-garonne/toulouse/aeronautique-des-chercheurs-toulousains-travaillent-sur-la-mise-au-point-des-ailes-du-futur-544498.html

[9] http://sse.royalsociety.org/2014

[10] https://news.cnrs.fr/videos/the-wings-of-the-future

[11] http://www.dailymotion.com/video/x4cdfb4

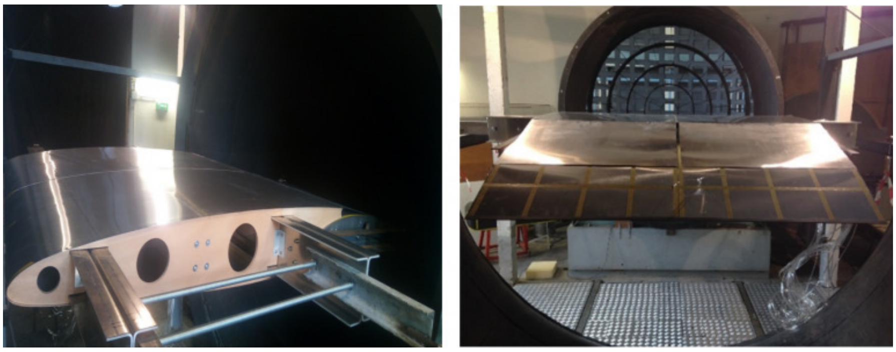

(a)

Figure 4.22: (a) Pictures of the Large Scale prototype in the S1 wind tunnel of IMFT laboratory. This prototype is part of the SMS project. This project has received funding from the European Union's H2020 program for research, technological development and demonstration under grant agreement no 723402.

- "Le biomimétisme : la nouvelle innovation qui s'inspire de la nature", 5min video report on the most watched national TV news (France 2), 2016 [12]

- "Fête de la science, bio-inspiration & aérodynamique", at Aeroscopia museum, Toulouse, France, October 2016. [13]

Supervised and co-supervised trainees:

- Dimirti Behary-Laul-Sirder, *Conception et réalisation d'un convertisseur statique multi voies sinus haute tension pour charge capacitive*, 2^{nd} year internship, ENSEEIHT engineering school (M1), 2015.

- Maxime Ruffel, *Conception d'un banc d'essai statique pour aile déformable*, 4^{th} year internship, INSA Toulouse engineering school (M1), 2016.

[12] http://www.francetvinfo.fr/decouverte/le-biomimetisme-la-nouvelle-innovation-qui-s-inspire-de-la-nature_1512499.html

[13] http://www.musee-aeroscopia.fr/fr/actualites/fete-de-la-science-au-mus%C3%A9e-les-8-9-octobre

- Oussama Filali, *Évaluation, comparaison et caractérisation de systèmes d'actionnement destinés au morphing de surfaces portantes de grandes envergures*, final year project of ENIT engineering school (M2), 2016.

- Vanilla Temtching Temou, *Simulation numérique en aéroélasticité des interactions fluide-structure et participation à la conception de la maquette d'une aile de type Airbus A320 en morphing électroactif hybride dans une échelle proche de 1*, final year project of SUPAERO engineering school (M2), 2016.

- Yannick Bmegaptche Tekap, *Conception d'un prototype d'une aile d'Airbus A320 d'échelle proche de 1 avec volet en morphing électroactif hybride*, final project of M2 research in mechanical engineering specialized in structures and materials, 2016.

- Mateus Carvalho, *Contribution á l'étude du morphing d'une aile d'avion de type Airbus A320 en échelle intermédiaire et échelle 1*, final year project of INSA engineering school (M2), 2017

- Martin Laroche, *Mise en oeuvre expèrimentale de dispositifs de caractérisation d'alliages á mémoire de formes thermiques et magnétiques*, 2^{nd} year internship, ENSEEIHT engineering school (M1), 2017.

Award and distinction:

- Best presentation award at the GEET day, annual meeting of the doctoral school, 2017.

- Best paper award – student travel grant award; for the paper: G. Jodin, J. Scheller, J.F. Rouchon, M. Braza. "On the multidisciplinary control and sensing of a smart hybrid morphing wing, *2017 IEEE International Workshop ofElectronics, Control, Measurement, Signals and their Application to Mechatronics (ECMSM)*, `https://doi.org/10.1109/ECMSM.2017.7945866`

Related publications

Peer-review publications:

1. J. Scheller, G. Jodin, K. J. Rizzo, E. Duhayon, J. F. Rouchon, M. Triantafyllou, M. Braza. "A Combined Smart-Materials Approach for Next-Generation Airfoils", *Solid State Phenomena*, Volume 251 Pages 106-112, 2016, `doi.org/10.4028/www.scientific.net/SSP.251.106`

2. G. Jodin, J. Scheller, E. Duhayon, J. F. Rouchon, M. Triantafyllou, M. Braza. “An Experimental Platform for Surface Embedded SMAs in Morphing Applications”, *Solid State Phenomena*, Volume 260, pages 69-76, 2017, `doi.org/10.4028/www.scientific.net/SSP.260.69`

3. G. Jodin, J. Scheller, E. Duhayon, J. F. Rouchon, M. Braza. “Implementation of a Hybrid Electro-Active Actuated Morphing Wing in Wind Tunnel”, *Solid State Phenomena*, Volume 260, pages 85-91, 2017, `doi.org/10.4028/www.scientific.net/SSP.260.85`

4. G. Jodin, V. Motta, J. Scheller, E. Duhayon, C. Döll, J.F. Rouchon, M. Braza. “Dynamics of a hybrid morphing wing with active open loop vibrating trailing edge by Time-Resolved PIV and force measures”, Journal of Fluid and Structures, 2017, `doi.org/10.1016/j.jfluidstructs.2017.06.015`

International conferences:

1. G. Jodin, J. Scheller, J.F. Rouchon, M. Braza. “On the multidisciplinary control and sensing of a smart hybrid morphing wing, *2017 IEEE International Workshop ofElectronics, Control, Measurement, Signals and their Application to Mechatronics (ECMSM)*, `https://doi.org/10.1109/ECMSM.2017.7945866`

2. G. Jodin, N. Simiriotis, V. Temtching, D. Szubert, Y. Hoarau, J. Scheller, J.F. Rouchon, M. Braza. “Electroactive morphing of a supercritical wing for increasing the aerodynamic performance”, *52nd 3AF International Conference on Applied Aerodynamics* , International Conference on Applied Aerodynamics, 27 – 29 March 2017, Lyon – France

3. G. Jodin, J. Scheller, K.J. Rizzo, E. Duhayon, J.F. Rouchon, M. Braza. “On the hybridization of electro-active materials to enhance aircraft aerodynamic performance”, *More Electric Aircraft MEA2017*, 1 – 2 February 2017, Bordeaux – France

4. G. Jodin, J. Scheller, J.F. Rouchon, M. Braza. “Experimental investigation of the dynamics of a hybrid morphing wing: time resolved particle image velocimetry and force measures”, *APS DFD 2016 - The 69textrmth Annual Meeting of The American Physical Society – Division of Fluid Dynamics*, November 2016, Portland, Oregon, USA

5. G. Jodin, J. Scheller, E. Duhayon, J.F. Rouchon, M. Braza. “Implementation of a hybrid electro-active actuated morphing wing in wind tunnel”, *MSM 2016 - 12textrmth International Conference Mechatronic Systems and Materials*, July 2016, Bialystok, Poland

6. G. Jodin, J. Scheller, E. Duhayon, J.F. Rouchon, M. Triantafyllou, M. Braza. “An experimental platform for surface embedded SMAs in morphing applications”, *MSM 2016 - 12textrmth International Conference Mechatronic Systems and Materials*, July 2016, Bialystok, Poland
7. J. Scheller, K.J. Rizzo, G. Jodin, S. Cazin, M. Marchal, E. Duhayon, J.F. Rouchon, M. Braza. “PIV measurements of a high-frequency vibrating trailing edge morphing NACA4412 airfoil”, *NIM 2015 - Workshop on Non-intrusive Measurements for unsteady flow and aerodynamics*, October 2015, Poitier, France
8. K.J. Rizzo, J. Scheller, G. Jodin, E. Duhayon, J.F. Rouchon, M. Braza. “Écoulement en bord de fuite d’un profil NACA 4412 morphé par un actionnement hybride”, *CFM 2015 - 22ème Congrès Français de Mécanique*, August 2015, Lyon, France
9. J. Scheller, K.J. Rizzo, G. Jodin, E. Duhayon, J.F. Rouchon, M. Braza. “A hybrid morphing NACA4412 airfoil concept”, *ICIT 2015 - 2015 IEEE International Conference on Industrial Technology*, March 2015, Sevilla, Spain
10. J. Scheller, K.J. Rizzo, G. Jodin, E. Duhayon, J.F. Rouchon, G. Harran, M. Braza. “Time-resolved PIV measurements of a hybrid morphing NACA4412 airfoil”, *IFASD - International Forum on Aeroelasticity and Structural Dynamics*, July 2015, Saint Petersburg, Russia
11. J. Scheller, K.J. Rizzo, G. Jodin, E. Duhayon, J.F. Rouchon, M. Braza. “A Combined Smart-Materials Approach for Next-Generation Airfoils”, *MSM 2015 - 11th International Conference Mechatronic Systems and Materials*, July 2015, Kaunas, Lithuania
12. G. Jodin, Johannes Scheller, Karl Joseph Rizzo, Eric Duhayon, Jean-François Rouchon, Marianna Braza. “Dimensionnement d’une maquette pour l’investigation du morphing électroactif hybride en soufflerie subsonique”, *CFM 2015 - 22textrmme Congrès Français de Mécanique*, August 2015, Lyon, France
13. G. Jodin, J. Scheller, K. J. Rizzo, E. Duhayon, J. F. Rouchon, M. Braza. “Models for dimensioning hybrid morphing airfoil actuating system”, *MEA 2015 More Electric Aircraft , International conference*, February 2015, Toulouse, France

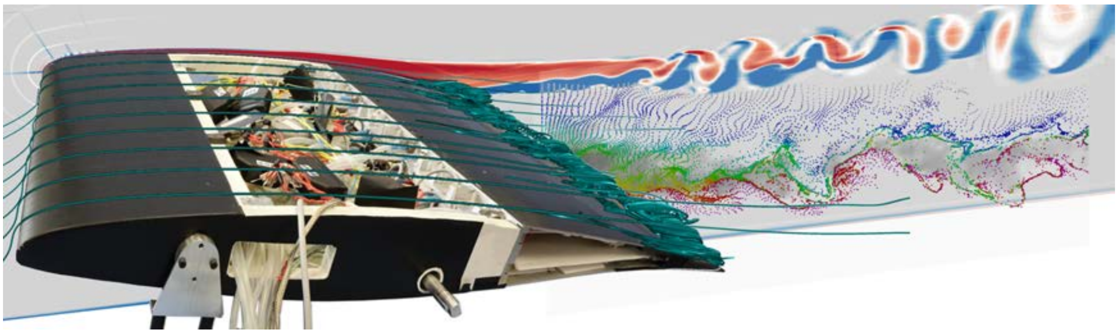

Figure 4.23: Artist view of electroactive morphing. Photomontage from a picture of the small wing prototype, streak-lines from PIV measures and numerical simulations made by IMFT. Image made for 3AF, 2017.

APPENDIX A

Wind tunnel experiment appendices

A.1 Experimental result validation: statistical convergence of the PIV

As the airflow is chaotic and characterized by coherent structures and random structures, statistic tools are used. Before making physical interpretation on statistical results, the statistical convergence is checked. To perform the convergence calculation, the same 8 points as 3.7 are selected. Points 1 to 4 are placed in the more energetic part of the wake. Points 5 and 6 are in the upper and middle part of the wake, behind the trailing edge. The points 7 and 8 are placed far downstream. For these points, the time averages depending on the experiment time is presented in figure below. The first order quantities (the mean stream-wise and crossflow velocities) converge quickly, then the second order (the Reynolds tensor components) reasonably converge at few per cent of the final value. For example Figure A.1 presents the convergence for baseline experiment. All quantities are within an interval of +/-2% before 8 s, so the experiment has reasonably converged. The convergence has been checked for all the morphing experiments. Therefore we can conclude that the 10 s experiments are statistically converged.

A.2 Experimental result validation: statistical convergence of the balance

For the same reasons as presented in A.1, convergence analysis of the balance measurements is performed. Figure A.2 presents the convergence of the average then the variance of lift and drag, for a selection of 80 different experiments at

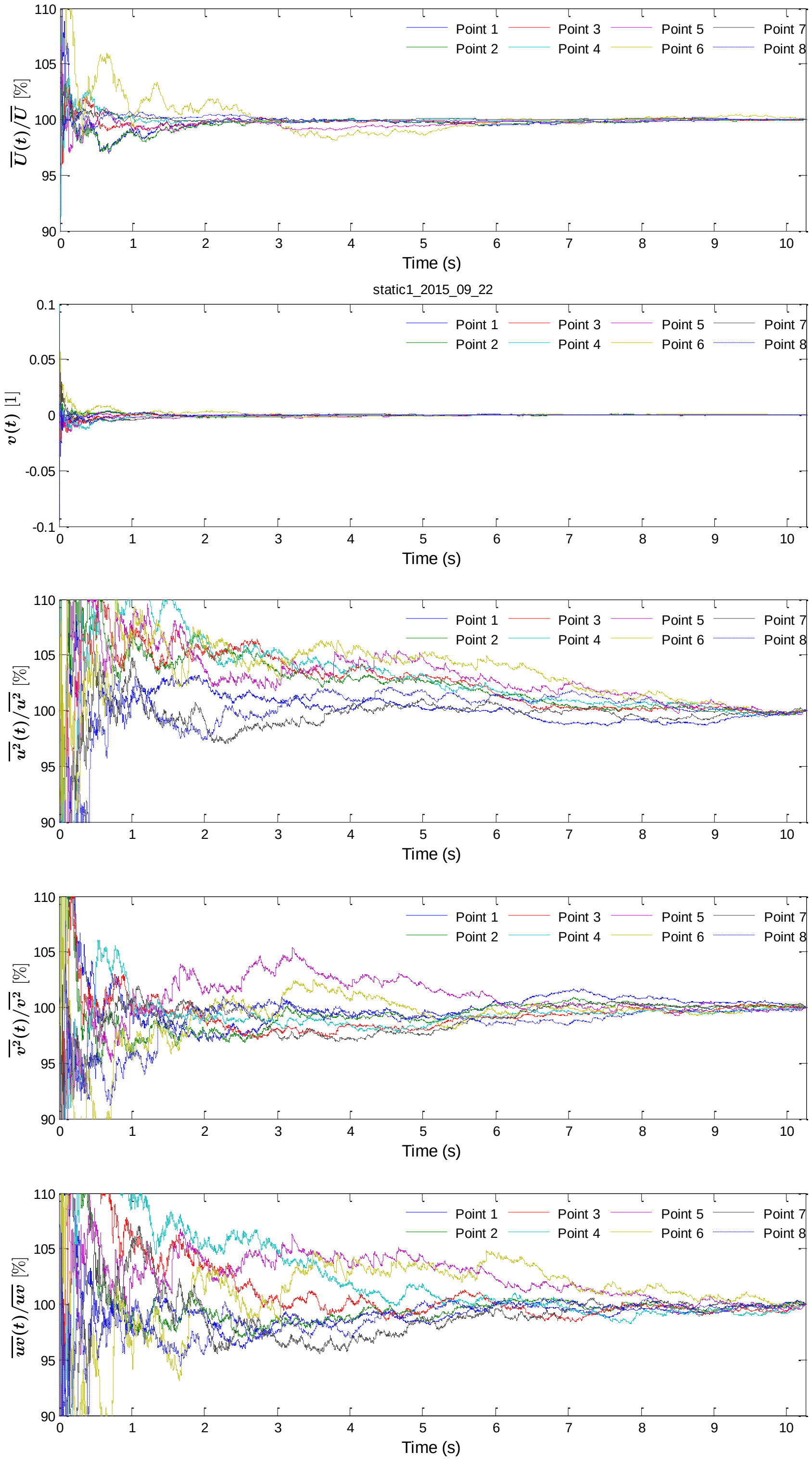

Figure A.1: Convergence of $\overline{U}$, $\overline{v}$, $\overline{u^2}$, $\overline{v^2}$ and $\overline{uv}$ quantities for the baseline configuration.

$Re = 10^6$. The average values are converged under 1% in less than 2 s; the variance values require more than 13 s. This ensure the right interpretation of the results, but not their accuracies. The accuracies and repeatability of the measured values are checked using calibrated weights hold on the balance's arms through pulleys and ropes.

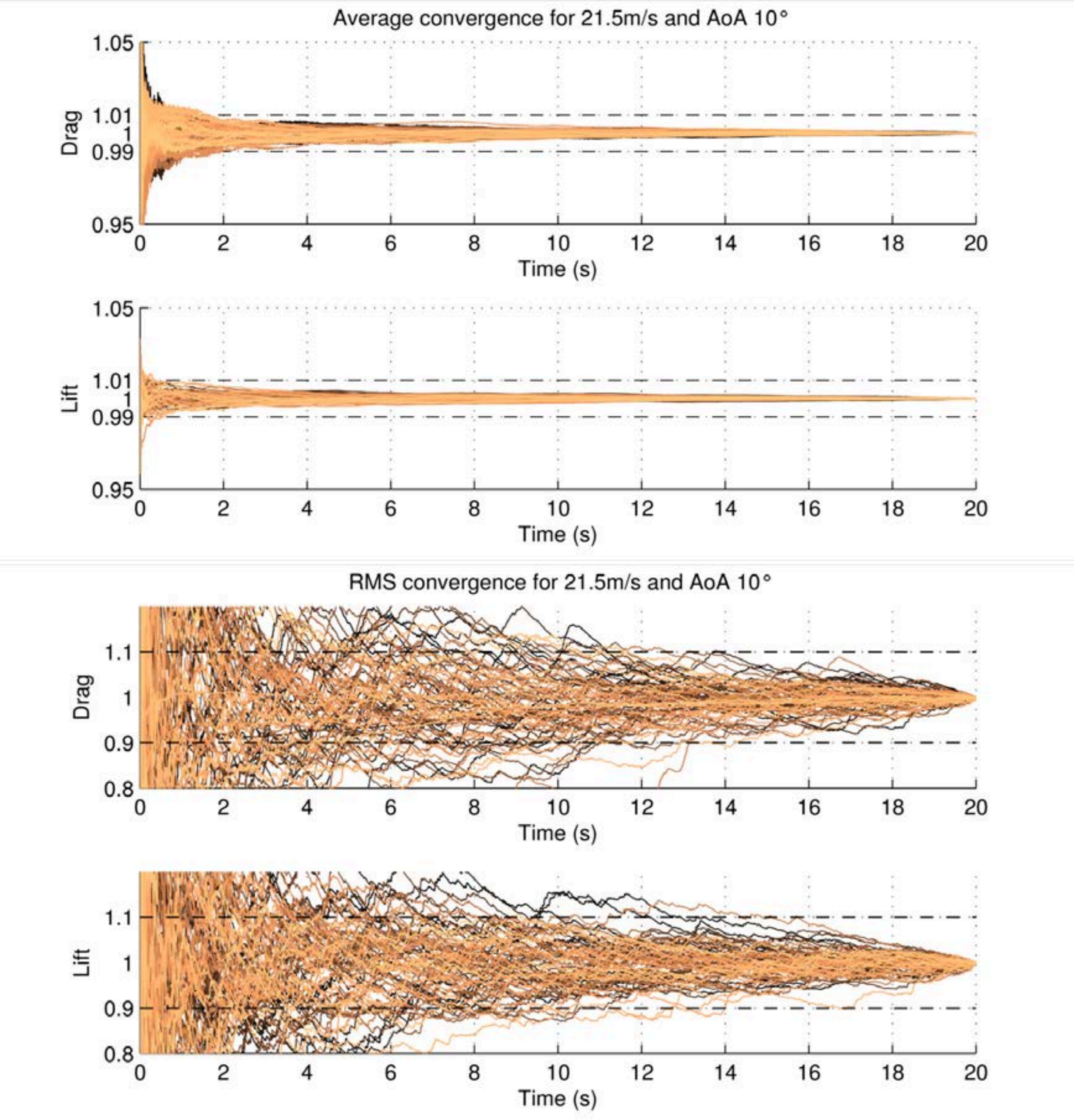

Figure A.2: Convergence of lift $(L/\overline{L})$ and drag $(D/\overline{D})$ for 80 actuation cases including baseline configuration.

A.3 Parasite drag effect

The aspect ratio and the wind tunnel's walls cause perturbation in the force measurements. Effects on lift and parasite drag have been studied and it is possible to estimate correction coefficients that are applied on the aerodynamic coefficients. An example about the corrected lift coefficient $C_{Lcorrected}$ follows: $C_{Lcorrected} = \alpha \cdot C_{Lmeasured}$, where α is a correction coefficient that depends on the dimensions of the wing model and wind tunnel, as well as flow conditions (i.e. free stream velocity). In the present study, we focus on the comparison of the actuated cases to the static baseline case. As flow conditions and geometries do not change during morphing, the value of α remains constant. Hence the calculation of the relative morphing effect ΔC_L does not depend on the correction coefficient: $\Delta C_{Lmeasured} = \frac{C_{Lmeasured}^{morphing} - C_{Lmeasured}^{baseline}}{C_{Lmeasured}^{baseline}} = \frac{\alpha \cdot C_{Lmeasured}^{morphing} - \alpha \cdot C_{Lmeasured}^{baseline}}{\alpha \cdot C_{Lmeasured}^{baseline}} = \frac{C_{Lcorrected}^{morphing} - C_{Lcorrected}^{baseline}}{C_{Lcorrected}^{baseline}} = \Delta C_{Lcorrected}$.

The correction factor α may depend on the $C_{Lmeasured}$ but the morphing effects on flow are non significant enough to cause a change in the correction factor. Thus the previous statement is valid. As a conclusion, the relative morphing effects calculated throughout the paper are valid regardless of the common wind tunnel compensation.

APPENDIX B

True scale cambered control flap appendices

B.1 Optimization results of the flap with elastic skin and elastic beam hinges

Normalized costs:

mass: 0.97	energy: 0.40	cycle life: 8.04
shape: 1.66	penality: 11.23	Sum: 22.30

General parameters

Span = 0.500 m

SMA set: design to 2% strain and 150 MPa

Optimization results

Number of rib section:	#1	#2	#3	#4	#5
Hinge positions (x/C)	25.2%	48.6%	57.1%	62.9%	75.7%
Hinge height position	42.5%	57.4%	57.5%	45.5%	41.8%

Rotation angles:

Rib section:	#1	#2	#3	#4	#5
	+7.5°	+6.6°	-3.5°	+7.7°	+6.5°

Skin strain:

	Up bending	Down bending
Intrados skin:	-1.3%	1.8%
Extrados skin:	2.0%	-1.4%

Rib report

One rib mass: 1.722kg

Force report

Force repartition

	Design moment	Aero part	Skin elastic part
Hinge #1	845.3 Nm	49.6%	50.4%
Hinge #2	317.4 Nm	51.5%	48.5%
Hinge #3	178.2 Nm	59.2%	40.8%
Hinge #4	206.3 Nm	36.0%	64.0%
Hinge #5	91.9 Nm	29.8%	70.2%

Actuators report

	mass	Force	Strain	Lever arm	Angle	Active Length	Stress
Act.#1	0.547 kg	4269 daN	2.0%	0.029 m	7.46°	0.188 m	150 MPa
Act.#2	0.253 kg	2546 daN	2.0%	0.024 m	6.56°	0.139 m	150 MPa
Act.#3	0.085 kg	1927 daN	2.0%	0.017 m	3.50°	0.051 m	150 MPa
Act.#4	0.152 kg	2625 daN	2.2%	0.012 m	7.73°	0.073 m	150 MPa
Act.#5	0.130 kg	2211 daN	2.0%	0.006 m	6.48°	0.033 m	150 MPa

Total actuator mass: 1.168 kg
Total SMA mass only: 0.881 kg
Antagonist actuators:

	mass	Force	Strain	Lever arm	Angle	Active Length	Stress
Act.#1	0.359 kg	2759 daN	2.0%	0.029 m	7.46°	0.188 m	150 MPa
Act.#2	0.260 kg	2617 daN	2.0%	0.024 m	6.56°	0.139 m	150 MPa
Act.#3	0.082 kg	1852 daN	2.0%	0.017 m	3.50°	0.051 m	150 MPa
Act.#4	0.105 kg	1797 daN	2.2%	0.012 m	7.73°	0.073 m	150 MPa
Act.#5	0.044 kg	628 daN	2.0%	0.012 m	6.48°	0.068 m	150 MPa

Total actuator mass: 0.850kg
Total SMA mass only: 0.668kg

Skin elongation requirements
Elongation due to rotations in mm

Number of rib section:	#1	#2	#3	#4	#5
Up skin:	9.7	5.9	2.8	7.1	4.2
Down skin:	10.3	8.7	4.0	6.0	2.6
Optimal skin free-length : (mm)					
Up skin:	97.1	82.5	72.0	98.1	82.6
Down skin:	111.2	94.5	82.5	112.3	94.5
Optimal skin force : (daN)					
Max up skin:	742.8	536.5	291.9	541.8	383.7
Max down skin:	744.3	681.7	358.4	460.7	270.6
Min up skin:	247.6	178.8	97.3	180.6	127.9
Min down skin:	216.3	156.2	85.0	157.8	111.7

Estimated average power consumption
Total maintaining power: 0.453 kW
Total heating power: 2.001 kW
Actuators energy distribution:

#1	#2	#3	#4	#5	antago	#1	#2	#3	#4	#5
26.4%	11.6%	3.2%	6.3%	2.4%		26.4%	11.6%	3.2%	6.3%	2.4%

Life span estimation
Minimum life cycle: 1e+05 cycles
Actuator estimated life:

#1	#2	#3	#4	#5	antago	#1	#2	#3	#4	#5
2E+05	2E+05	2E+05	1E+05	2E+05		2E+05	2E+05	2E+05	1E+05	2E+05

Hinge report

	mass	b	h	L	max resitivie torque	Radial force
Hinge.#1	0.53kg	499mm	4mm	44mm	20.4Nm	8021.6daN
Hinge.#2	0.20kg	497mm	3mm	24mm	7.2Nm	6024.3daN
Hinge.#3	0.02kg	449mm	1mm	4mm	0.5Nm	4235.6daN
Hinge.#4	0.28kg	498mm	3mm	31mm	9.5Nm	5122.2daN
Hinge.#5	0.07kg	481mm	2mm	13mm	2.2Nm	3333.8daN

Total hinge mass: 1.099kg

Mass distribution

Total	Actuator	Rib structure	Elastic hinges
4.839kg	2.018kg	1.722kg	1.099kg
100.0%	41.7%	35.6%	22.7%

Overall flap

Total mass: 19.356 kg

Total average power: 8.004 kW

B.2 Optimization results of the flap with feathers and gliding bearings

Normalized costs:

mass: 0.52	energy: 0.10	cycle life: 6.73
shape: 2.29	penality: 39.13	Sum: 48.77

General parameters

Span = 0.500 m

SMA set: design to 2% strain and 150 MPa

Optimization results

Number of rib section:	#1	#2	#3	#4	#5
Hinge positions (x/C)	29.3%	46.1%	51.4%	59.8%	71.7%
Hinge height position	40.0%	35.4%	68.9%	69.2%	55.0%

Rotation angles:

Rib section:	#1	#2	#3	#4	#5
Up bending:	+6.7°	-1.1°	+0.1°	+2.8°	+4.6°
Down bending: -1.9°	-5.9°	+0.5°	-0.2°	-3.5°	

Rib report

One rib mass: 1.804kg

Force report

Force repartition

	Design moment	Aero part	Feather friction part
Hinge #1	363.4Nm	100.0%	0.0% (0.07Nm)
Hinge #2	183.9Nm	100.0%	0.0% (0.02Nm)
Hinge #3	142.3Nm	100.0%	0.0% (0.01Nm)
Hinge #4	90.0Nm	100.0%	0.0% (0.02Nm)
Hinge #5	39.2Nm	99.6%	0.4% (0.16Nm)

Actuators report

	mass	Force	Strain	Lever arm	Angle	Active Length	Stress
Act.#1	0.246kg	1989daN	2.0%	0.024m	8.52°	0.176m	150MPa
Act.#2	0.078kg	1093daN	2.0%	0.022m	4.82°	0.091m	150MPa
Act.#3	0.012kg	289daN	2.0%	0.063m	0.46°	0.025m	150MPa
Act.#4	0.026kg	371daN	2.0%	0.031m	2.99°	0.081m	150MPa
Act.#5	0.029kg	422daN	2.1%	0.012m	8.02°	0.081m	150MPa

Total actuator mass: 0.391 kg
Total SMA mass only: 0.301 kg
Antagonist actuators:

	mass	Force	Strain	Lever arm	Angle	Active Length	Stress
Act.#1 0.119kg	928daN	2.0%	0.024m	8.52°	0.176m	150MPa	
Act.#2 0.038kg	510daN	2.0%	0.022m	4.82°	0.091m	150MPa	
Act.#3 0.014kg	370daN	2.0%	0.023m	0.46°	0.009m	150MPa	
Act.#4 0.025kg	444daN	2.0%	0.012m	2.99°	0.032m	150MPa	
Act.#5 0.015kg	198daN	2.1%	0.012m	8.02°	0.081m	150MPa	

Total actuator mass: 0.211 kg
Total SMA mass only: 0.141 kg

Feathers length (mm):

Rib section:	#1	#2	#3	#4	#5
Extrados feathers	10.7	13.5	3.4	4.5	3.6
Intrados feathers	8.1	8.8	3.8	6.4	3.7

Feather deformation (mm):

Rib section:	#1	#2	#3	#4	#5
Extrados feathers	1.252	0.032	0.000	0.079	0.205
Intrados feathers	0.065	0.506	0.007	0.001	0.145

Estimated average power consumption

Total maintaining power: 0.129 kW
Total heating power: 0.571 kW
Actuators energy distribution:

#1	#2	#3	#4	#5	antago	#1	#2	#3	#4	#5
45.8%	13.0%	0.9%	3.9%	4.5%		21.4%	6.1%	0.4%	1.8%	2.1%

Life span estimation

Minimum life cycle: 1e+05 cycles
Actuator estimated life:

#1	#2	#3	#4	#5	antago	#1	#2	#3	#4	#5
2E+05	2E+05	2E+05	2E+05	1E+05		2E+05	2E+05	2E+05	2E+05	1E+05

Hinge report

	mass	b	h	L	max resitivie torque	Radial force
Hinge.#1	0.16kg	471mm	2mm	25mm	4.7Nm	2919.9daN
Hinge.#2	0.02kg	141mm	1mm	10mm	0.6Nm	1605.1daN
Hinge.#3	0.00kg	3mm	4mm	10mm	0.0Nm	662.5daN
Hinge.#4	0.00kg	25mm	2mm	10mm	0.2Nm	816.7daN
Hinge.#5	0.02kg	207mm	1mm	10mm	0.4Nm	621.2daN

Total hinge mass: 0.200kg

Mass distribution

Total	Actuator	Rib structure	Elastic hinges
2.605kg	0.602kg	1.804kg	0.200kg
100.0%	23.1%	69.2%	7.7%

Overall flap
Total mass: 10.421 kg
Total average power: 0.518 kW

B.3 Optimization results of the final chosen flap design

Normalized costs:

mass: 0.48	energy: 0.10	cycle life: 22.80
shape: 1.76	penality: 47.24	Sum: 72.39

General parameters
Span = 0.500 m
SMA set: design to 2% strain and 150 MPa

Optimization results

Number of rib section:	#1	#2	#3	#4	#5
Hinge positions (x/C)	23.4%	51.8%	60.2%	65.7%	75.6%
Hinge height position	46.9%	57.0%	58.8%	60.4%	49.1%

Rotation angles:

Rib section:	#1	#2	#3	#4	#5
Up bending:	+4.8°	+1.5°	+1.5°	+2.2°	+3.4°
Down bending:	-2.5°	-5.3°	+0.1°	+0.4°	-4.1°

Rib report
Rib report One rib mass: 1.707kg

Force report
Force repartition

	Design moment	Aero part	Feather friction part
Hinge #1	445.4Nm	100.0%	0.0% (0.16Nm)
Hinge #2	132.5Nm	100.0%	0.0% (0.06Nm)
Hinge #3	87.4Nm	100.0%	0.0% (0.02Nm)
Hinge #4	61.1Nm	100.0%	0.0% (0.01Nm)
Hinge #5	27.6Nm	99.3%	0.7% (0.20Nm)

Actuators report

Agonist actuators:

	mass	Force	Strain	Lever arm	Angle	Active Length	Stress
Act.#1	0.265kg	1818daN	2.0%	0.031m	7.62°	0.209m	150MPa
Act.#2	0.071kg	571daN	2.0%	0.030m	6.33°	0.164m	150MPa
Act.#3	0.019kg	444daN	2.0%	0.025m	2.03°	0.044m	150MPa
Act.#4	0.014kg	291daN	2.0%	0.027m	1.17°	0.027m	150MPa
Act.#5	0.015kg	297daN	3.1%	0.012m	7.56°	0.051m	150MPa

Total actuator mass: 0.383 kg

Total SMA mass only: 0.300 kg

Antagonist actuators:

	mass	Force	Strain	Lever arm	Angle	Active Length	Stress
Act.#1	0.129kg	849daN	2.0%	0.031m	7.62°	0.209m	150MPa
Act.#2	0.035kg	267daN	2.0%	0.030m	6.33°	0.164m	150MPa
Act.#3	0.009kg	207daN	2.0%	0.025m	2.03°	0.044m	150MPa
Act.#4	0.011kg	258daN	2.0%	0.014m	1.17°	0.014m	150MPa
Act.#5	0.007kg	140daN	3.1%	0.012m	7.56°	0.051m	150MPa

Total actuator mass: 0.192 kg

Total SMA mass only: 0.140 kg

Feathers length (mm):

Rib section:	#1	#2	#3	#4	#5
Extrados feathers	6.4	6.3	3.4	4.7	3.0
Intrados feathers	6.0	7.4	3.6	5.6	3.0

Feather deformation (mm):

Rib section:	#1	#2	#3	#4	#5
Extrados feathers	0.624	0.027	0.022	0.042	0.135
Intrados feathers	0.149	0.526	0.010	0.011	0.131

Estimated average power consumption

Total maintaining power: 0.129 kW

Total heating power: 0.568 kW

Actuators energy distribution:

#1	#2	#3	#4	#5	antago	#1	#2	#3	#4	#5
50.1%	12.4%	2.6%	1.0%	2.0%		23.4%	5.8%	1.2%	0.5%	0.9%

Life span estimation

Minimum life cycle: 4e+04 cycles

#1	#2	#3	#4	#5	antago	#1	#2	#3	#4	#5
2E+05	2E+05	2E+05	2E+05	4E+04		2E+05	2E+05	2E+05	2E+05	4E+04

Hinge report

	mass	b	h	L	max resitivie torque	Radial force
Hinge.#1	0.09kg	469mm	2mm	17mm	2.6Nm	2671.0daN
Hinge.#2	0.02kg	148mm	1mm	10mm	0.4Nm	841.0daN
Hinge.#3	0.00kg	10mm	3mm	10mm	0.1Nm	654.0daN
Hinge.#4	0.00kg	4mm	3mm	10mm	0.0Nm	550.9daN
Hinge.#5	0.01kg	124mm	1mm	10mm	0.3Nm	438.9daN

Total hinge mass: 0.120kg

Mass distribution

Total	Actuator	Rib structure	Elastic hinges
2.402kg	0.575kg	1.707kg	0.120kg
100.0%	23.9%	71.1%	5.0%

Overall flap

Total mass: 9.609 kg

Total average power: 0.515 kW

Bibliography

[88] *IEEE standard on piezoelectricity, ANSI IEEE 1987-176*. 1988. DOI: 10.1109/IEEESTD.1988.79638.

[Ald+16] M.A. Aldheeb et al. "A review on aerodynamics of non-flapping bird wings". In: *Journal of Aerospace Technology and Management* 8.1 (2016), pages 7–17.

[And10] J.D. Anderson Jr. *Fundamentals of aerodynamics*. Tata McGraw-Hill Education, 2010.

[Av49] I.H. Abbott and A.E. von Doenhoff. *Theory of Wing sections*. New York, NY: Dover Publication, Inc., 1949.

[Bal07] Rüdiger G Ballas. *Piezoelectric multilayer beam bending actuators: Static and dynamic behavior and aspects of sensor integration*. Springer Science & Business Media, 2007.

[Bar+11] S. Barbarino et al. "A review of morphing aircraft". In: *Journal of Intelligent Material Systems and Structures* 22.9 (2011), pages 823–877.

[Bar+14] S. Barbarino et al. "A review on shape memory alloys with applications to morphing aircraft". In: *Smart Materials and Structures* 23.6 (2014), page 063001. URL: http://stacks.iop.org/0964-1726/23/i=6/a=063001.

[Bar04] Yoseph Bar-Cohen. *Electroactive polymer (EAP) actuators as artificial muscles: reality, potential, and challenges*. Volume 136. SPIE press, 2004.

[BCM86] M. Braza, P.H.H.M. Chassaing, and H.H. Minh. "Numerical study and physical analysis of the pressure and velocity fields in the near wake of a circular cylinder". In: *Journal of fluid mechanics* 165 (1986), pages 79–130.

[Ber11] Berkooz, G. and Holmes, P. and Lumley, J.L. "The proper orthogonal decomposition in the analysis of turbulent flows". In: *Annual Review of Fluid Mechanics* 25.1 (2011), pages 539–575.

[BF93] R.E. Brown and M.R. Fedde. “Airflow sensors in the avian wing”. In: *Journal of experimental biology* 179.1 (1993), pages 13–30.

[BFP01] M. BRAZA, D. Faghani, and H. Persillon. “Successive stages and the role of natural vortex dislocations in three-dimensional wake transition”. In: *Journal of Fluid Mechanics* 439 (2001), pages 1–41.

[Bil+10] O. Bilgen et al. “Macro-fiber composite actuated simply supported thin airfoils”. In: *Smart Materials and Structures* 19.5 (2010), page 055010.

[Bil05] Onur Bilgen. “Aerodynamic and Electromechanical Design, Modeling and Implementation of Piezocomposite Airfoils”. PhD thesis. Virginia Polytechnic Institue and State University, 2005.

[BL07] M. Behl and A. Lendlein. “Shape-memory polymers”. In: *Materials today* 10.4 (2007), pages 20–28.

[Bou+08] R. Bourguet et al. “Anisotropic Organised Eddy Simulation for the prediction of non-equilibrium turbulent flows around bodies”. In: *Journal of Fluids and Structures* 24.8 (2008), pages 1240–1251.

[Bri07] Michel Brissaud. *Matériaux piézoélectriques: caractérisation, modélisation et vibration*. PPUR presses polytechniques, 2007.

[Bub+10] E.A. Bubert et al. “Design and fabrication of a passive 1D morphing aircraft skin”. In: *Journal of Intelligent Material Systems and Structures* 21.17 (2010), pages 1699–1717.

[Bur+15] D. Burdette et al. “Aerostructural design optimization of an adaptive morphing trailing edge wing”. In: *Proceedings of the AIAA Science and Technology Forum and Exposition (SciTech), Kissimmee, FL*. 2015, pages 2015–1129.

[Cat+03] L. Cattafesta et al. “Review of active control of flow-induced cavity resonance”. In: *AIAA paper* 3567 (2003), page 2003.

[CCP16] A. Cornogolub, P.J. Cottinet, and L. Petit. “Hybrid energy harvesting systems, using piezoelectric elements and dielectric polymers”. In: *Smart Materials and Structures* 25.9 (2016), page 095048.

[CCS96] J.D. Carlson, D.M. Catanzarite, and K.A. St. Clair. “Commercial magneto-rheological fluid devices”. In: *International Journal of Modern Physics B* 10.23n24 (1996), pages 2857–2865.

[Chi+14] M. Chinaud et al. "Trailing-edge dynamics and morphing of a deformable flat plate at high Reynolds number by time-resolved {PIV}". In: *Journal of Fluids and Structures* 47 (2014). Special Issue on Unsteady Separation in Fluid-Structure Interaction-l, pages 41–54. ISSN: 0889-9746. DOI: `http://dx.doi.org/10.1016/j.jfluidstructs.2014.02.007`. URL: `http://www.sciencedirect.com/science/article/pii/S0889974614000231`.

[CLM03] F. Claeyssen, N. Lhermet, and T. Maillard. "Magnetostrictive actuators compared to piezoelectric actuators". In: *Proc. SPIE*. Volume 4763. 2003, pages 194–199.

[CM16] F.T. Calkins and J.H. Mabe. "Flight Test of a Shape Memory Alloy Actuated Adaptive Trailing Edge Flap". In: *ASME 2016 Conference on Smart Materials, Adaptive Structures and Intelligent Systems*. American Society of Mechanical Engineers. 2016, V001T04A007–V001T04A007.

[Col+04] S.S. Collis et al. "Issues in active flow control: theory, control, simulation, and experiment". In: *Progress in Aerospace Sciences* 40.4 (2004), pages 237–289.

[CP15] C.J. Clark and R.O. Prum. "Aeroelastic flutter of feathers, flight and the evolution of non-vocal communication in birds". In: *Journal of Experimental Biology* 218.21 (2015), pages 3520–3527.

[Cum+16] St.B. Cumming et al. "Aerodynamic Flight-Test Results for the Adaptive Compliant Trailing Edge". In: (2016).

[Deb+13] M. Debiasi et al. "Deformation of the upper and lower surfaces of an airfoil by macro fiber composite actuators". In: *31st AIAA applied aerodynamics conference*. 2013, pages 24–27.

[Dim+16] I. Dimino et al. "Smart Intelligent Aircraft Structures (SARISTU): Proceedings of the Final Project Conference". In: edited by Christof Piet Wölcken and Michael Papadopoulos. Cham: Springer International Publishing, 2016. Chapter Distributed Actuation and Control of a Morphing Wing Trailing Edge, pages 171–186. ISBN: 978-3-319-22413-8. DOI: `10.1007/978-3-319-22413-8_9`. URL: `http://dx.doi.org//10.1007//978-3-319-22413-8_9`.

[Dob10] Werner Dobrzynski. "Almost 40 years of airframe noise research: what did we achieve?" In: *Journal of aircraft* 47.2 (2010), pages 353–367.

[Duv05] Jé rôme Duval. "Conception et mise en oeuvre d'un système d'actionneurs AMF ré partis pour le contrôle de forme é lectroactif de voilures aéronautiques". PhD thesis. Institut National Polytechnique de Toulouse, 2005.

[Ela04] Mohammad Elahinia. “Effect of system dynamics on shape memory alloy behavior and control”. PhD thesis. Virginia Tech, 2004.

[Ert+08] A. Erturk et al. “Piezoelectric energy harvesting from macro-fiber composites with an application to morphing-wing aircrafts”. In: *Proceedings of the 19th International Conference on Adaptive Structures and Technologies, Ascona, Switzerland, Oct.* 2008, pages 6–9.

[ESW03] D.M. Elzey, A.Y.N. Sofla, and H.N.G. Wadley. “A bio-inspired high-authority actuator for shape morphing structures”. In: *Smart Structures and Materials 2003* 5053 (2003), pages 92–100.

[FL95] Rong F.H. and Chih L.L. “Vortex Shedding and Shear-Layer Instability of Wing at Low-Reynolds Numbers”. In: *AIAA Journal* 33.8 (1995), pages 1398–1403. DOI: `http://dx.doi.org/10.2514/3.12561`.

[FNM16] A.D.B.L. Ferreira, P.R.O. Novoa, and A.T. Marques. “Multifunctional material systems: a state-of-the-art review”. In: *Composite Structures* 151 (2016), pages 3–35.

[FT06] R. Featherstone and Y. Teh. “Improving the speed of shape memory alloy actuators by faster electrical heating”. In: *Experimental Robotics IX* (2006), pages 67–76.

[GH97] D. Grant and V. Hayward. “Variable structure control of shape memory alloy actuators”. In: *IEEE Control Systems Magazine* 17.3 (1997), pages 80–88.

[Gid+11] P. F Giddings et al. “Modelling of piezoelectrically actuated bistable composites”. In: *Materials Letters* 65.9 (2011), pages 1261–1263.

[GK15] N. Gabdullin and S.H. Khan. “Review of properties of magnetic shape memory (MSM) alloys and MSM actuator designs”. In: *Journal of Physics: Conference Series*. Volume 588. 1. IOP Publishing. 2015, page 012052.

[Gre95] S.I. Green. *Fluid Vortices: Fluid Mechanics and its Applications*. Volume 30. New York, NY: Springer, 1995.

[Gri] Grigorie, L. and Botez, M.R. and Popov, A.V. “Self-adaptive morphing wing model, smart actuated and controlled by using a multi-loop controller based on a laminar flow real time optimizer”. In: *24th AIAA/AHS Adaptive Structures Conference, San Diego CA, USA, 4–8 January 2016*.

[Hai+14] C.S. Haines et al. “Artificial muscles from fishing line and sewing thread”. In: *science* 343.6173 (2014), pages 868–872.

[HBP16] C.J.C. Heath, I.P. Bond, and K.D. Potter. “Variable stiffness sandwich panels using electrostatic interlocking core”. In: *SPIE Smart Structures and Materials+ Nondestructive Evaluation and Health Monitoring*. International Society for Optics and Photonics. 2016, 97992A.

[HEW08] J.C.R. Hunt, I. Eames, and J. Westerweel. “Vortical Interactions with Interfacial Shear Layers”. In: *IUTAM Symposium on Computational Physics and New Perspectives in Turbulence: Proceedings of the IUTAM Symposium on Computational Physics and New Perspectives in Turbulence, Nagoya University, Nagoya, Japan, September, 11-14, 2006*. Edited by Yukio Kaneda. Dordrecht: Springer Netherlands, 2008, pages 331–338. ISBN: 978-1-4020-6472-2. DOI: 10.1007/978-1-4020-6472-2_50. URL: http://dx.doi.org/10.1007/978-1-4020-6472-2_50.

[HFA97] J.E. Huber, N.A. Fleck, and M.F. Ashby. “The selection of mechanical actuators based on performance indices”. In: *Proceedings of the Royal Society of London A: Mathematical, Physical and Engineering Sciences*. Volume 453. 1965. The Royal Society. 1997, pages 2185–2205.

[HL95] R.F. Huang and C.L. Lin. “Vortex shedding and shear-layer instability of wing at low-Reynolds numbers”. In: *AIAA journal* 33.8 (1995), pages 1398–1403.

[Hoa+03] Y. Hoarau et al. “Organized modes and the three-dimensional transition to turbulence in the incompressible flow around a NACA0012 wing”. In: *Journal of Fluid Mechanics* 496 (December 2003), pages 63–72. DOI: 10.1017/S0022112003006530. URL: https://www.cambridge.org/core/article/organized-modes-and-the-three-dimensional-transition-to-turbulence-in-the-incompressible-flow-around-a-naca0012-wing/4D03E354E6CD728DCBA13B3D2A1FF963.

[Hun+16] J. Hunt et al. “Turbulence Near Interfaces—Modelling and Simulations”. In: *Advances in Fluid-Structure Interaction*. Edited by Marianna Braza, Alessandro Bottaro, and Mark Thompson. Volume 133. Notes on Numerical Fluid Mechanics and Multidisciplinary Design. Updated contributions reflecting new findings presented at the ERCOFTAC Symposium on Unsteady Separation in Fluid-Structure Interaction, 17-21 June 2013, St John Resort, Mykonos, Greece. Springer International Publishing Switzerland, April 2016, pages 283–292. DOI: 10.1007/978-3-319-27386-0_17. URL: http://icube-publis.unistra.fr/1-HISA16.

[Ina+15] K. Inaoka et al. “Feedback flow control of a low-Re airfoil by flap actuators”. In: *Journal of Fluids and Structures* 58 (2015), pages 319–330. ISSN: 0889-9746. DOI: `http://dx.doi.org/10.1016/j.jfluidstructs.2015.08.011`. URL: `http://www.sciencedirect.com/science/article/pii/S0889974615002108`.

[Jan+06] P. Janker et al. “New actuators for aircraft and space applications”. In: *Proc Actuator*. 2006, pages 325–330.

[Jan+14] J.M. Jani et al. “A review of shape memory alloy research, applications and opportunities”. In: *Materials & Design* 56 (2014), pages 1078–1113.

[Jay+05] J. Jayender et al. “Modelling and gain scheduled control of shape memory alloy actuators”. In: *Control Applications, 2005. CCA 2005. Proceedings of 2005 IEEE Conference on*. IEEE. 2005, pages 767–772.

[Jay+08] J. Jayender et al. “Modeling and control of shape memory alloy actuators”. In: *IEEE transactions on control systems technology* 16.2 (2008), pages 279–287.

[Jod] Jodin, G. and Scheller, J. and Rizzo, K.J. and Duhayon, E. and Rouchon, J.F. and Braza M. “Dimensionnement d’une maquette pour l’investigation du morphing électroactif hybride en soufflerie subsonique”. In: *Congrès Français de Mécanique, Online AFM, Association Française de Mécanique, 2015.*

[Jod+17] G. Jodin et al. “Implementation of a hybrid electro-active actuated morphing wing in wind tunnel”. In: *{To appear in} Solid State Phenomena* (2017).

[K+14] A. Koreanschi, O. Sugar-Gabor, R.M. Botez, et al. “New numerical study of boundary layer behavior on a morphing wing-with-aileron system”. In: *American Institute of Aeronautics and Astronautics AIAA 32nd Applied Aerodynamics Conference, Atlanta, GA, USA*. 2014, pages 16–20.

[KB12] S. Kunze and C. Brücker. “Control of vortex shedding on a circular cylinder using self-adaptive hairy-flaps”. In: *Comptes Rendus Mécanique* 340.1-2 (2012), pages 41–56.

[KBR14] S.H. Ko, J.S. Bae, and J.H. Rho. “Development of a morphing flap using shape memory alloy actuators: the aerodynamic characteristics of a morphing flap”. In: *Smart Materials and Structures* 23.7 (2014), page 074015.

[KFC16] S. Kota, P. Flick, and F. Collier. “Flight Testing of the FlexFloil TM Adaptive Compliant Trailing Edge”. In: *54th AIAA Aerospace Sciences Meeting*. 2016, page 0036.

[KH08] S. Kota and J.A. Hetrick. *Adaptive compliant wing and rotor system*. US Patent 7,384,016. June 2008.

[Kim+12] H. Kim et al. “Sensorless displacement estimation of a shape memory alloy coil spring actuator using inductance”. In: *Smart Materials and Structures* 22.2 (2012), page 025001.

[Kim16] Wonhee Kim. “Model-based Design Framework for Shape Memory Alloy Wire Actuation Devices”. PhD thesis. Mechanical engineering department of the University of Michigan, 2016.

[Kin+16] M. Kintscher et al. “Assessment of the SARISTU enhanced adaptive droop nose”. In: *Smart Intelligent Aircraft Structures (SARISTU)*. Springer, 2016, pages 113–140.

[KN14] U.K. Kaul and N.T. Nguyen. “Drag Optimization Study of Variable Camber Continuous Trailing Edge Flap (VCCTEF) Using OVERFLOW”. In: *AIAA Paper* 2444 (2014), page 2014.

[Lee+15] J. Lee S.and Kim et al. “The function of the alula in avian flight.” In: *Scientific reports* 5 (2015), pages 9914–9914.

[Lex13] Christian Lexcellent. *Shape-memory alloys handbook*. John Wiley & Sons, 2013.

[Li+15] C. Li et al. “Passive vibration control of flexible hydrofoils using piezoelectric material”. In: *Fourth International Symposium on Marine Propulsors, Austin, TX, June*. 2015.

[LI14] B.W. LaCroix and P.G. Ifju. “Macro fiber composites and substrate materials for MAV wing morphing”. In: *Experimental Mechanics of Composite, Hybrid, and Multifunctional Materials, Volume 6*. Springer, 2014, pages 89–101.

[Lil98] G.M. Lilley. “A study of the silent flight of the owl”. In: *AIAA paper* 2340.1998 (1998), pages l–6.

[Lin02] J.C. Lin. “Review of research on low-profile vortex generators to control boundary-layer separation”. In: *Progress in Aerospace Sciences* 38.4 (2002), pages 389–420.

[LM15] Z. Lyu and J.R.R.A. Martins. “Aerodynamic Shape Optimization of an Adaptive Morphing Trailing Edge Wing”. In: *Journal of Aircraft* 52 (November 2015), 1951–1970. DOI: 10.2514/1.C033116.

[Mad+16] F. B Madsen et al. “The Current State of Silicone-Based Dielectric Elastomer Transducers”. In: *Macromolecular rapid communications* 37.5 (2016), pages 378–413.

[Mil+16] E.J. Miller et al. “Evaluation of the Hinge Moment and Normal Force Aerodynamic Loads from a Seamless Adaptive Compliant Trailing Edge Flap in Flight”. In: *54th AIAA Aerospace Sciences Meeting*. 2016.

[MMD16] V. Motta, P. Mouyon, and C. Döll. “Discrete Time Open-Loop and Closed-Loop Flow Control Based on Van der Pol Modeling”. In: *8th AIAA Flow Control Conference*. 2016, page 3256.

[Mot15a] Motta, V. and Quaranta, G. “Linear Reduced-Order Model for Unsteady Aerodynamics of an L-Shaped Gurney Flap”. In: *Journal of Aircraft* 52 (2015), pages 1887–1904. DOI: `{10.2514/1.C033099}`.

[Mot15b] V. Motta. “Computational fluid dynamic analysis of a L-shaped Gurney flap for vibration control”. PhD thesis. Milano, ITALY: Politecnico di Milano, 2015.

[MSL04] N. Ma, G. Song, and H.J. Lee. “Position control of shape memory alloy actuators with internal electrical resistance feedback using neural networks”. In: *Smart materials and structures* 13.4 (2004), page 777.

[Mus01] A. Musolff. “Adaptiver Tragflügel mit Formgedächtnisaktuatoren”. In: *Konstruktion* 5 (2001), pages 72–77.

[NA09] D. Neal and H. Asada. “Nonlinear, large-strain PZT actuators using controlled structural buckling”. In: *Robotics and Automation, 2009. ICRA'09. IEEE International Conference on*. IEEE. 2009, pages 170–175.

[Nag+16] C. Nagel et al. “Seamless Morphing Concepts for Smart Aircraft Wing Tip”. In: *Smart Intelligent Aircraft Structures (SARISTU)*. Springer, 2016, pages 275–291.

[Nor11] Norman, A.K. and McKeon, B.J. “Unsteady force measurements in sphere flow from subcritical to supercritical Reynolds numbers”. In: *Experiments in fluids* 51 (2011), pages 1439–1453.

[Oha+12] O.J. Ohanian et al. “Piezoelectric morphing versus servo-actuated MAV control surfaces”. In: *AIAA Paper* 1512 (2012), pages 23–26.

[Orn13] Cornell Lab of Ornithology. *All About Feathers. All About Bird Biology*. Cornell Lab of Ornithology, Ithaca, New York. 2013. URL: `https://academy.allaboutbirds.org/feathers-article/` (visited on July 9, 2017).

[PAM16] R. Pecora, F. Amoroso, and M. Magnifico. "Toward the bi-modal camber morphing of large aircraft wing flaps: the CleanSky experience". In: volume 9801. 2016, pages 980106–98018. DOI: 10.1117/12.2218415. URL: http://dx.doi.org/10.1117/12.2218415.

[PB98] H. Persillon and M. Braza. "Physical analysis of the transition to turbulence in the wake of a circular cylinder by three-dimensional Navier–Stokes simulation". In: *Journal of Fluid Mechanics* 365 (1998), pages 23–88.

[PDW02] D.M. Pitt, J.P. Dunne, and E.V. White. "SAMPSON smart inlet design overview and wind tunnel test Part I-Design overview". In: *Proc. SPIE*. Volume 4698. 2002, page 13.

[Per05] R. Perrin. "Analyse physique et modélisation d'écoulements incompressibles instationnaires turbulents autour d'un cylindre circulaire à grand nombre de Reynolds". PhD thesis. 2005.

[PFI15] A.M. Pankonien, C.T. Faria, and D.J. Inman. "Synergistic smart morphing aileron: Experimental quasi-static performance characterization". In: *Journal of Intelligent Material Systems and Structures* 26.10 (2015), pages 1179–1190.

[PML14] N. Precup, M. Mor, and E. Livne. "Design, Construction, and Tests of an Aeroelastic Wind Tunnel Model of a Variable Camber Continuous Trailing Edge Flap (VCCTEF) Concept Wing". In: *AIAA Paper* 2442 (2014).

[Ram+05] D.S. Ramrakhyani et al. "Aircraft structural morphing using tendon-actuated compliant cellular trusses". In: *Journal of aircraft* 42.6 (2005), pages 1615–1621.

[Red+02] O.K. Rediniotis et al. "Development of a shape-memory-alloy actuated biomimetic hydrofoil". In: *Journal of Intelligent Material Systems and Structures* 13.1 (2002), pages 35–49.

[Rou+11] J.F. Rouchon et al. "Activation d'une voilure déformable par des câbles d'AMF répartis en surface". In: *20ème Congrès Français de Mécanique, 28 août/2 sept. 2011-25044 Besançon, France (FR)* (2011).

[Rou+13] J.F. Rouchon et al. "Assembling and testing of quasi-static hybrid piezoelectric motor based on electroactive lubrication principle". In: *Archives of Electrical Engineering* 62.2 (2013), pages 237–250.

[RSE14] K.S. Ramadan, D. Sameoto, and S. Evoy. "A review of piezoelectric polymers as functional materials for electromechanical transducers". In: *Smart Materials and Structures* 23.3 (2014), page 033001.

[SCB03] G. Song, V. Chaudhry, and C. Batur. "Precision tracking control of shape memory alloy actuators using neural networks and a sliding-mode based robust controller". In: *Smart materials and structures* 12.2 (2003), page 223.

[Sch] Scheller, J. and Rizzo, K. and Duhayon, E. and Rouchon, J.F. and Braza, M. "A hybrid morphing NACA4412 airfoil concept". In: *IEEE International Conference on Industrial Technology (ICIT), 17–19 March 2015, Seville, Spain*, pages 1974–1978. DOI: `10.1109/ICIT.2015.7125385`.

[Sch+15] J. Scheller et al. "Trailing-edge dynamics of a morphing {NACA0012} aileron at high Reynolds number by high-speed {PIV}". In: *Journal of Fluids and Structures* 55 (2015), pages 42–51. ISSN: 0889-9746. DOI: `http://dx.doi.org/10.1016/j.jfluidstructs.2014.12.012`. URL: `http://www.sciencedirect.com/science/article/pii/S0889974615000158`.

[Sch+16] J. Scheller et al. "A Combined Smart-materials Approach for Next-generation Airfoils." In: *Solid State Phenomena* 251 (2016).

[Sch15] Johannes Scheller. "Electroactive morphing for the aerodynamic performance improvement of next generation airvehicles". PhD thesis. Institut Narional Polytechnique de Toulouse, 2015.

[SF05] C. Scherer and Antonio M. Figueiredo N. "Ferrofluids: properties and applications". In: *Brazilian Journal of Physics* 35.3A (2005), pages 718–727.

[SK01] M. Shahinpoor and K.J. Kim. "Ionic polymer-metal composites: I. Fundamentals". In: *Smart materials and structures* 10.4 (2001), page 819.

[SLY08] A.K. Seow, Y. Liu, and W.K. Yeo. "Shape memory alloy as actuator to deflect a wing flap". In: *AIAA Paper* 1704 (2008).

[Szu+15] D. Szubert et al. "Shock-vortex shear-layer interaction in the transonic flow around a supercritical airfoil at high Reynolds number in buffet conditions". In: *Journal of Fluids and Structures* 55 (2015), pages 276–302. ISSN: 0889-9746. DOI: `http://dx.doi.org/10.1016/j.jfluidstructs.2015.03.005`. URL: `http://www.sciencedirect.com/science/article/pii/S0889974615000602`.

[Szu+16] D. Szubert et al. "Numerical study of the turbulent transonic interaction and transition location effect involving optimisation around a supercritical aerofoil". In: *European Journal of Mechanics-B/Fluids* 55 (2016), pages 380–393.

[Szu15] Damien Szubert. “Physics and modelling of unsteady turbulent flows around aerodynamic and hydrodynamic structures at high Reynold number by numerical simulation”. PhD thesis. Institut Narional Polytechnique de Toulouse, 2015.

[Thi+08] C. Thill et al. “Morphing skins”. In: *The Aeronautical Journal* 112.1129 (2008), pages 117–139.

[Urs+07] N. Ursache et al. “Morphing winglets for aircraft multi-phase improvement”. In: *7th AIAA ATIO Conf, 2nd CEIAT Int’l Conf on Innov and Integr in Aero Sciences, 17th LTA Systems Tech Conf; followed by 2nd TEOS Forum*. 2007, page 7813.

[WBF14] B.K.S. Woods, O. Bilgen, and M.I. Friswell. “Wind tunnel testing of the fish bone active camber morphing concept”. In: *Journal of Intelligent Material Systems and Structures* 25.7 (2014), pages 772–785.

[Wel67] P.D. Welch. “The use of fast Fourier transform for the estimation of power spectra: A method based on time averaging over short, modified periodograms”. In: *IEEE Transactions on audio and electroacoustics* 15.2 (1967), pages 70–73.

[Wu+17] R. Wu et al. “A morphing aerofoil with highly controllable aerodynamic performance”. In: *The Aeronautical Journal* 121.1235 (2017), pages 54–72.

[YSK06] S. Yarusevych, P.E. Sullivan, and J.G. Kawall. “Coherent structures in an airfoil boundary layer and wake at low Reynolds numbers”. In: *Physics of Fluids* 18.4, 044101 (2006). DOI: `http://dx.doi.org/10.1063/1.2187069`. URL: `http://scitation.aip.org/content/aip/journal/pof2/18/4/10.1063/1.2187069`.

Résumé :

Le Morphisme Electroactif est un axe multidisciplinaire, associant l'aérodynamique, les matériaux innovants et la mécatronique. Ce concept consiste en l'amélioration des performances aérodynamiques par l'utilisation d'actionneurs déformant la surface portante d'un aéronef en temps réel.

Soutenue par Airbus, la modélisation, conception et réalisation d'un démonstrateur petite échelle est une première étape. Basée sur un profil d'aile A320, il est équipé d'actionnements pour le morphisme électroactif hybride : de grandes déformations à faibles vitesses par des Alliages à Mémoire de Forme sont associés à l'intégration au bord de fuite d'actionneurs piézoélectriques permettant de hautes fréquences d'actionnement à amplitude moindre.

Une seconde étape de la thèse est dédiés aux essais en soufflerie. La mesure de forces et la vélocimétrie d'images de particules permettent de comprendre la physique de l'écoulement et de la turbulence. L'étude de ce couplage fluide-structure-actionneurs présente les effets du morphisme par actionnement indépendant ; puis le couplage non linéaire de l'actionnement hybride.

La troisième étape consiste au passage vers une échelle réaliste des actionneurs, par la conception d'un volet « électro-morphé ». Une approche de dimensionnement par optimisation est proposée. Basé sur des technologies nouvelles d'actionnement, un prototype d'un tel macro-actionneur est alors conçu pour être testé.

Mots clés :

morphisme de structure, matériaux électroactifs, aéronautique, soufflerie, turbulence

Abstract:

Electroactive Morphing is a multidisciplinary axis, combining aerodynamics, innovative materials and mechatronics. This concept consists in improving the aerodynamic performance by the use of actuators deforming the airfoil of an aircraft in real time.

Supported by Airbus, the modeling, design and implementation of a small scale demonstrator is a first step. Based on an A320 wing profile, it is equipped with actuators for hybrid electroactive morphing: large deformations at low speeds by Shape Memory Alloys are associated with the integration at the trailing edge of piezoelectric actuators allowing high operating frequencies at lower amplitude.

A second step of the thesis is dedicated to wind tunnel tests. The measurement of forces and the Particle Image Velocimetries allow for the understanding of the flow and turbulence physics. The study of this fluid-structure-actuator coupling presents the effects of the morphism by independent actuation; then the nonlinear coupling of the hybrid actuation.

The third step is the transition to a realistic scale of actuators, by designing an "electro-morphed" macro-actuator. An optimization sizing approach is proposed. Based on new actuation technologies, a prototype of such a macro-actuator is then designed to be tested.

Keywords:

structure morphing, electroactive materials, aeronautics, true scale, turbulence